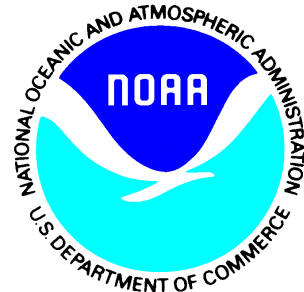

**NOAA Unique Combined Atmospheric Processing
System (NUCAPS)**

Algorithm Theoretical Basis Document

Compiled by the
STAR NUCAPS Team



Version 3.1
April 21, 2021

TITLE: NUCAPS ALGORITHM THEORETICAL BASIS DOCUMENT

CONTRIBUTORS (listed in alphabetical order):

Christopher D. Barnet (STC, formerly NOAA/NESDIS/STAR)

Murty Divakarla (IMSG Inc. at NOAA/NESDIS/STAR)

Antonia Gambacorta (formerly IMSG Inc. at NOAA/NESDIS/STAR)

Flavio Iturbide-Sanchez (NOAA/NESDIS/STAR)

Nicholas R. Nalli (IMSG Inc. at NOAA/NESDIS/STAR)

Ken Pryor (NOAA/NESDIS/STAR)

Changyi Tan (IMSG Inc. at NOAA/NESDIS/STAR)

Tianyuan Wang (IMSG Inc. at NOAA/NESDIS/STAR)

Juying Warner (University of Maryland)

Kexin Zhang (formerly IMSG Inc. at NOAA/NESDIS/STAR)

Tong Zhu (IMSG Inc. at NOAA/NESDIS/STAR)

**DOCUMENT HISTORY
 DOCUMENT REVISION LOG**

The Document Revision Log identifies the series of revisions to this document since the baseline release. Please refer to the above page for version number information.

DOCUMENT TITLE: Algorithm Theoretical Basis Document			
DOCUMENT CHANGE HISTORY			
Revision No.	Date	Revision Originator Project Group	CCR Approval # and Date
1.0	21 Aug 2013	Version 1.0 draft for CrIS/ATMS, supersedes NPOESS CrIMSS EDR	
2.0	14 Aug 2017	Updates and enhancements to v1.0	
3.0	21 Dec 2020	Revamp, corrections and updates to v2.0	
3.1	21 Apr 2021	Include carbon trace gas summary	

LIST OF CHANGES

Significant alterations made to this document are annotated in the List of Changes table.

DOCUMENT TITLE: Algorithm Theoretical Basis Document					
LIST OF CHANGE-AFFECTED PAGES/SECTIONS/APPENDICES					
Version Number	Date	Changed By	Pages	Section	Description of Change(s)
v2.0	14 Aug 2017	Nalli, Gambacorta, Tan, Barnet, Zhang, Iturbide-Sanchez	all	all	Updates for CrIS-FSR and ATMS Block 2; error corrections; notation improvements; completion of validation chapter
v3.0	21 Dec 2020	Nalli, Divakarla, Zhu, Wang, Tan	all	all	Revamp in accordance with SPSRB template; updated for NOAA-20 & carbon trace gases additional cleanup and error corrections; notation improvements
v3.1	21 Apr 2021	Nalli, Warner, Divakarla, Pryor	103, 105–107	2.8.2	Include carbon trace gas algorithm upgrades and validation summary

TABLE OF CONTENTS

LIST OF TABLES	6
LIST OF FIGURES	7
1 INTRODUCTION	9
1.1 Product Overview	9
1.2 Satellite Instrument Description	11
1.2.1 The Advanced Technology Microwave Sounder (ATMS)	11
1.2.2 The Cross-Track Infrared Sounder (CrIS)	12
2 ALGORITHM DESCRIPTION	14
2.1 Processing Outline	14
2.2 Algorithm Inputs	14
2.2.1 Background Climatology Look Up Tables	14
2.2.2 Local Angle Adjustment Coefficients	17
2.2.3 Forecast Surface Pressure	17
2.2.4 IR Surface Emissivity First-Guess	17
2.2.5 Microwave and Infrared Tuning Coefficients	21
2.3 Radiative Transfer Models (RTM)	30
2.3.1 MW RTM	30
2.3.2 IR RTM	35
2.4 Microwave Retrieval Algorithm	43
2.4.1 Precipitation Flags, Rate Retrieval and ATMS Corrections.	43
2.4.2 MW-Only Profile Retrieval Algorithm	47
2.5 Regression Retrieval	52
2.5.1 Post-Launch First Guess Regression Procedure	52
2.6 Cloud-Clearing	61
2.7 Physical Retrieval Algorithm	70
2.7.1 The Inverse Problem	70

- 2.7.2 Linearization of the RTE 71
- 2.7.3 IR+MW Physical Retrieval Module 74
- 2.7.4 Specification of Geophysical Functions 76
- 2.7.5 Retrieval Error Covariance Matrix 78
- 2.7.6 The Retrieval of the Geophysical State 79
- 2.7.7 Rejection Criteria 82
- 2.8 Validation 86
 - 2.8.1 Sounder Validation Methodology 86
 - 2.8.2 SNPP, NOAA-20 and Metop-A/B/C NUCAPS Validation 98

3 REFERENCES 108

LIST OF TABLES

2.1	View-Angle Regimes in Post-Launch Regression	56
2.2	Geophysical parameters, X_i , solved for in NUCAPS regression	57
2.3	Definition of the Geophysical State, $X_L^{s,i}$, in the NUCAPS Algorithm . . .	74
2.4	Retrieval Steps in the NUCAPS Algorithm	84
2.5	Scale Size of Perturbation Functions in v2.0	85
2.6	JPSS L1 Requirements for CrIS/ATMS AVTP Measurement Uncertainty	89
2.7	JPSS L1 Requirements for CrIS/ATMS AVMP Measurement Uncertainty	90
2.8	JPSS Level 1 Requirements* for IR Ozone Profile EDR	91
2.9	JPSS L1 Requirements for CrIS IR Trace Gas Measurement Uncertainty	96

LIST OF FIGURES

2.1 NUCAPS Level 2 retrieval processing flow chart. 15

2.2 Typical emissivity spectra of snow, ice, distilled water, and sea water in TIR obtained at the exitance angle 10 degree by past laboratory experiments reproduced from the ASTER Spectral Library and from the MODIS University of California, Santa Barbara (USCB) Emissivity Library (Wan and Zhang, 1999). 19

2.3 CrIS radiance spectrum with red asterisks showing the 16 pre-selected CrIS window channels for the regression training: (top) LWIR, (bottom) MWIR. 20

2.4 Regression bias and standard deviation over warm land. 21

2.5 Regression bias and standard deviation over ice/snow land. 22

2.6 ATMS bias tuning correction for channels 1–22, as a function of view angle. Results show the actual bias correction for the ATMS/TDR Block 1.0, and the most recent correction made for ATMS/TDR Block 2.0. . . . 24

2.7 ATMS RTA error for channels 1–22. Results show the actual RTA error for the ATMS/TDR Block 1.0, and the most recent correction made for ATMS/TDR Block 2.0. 25

2.8 The collocation of CrIS FOVs and VIIRS pixels. The red circles (or ovals) represents the CrIS FOVs and the pixel dots are VIIRS pixels (blue: cloudy; yellow: probably cloudy; grey circles: clear). The upper panel shows the one single CrIS scan line. The lower left shows the 11th CrIS FOR of the particular scan line. The lower right even zooms in to show the 2nd FOV of the particular FOR. 26

2.9 The CrIS full spectral-resolution (FSR) RTA bias versus nominal spectral-resolution (NSR) RTA bias. The blue shows the FSR RTA bias and the red shows the NSR RTA bias. 27

2.10 The CrIS-FSR RTA error (standard deviation) versus NSR RTA error. The blue shows the FSR RTA error and the red shows the NSR RTA error. 28

2.11 The comparison of CrIS-FSR RTA biases for SNPP (blue) and NOAA-20 (red) retrievals. 29

2.12 NUCAPS quality control flag showing regions where the IR/MW retrieval converges (blue regions) and where the MW-Only retrieval fails (red regions) for the ascending (left figure) and descending (right figure) satellite modes and for the NUCAPS version 2.0.5.4. 44

2.13 Temperature at 500 hPa for the ascending (left plot) and descending (right plot) satellite modes, retrieved by the NUCAPS MW-only retrieval (offline v2.0.5.4). 51

2.14 Water Vapor at 950 hPa for the ascending (left plot) and descending (right plot) satellite modes, retrieved by the NUCAPS MW-only retrieval (offline v2.0.5.4). 51

2.15 Geographic histograms of NOAA-20 dedicated and GRUAN reference RAOB collocations NUCAPS EDR validation 99

2.16 Geographic histograms of NOAA-20 ozonesonde collocations used for NOAA-20 NUCAPS IR ozone profile EDR validation 100

2.17 Coarse- and broad-layer statistical uncertainty assessment of the NOAA-20 NUCAPS AVTP EDR 101

2.18 As Figure 2.17 except for AVMP 102

2.19 As Figure 2.17 except for AVMP 102

2.20 As Figure 2.17 except for Metop-A/B/C versus global ECMWF model . . 104

2.21 As Figure 2.18 except for Metop-A/B/C versus global ECMWF model . . 104

2.22 NUCAPS CO₂ comparison with OCO-2 105

2.23 NOAA-20 NUCAPS-ATom aircraft collocations 106

2.24 NOAA-20 NUCAPS-ATom carbon trace gas profile statistics 107

1. INTRODUCTION

Launched on board the Joint Polar Satellite System (JPSS) Suomi National Polar-orbiting Partnership (SNPP) platform on 28 October 2011, the Cross-track Infrared Sounder (CrIS) and the Advanced Technology Microwave Sounder (ATMS) represent the U.S. next generation of polar-orbiting operational combined hyperspectral-infrared and microwave (IR/MW) sounding systems (Goldberg et al., 2013).

CrIS is a Fourier transform spectrometer (FTS) that measures calibrated infrared (IR) radiances in 2211 channels covering the longwave ($655\text{--}1095\text{ cm}^{-1}$), midwave ($1210\text{--}1750\text{ cm}^{-1}$), and shortwave ($2155\text{--}2550\text{ cm}^{-1}$) infrared spectral regions with a spectral resolution of 0.625 cm^{-1} across all three bands. ATMS is a cross-track scanner with 22 channels in spectral bands from 23 GHz through 183 GHz. This suite of instruments has been designed to guarantee continuity to the 01:30, 13:30 equatorial crossing time orbit, in replacement of the AIRS/Advanced Microwave Sounding Unit (AMSU) instruments on board the NASA Aqua satellite and in conjunction with the European Metop satellite series operating the mid-morning orbit. Specifically, CrIS has been designed to continue the advances in atmospheric observations and research that started with the Atmospheric Infrared Sounder (AIRS) launched on the Aqua platform in 2002 (Aumann et al., 2003) and followed by the Infrared Atmospheric Sounding Interferometer (IASI), launched on the Meteorological Operational Satellite Program (Metop)-A platform in 2006. The ATMS will similarly continue the series of observations that started with the Advanced Microwave Sounding Unit (AMSU) first launched by NOAA in 1998.

1.1. Product Overview

In this document we describe the algorithm theoretical basis of the NOAA Unique Combined Atmospheric Processing System (NUCAPS), an algorithm built on the heritage from the of the AIRS Science Team (Susskind et al., 2003). The NOAA/NESDIS Center for Satellite Applications and Research (STAR) led the efforts to develop, test, validate and refine the NUCAPS algorithm to produce operationally cloud-cleared radiances (CCR) and global atmospheric profiles of environmental data records (EDRs). The algorithm has been adapted as an enterprise solution to work on the Joint Polar Satellite System (JPSS) SNPP/NOAA-20 CrIS/ATMS, and Metop IASI, AMSU-A and Microwave Humidity Sounder (MHS) instrument complements. The microwave (MW) sounder data from ATMS or AMSU-A/MHS (JPSS or Metop) are used in the NUCAPS

algorithm to produce MW-only retrieval in addition to the hyperspectral IR sounding retrievals from CrIS or IASI, and to assist in generating high-quality geophysical products under non-precipitating scenes with up to 80% cloud cover.

The NUCAPS suite of EDR products includes two different files in NetCDF format: the Standard Product and the Cloud-Cleared Radiance (CCR) Product. The Standard Product consists of retrieved estimates of geophysical variables such as temperature, water vapor, cloud fraction and cloud top pressure, along with trace gas retrievals such as ozone, methane, carbon monoxide, carbon dioxide, SO₂, N₂O, and HNO₃, and a flag indicating the presence of dust and volcano emission. The vertical sampling of each retrieved atmospheric profile variable consists of 100 points total between 1100 hPa and 0.016 hPa; Intermediate solutions from the microwave only step and the regression first guess are also part of the delivered standard output. Full spectrum cloud-cleared radiances are produced along with the Standard Product, as they are the radiances used to retrieve the Standard Product. Both the Standard and CCR Product files are generated at the field-of-regard (FOR) resolution. Each FOR contains an instantaneously measured 3 × 3 fields-of-view (FOVs). The CrIS FOVs are circular and have a diameter of 14 km at nadir. The UTC start time of the *N*th granule of each data is $[146 + 360(N - 1)] / 3600$ hours. The instrument provides 30 FORs for each scan of observations. Four scan lines constitute a granule, and a full day of data contains approximately 2700 granules of the CrIS observations.

NUCAPS runs within the Hyperspectral Enterprise Algorithm Package (HEAP) at the NOAA Satellite Operational Facility (NSOF). The HEAP provides the pre and post-processing capability for the NUCAPS to generate operational products from SNPP/NOAA-20 CrIS/ATMS and Metop-A/B IASI/AMSU-A/MHS sensors. In addition to NUCAPS products, the HEAP produces other derived hyperspectral radiance products such as thinned radiance data sets and principal component (PC) scores, and near real time CrIS outgoing longwave radiation (OLR). The thinned radiance products are in BUFR format specifically tailored to cater for Numerical Weather Prediction (NWP) centers.

A variety of NUCAPS sounding products are currently ingested into the Advanced Weather Interactive Processing System (AWIPS-2) for their utility by many Weather Forecasting Offices (WFOs) nationwide for analyzing atmospheric instabilities, potential outbreaks of severe weather, and now-casting applications. The NUCAPS algorithm is also part of the Community Satellite Processing Package to disseminate products through Direct Broadcast services with improved latency for regional applications. NUCAPS operational products are available to worldwide users through the NOAA Comprehensive Large Array-data Stewardship System (CLASS).

This ATBD is organized as follows. Section 1.2 describes the attributes of the CrIS

and ATMS sounding systems and Section 2 provides the overall algorithm description. Because NUCAPS is actually a combination of several algorithms (as overviewed in Section 2.1, which provides the processing processing outline), this section is further subdivided as follows: Section 2.2 describes the algorithm inputs; Section 2.4 describes the microwave (MW) module component of the algorithm; Section 2.5 describes the regression module for both the cloud-clearing input profile and the first guess; Section 2.6 describes the cloud-clearing algorithm; Section 2.7 describes the physical and mathematical basis of the algorithm, along with the technical characteristics of the algorithm processing flow; finally, Section 2.8 details the formal validation methodology of the algorithm EDRs.

1.2. Satellite Instrument Description

1.2.1. The Advanced Technology Microwave Sounder (ATMS)

The *Advanced Technology Microwave Sounder (ATMS)* is a cross-track scanner which combines all the channels of the preceding AMSU-A1, AMSU-A2, and AMSU-B sensors into a single package consisting of 22 channels in spectral bands from 23 GHz through 183 GHz. Channel 3–15 fall within the 50–60 GHz portion of the oxygen band to temperature and precipitation information.

In addition, ATMS contains three window-channels at 23.8, 31.4, and 89 GHz to provide total precipitable water, cloud liquid water content, and precipitation measurements, respectively. These channels can also be used to provide information on sea-ice concentration and snow cover. ATMS also has one window-channel at 166.31 GHz to obtain high-resolution measurements of precipitation, snow cover, and sea-ice. Three additional channels in the 183 GHz water vapor line are used to retrieve atmospheric humidity profiles. The 3-dB beam diameter of an ATMS FOV is 1.1, corresponding to about 16 km at nadir. This beam is co-located with the CrIS field-of-view (FOV). Table 1.1 describes the characteristics of the ATMS microwave sensor and of the AMSU/MHS suite.

The scanning geometry and footprint sizes of ATMS are somewhat different for every channel. Channels 1 and 2 have a beam width of 5.2° , which corresponds to a footprint size of 74.8 km at nadir. Channels 3–16 have a beam width of 2.2° , which corresponds to a footprint size of 31.6 km at nadir. Channels 17–22 have a beam size of 1.1° , which corresponds to a footprint size of 15.8 km. Because the ATMS scans at a rate of 8/3 seconds per scan, the scan pattern overlaps, but does not match exactly, the scan pattern of CrIS. The NUCAPS preprocessor performs collocation of ATMS observations to the CrIS FOR EDR algorithm assumes that the ATMS data

will be re-sampled to match the CrIS FOR configuration prior to ingestion by the CrIS software producing NUCAPS products.

Table 1.1: Description of the Channel Characteristics of the ATMS and AMSU/MHS Microwave Sensors (Weng et al., 2012)

Advanced Technology Microwave Sounder (ATMS) and AMSU/MHS						
Channel		Center Frequency (GHz)		Static Beamwidth (deg)		Weighting Function Peak (hPa)
ATMS	AMSU	ATMS	AMSU/MHS	ATMS	AMSU/MHS	
1			23.8	5.2	3.3	Window
2			31.4	5.2	3.3	Window
3			50.3	2.2	3.3	Window
4		51.76		2.2	3.3	950
5	4		52.8	2.2	3.3	850
6	5		53.596±0.115	2.2	3.3	700
7	6		54.4	2.2	3.3	400
8	7		54.94	2.2	3.3	250
9	8		55.5	2.2	3.3	200
10	9		57.29	2.2	3.3	100
11	10		57.29±0.217	2.2	3.3	50
12	11		57.29±0.322±0.048	2.2	3.3	25
13	12		57.29±0.322±0.022	2.2	3.3	10
14	13		57.29±0.322±0.010	2.2	3.3	5
15	14		57.29±0.322±0.0045	2.2	3.3	2
16	15		88.2	2.2	3.3	Window
	16				1.1	Window
17	17		165.5	1.1	1.1	Window
18	20		183.31±7.0	1.1	1.1	800
19			183.31±4.5	1.1		700
20	19		183.31±3.0	1.1	1.1	500
21			183.31±1.8	1.1		400
22	18		183.31±1.0	1.1	1.1	300

1.2.2. The Cross-Track Infrared Sounder (CrIS)

The *Cross-track IR Sounder (CrIS)* is a Fourier transform spectrometer (FTS) on-board the JPSS series (SNPP, NOAA-20, and JPSS-2, 3, and 4), measuring infrared radiation emitted from the surface of the Earth. Up until December 2014, the CrIS instrument was operating at a nominal spectral resolution (NSR) with a total of 1305 infrared sounding channels covering the longwave (655–1095 cm^{-1}), midwave (1210–1750 cm^{-1}), and shortwave (2155–2550 cm^{-1}) IR spectral regions (LWIR, MWIR and

SWIR, respectively). Starting December 4, 2014, the S-NPP CrIS has been operating at full spectral resolution (0.625 cm^{-1} across all three IR spectral bands. The CrIS instrument aboard the NOAA-20 has been operating at full spectral resolution from the launch.

Previous operational SNPP NUCAPS versions (v1.5) ran on CrIS spectra at the original nominal spectral resolution spectra of $\Delta\nu \simeq 0.625\text{ cm}^{-1}$, 1.25 cm^{-1} and 2.5 cm^{-1} for the LWIR, MWIR and SWIR bands, respectively. The reduced resolution in the MWIR and SWIR bands is the result of the interferograms being truncated in those bands during operational processing of the SDRs. The reduction in spectral resolution in these bands was empirically demonstrated by Gambacorta et al. (2014) to have an adverse impact upon trace gases, especially carbon monoxide. Full-resolution CrIS ($\Delta\nu \simeq 0.625\text{ cm}^{-1}$ in all three bands) thus led to offline production of full-spectral resolution (full-res) CrIS SDRs beginning in December 2014 (Han et al., 2015). Additional details of the CrIS design and measurement objectives are found in Han et al. (2013). The CrIS Full Spectral Resolution (FSR) instrument with 2211 channels at 0.625 cm^{-1} spectral resolution coupled with low noise in all three bands enable high quality CO and other trace gas retrievals. The increased spectral resolution also improves the calibration of the shortwave infrared (SWIR) and improve temperature sounding, which, in turn, leads to improved sounding products.

2. ALGORITHM DESCRIPTION

2.1. Processing Outline

The NUCAPS algorithm consists of the following six modules as summarized below.

1. Preliminary input quality control, look-up tables (LUT), and ancillary product acquisition.
2. The **microwave-only (MW-only) retrieval module** which derives cloud liquid water flags and microwave surface emissivity uncertainty (Rosenkranz, 2001).
3. An **all-sky fast eigenvector regression retrieval** for temperature and moisture that is trained against ECMWF analysis and CrIS all-sky radiances (Goldberg et al., 2003).
4. A **cloud-clearing module** that combines a set of microwave and IR channels (along with, in the future, visible observations provided by the onboard VIIRS instrument) to produce cloud-cleared IR radiances (Chahine, 1974).
5. A **cloud-cleared fast eigenvector regression retrieval** for temperature and moisture that is trained against ECMWF analysis and CrIS cloud-cleared radiances (Goldberg et al., 2003).
6. The **final infrared (IR) physical retrieval**, which employs the previous regression retrieval as the first-guess for temperature and water vapor (Susskind et al., 2003).

Figure 2.1 describes the complete flow diagram of the algorithm software architecture. The full description of the attributes of all input data used by the algorithm, including primary sensor data, ancillary data, forward models and look-up tables is provided in the next chapter.

2.2. Algorithm Inputs

2.2.1. Background Climatology Look Up Tables

Climatological background profiles of temperature and water vapor, used extensively in the MW-only retrieval step, are used to generate the covariance of the atmospheric

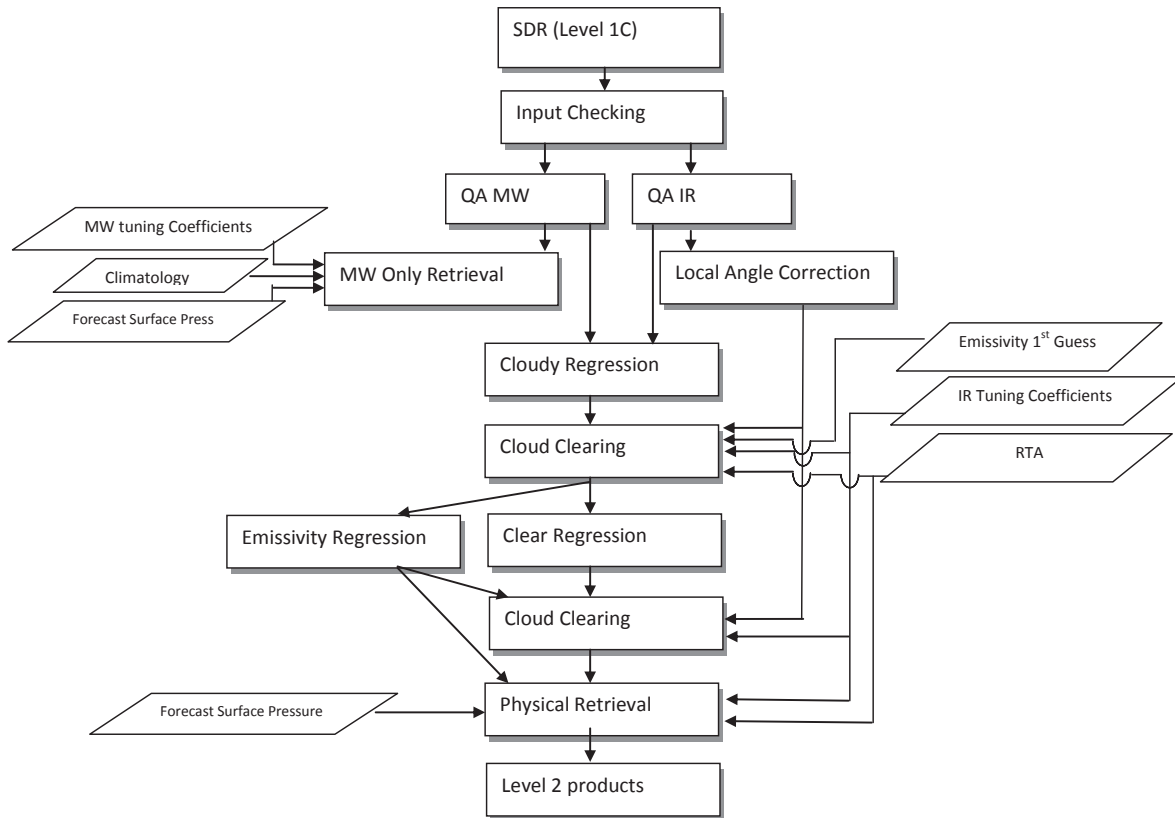


Figure 2.1: NUCAPS Level 2 retrieval processing flow chart.

temperature and water vapor. Climatological profiles of trace gases are also used as first guess in the physical retrieval step. The climatology for earlier versions of NUCAPS was based on two sources: (1) the National Center for Environmental Prediction (NCEP) temperature and water vapor monthly means derived from the 20 year (1979–1998) reanalysis on a 2.5 degree latitude/longitude grid; and (2) the Upper Atmosphere Research Satellite (UARS) temperature, water vapor and ozone profiles. The climatological temperature profile is obtained from the NCEP source from the surface up to 100 hPa, tri-linearly interpolated by month, latitude and longitude and then log-pressure interpolated onto the 100 levels. A P^4 extrapolation is used for altitudes above 100 hPa. The climatological water vapor profile is derived from the NCEP source from the surface up to 300 hPa, tri-linearly interpolated by month, latitude and longitude and then log-pressure interpolated onto the 100 levels. Above 300 hPa the information comes from the UARS source, linearly interpolated between two latitude zones. While keeping this old climatology as a backup option, a new climatology has been implemented into the NUCAPS, and has been used since the operational version HEAP 2.2. The new climatology is adapted from the Microwave Integrated Retrieval System climatology (MiRS v11.0). Generated from the ECMWF 2012 reanalysis, the climatology includes monthly atmospheric temperature and water vapor profiles on a global 5° latitude/longitude grid. The climatology is on the same 100 levels as that used in NUCAPS, and available four times a day (00, 06, 12, 18 UTC) to capture the daily changes of these two fields.

The *a priori* ozone climatology is derived from the UARS source, linearly interpolated between two latitude zones. No time interpolation is computed. The CO *a priori* was a 12 month set of two single CO profiles, for the northern and southern hemisphere respectively, computed from the Measurements of Pollution In The Troposphere (MOPITT) version 4 CO monthly averages. These profiles are temporally and spatially interpolated during the retrieval. The CH₄ *a priori* was a function of latitude and altitude was generated to capture its strong latitudinal and vertical gradients. This CH₄ *a priori* profile was generated by using a nonlinear polynomial fitting to different data, including the *in situ* aircraft observation data from six sites (the first six sites in Table 1) of the NOAA Global Monitoring Laboratory (GML), some ground-based flask network data (GLOBALVIEW-CH₄, 2005), Matsueda aircraft observation data (Matsueda and Inoue, 1996) and HALOE satellite observation data (Park et al., 1996) (<http://haloedata.larc.nasa.gov/download/index.php>). In the fitting only the mean profiles as a representative of its climatology for each location and altitude were used. For example, for each NOAA/ESRL/GMD site only the mean of all profiles observed in the past 3 years from 2003 to early 2006 was used. Matsueda aircraft data from GLOBALVIEW-CH₄ (2005) and HALOE data were interpolated to several latitudinal

grids first, and then the mean profiles corresponding to different latitude and altitude were used. Monthly average of model simulated data using the TM3 (Houweling et al., 2006) was used to extrapolate the in situ aircraft data to higher altitudes. Over the southern hemisphere oceans where in situ measurements are not available, yearly zonal mean profiles in several latitude grids from the TM3 model are also used. The N_2O climatology is given as a smoothed function of latitude and pressure. The generation of N_2O first-guess profile was from model data only. The model simulations are made by the Center for Climate System Research/National Institute for Environmental Studies/Frontier Research Center for Global Change (CCSR/NIES/FRCGC) using an Atmospheric General Circulation Model (AGCM)-based chemistry transport model.

2.2.2. Local Angle Adjustment Coefficients

CrIS makes a 90° measurement scan, cross-track between -49 and $+49^\circ$. The data analysis, however, uses the data in 3×3 clusters with 30 scan angles between -49 and $+49^\circ$. A primary assumption of cloud clearing is that within a 3×3 array of 9 CrIS FOVs the differences are solely attributed to differences in clouds. Local angle adjustment removes one potentially confounding source of intra-FOV variation: differences in observing geometry. In each 3×3 cluster there are 3 observations at each of 3 different scan angles. This step makes small adjustments to the spectra for the 3 highest- angle and 3 lowest-angle FOVs so all FOVs resemble those which would be observed at the central angle. No adjustment is applied to the central FOVs. In the AIRS retrieval algorithm, the actual adjustment is calculated using a PCs approach. Given the rotating scanning geometry of the CrIS instrument a more complex solution needs to be taken and is the subject of a work in progress. Unpublished studies have shown though that the local angle correction does not have significant impact on the retrieval performance and can be neglected with no noticeably detrimental effects.

2.2.3. Forecast Surface Pressure

The AVN forecast surface pressure, PSurf, is used by the NUCAPS L2 retrieval. The surface pressure is available on a one-degree grid. The surface pressure is calculated from the 3-, 6-, and 9-hour forecasts from the same model run, interpolated in space and time to match observed location.

2.2.4. IR Surface Emissivity First-Guess

The IR surface emissivity, ϵ_ν , is critical for accurate determination of the surface energy budget and it is a common input parameter for a variety of radiative transfer

models (Zhou et al., 2008). Due to the intrinsic characteristic differences between the oceanic and land surfaces, the ϵ_ν alters substantially from place to place. In the oceanic areas, the surface characteristics are more homogeneous, however the land surfaces are much more complex since the land surfaces can be covered by sands, grasses, soil, trees, ice, man-made structures, or their combinations. In the NUCAPS algorithm, the Masuda model (Masuda et al., 1988; Masuda, 2006) has been employed over ocean to estimate the ϵ_ν initial guess, while a synthetic regression approach is employed instead over land surfaces. Plans for upgrading the NUCAPS first-guess emissivities are currently underway. For oceans this would include accounting for the significant dependence of the IR optical constants of water on temperature and for land the plan is to replace the regression first-guess with the CAMEL database as a formal *a priori*, and possibly employ a physical model for snow/ice surfaces.

Training Data Set used for Emissivity First Guess Regression Over Land

The atmospheric profiles are based on the SeeBor Version 5.0 created by Eva Borbas and Suzanne Wetzel Seemann, University of Wisconsin-Madison (Seemann et al., 2008). The SeeBor Version 5.0 consists of global profiles of temperature, moisture, and ozone at 101 pressure levels in the clear sky condition. The total 15,704 profiles are taken from NOAA-88 (6137 profiles), an ECMWF 60-level training set (6015 profiles), TIGR-3 (1387 profiles), ozonesondes from 8 NOAA Climate Monitoring and Diagnostics Laboratory (CMDL) sites (1595 profiles), and radiosondes from the Sahara desert in 2004 (570 profiles). To ensure the quality of the atmospheric states, the screen-out criteria are set as: (1) the relative humidity (RH) value of the profiles must be less than 99% at each level below 250 hPa, and (2) the top pressure of sounding measurements must be no greater than 30 hPa for temperature and water vapor profiles and 10 hPa for ozone profiles. For each profile in the data set, the corresponding SSEs and surface skin temperature are added separately. The SSEs are set at 39 hinge points (see Appendix List 1) based on random characterization simulations to represent the SSEs of the whole spectra. The infrared emissivity of soil, tree and grass is obtained from MODIS UCSB Emissivity Library (see Figure 2.2). There are 70 types of soils, 23 types of trees and 7 types of grasses are included in the library. A random selection algorithm is applied to estimate the surface composition fractions.

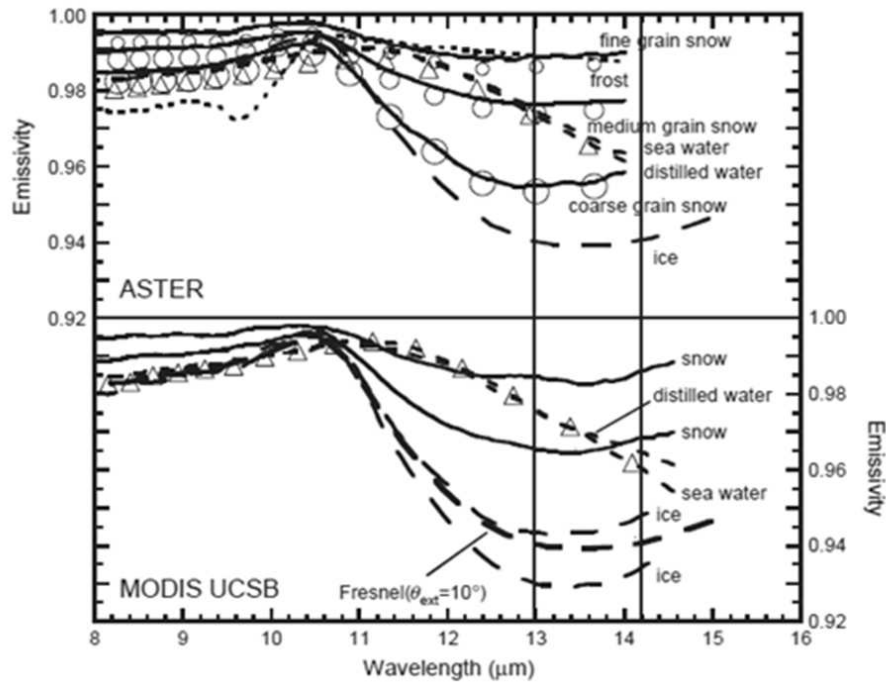


Figure 2.2: Typical emissivity spectra of snow, ice, distilled water, and sea water in TIR obtained at the exitance angle 10 degree by past laboratory experiments reproduced from the ASTER Spectral Library and from the MODIS University of California, Santa Barbara (USCB) Emissivity Library (Wan and Zhang, 1999).

Methodology of Emissivity First Guess Regression Over Land

The total data set includes different surface types, e.g. land, ocean, ice/snow. But different surface type behaviors vary very different in the spectra. The ϵ_ν regression training needs to be done separately by different surface types. We distinguish land or ocean by the geolocation of the profile and distinguish the warm land or ice/snow land by the surface temperature. The regression training is performed on the sub-datasets of warm land and ice/snow land, respectively. The predictors are the brightness temperatures of $m = 16$ pre-selected CrIS window channels (see the Appendix List 2 and Figure 2.3) and the satellite view angle, ϑ , while the fitting vector is composed by the SSEs of the $n = 39$ hinge points and the surface skin temperature, T_s , as per the

following equation

$$\begin{pmatrix} T_s \\ \epsilon_1 \\ \vdots \\ \epsilon_n \end{pmatrix} = \begin{pmatrix} C_{0,0} & C_{0,1} & \cdots & C_{0,m} \\ C_{1,0} & C_{1,1} & \cdots & C_{1,m} \\ \vdots & \vdots & \ddots & \vdots \\ C_{n,0} & C_{n,1} & \cdots & C_{n,m} \end{pmatrix} \begin{pmatrix} T_B(\nu_1) \\ \vdots \\ T_B(\nu_m) \\ \vartheta \end{pmatrix}. \quad (2.1)$$

The regression training is to solve the coefficients $C_{n,m}$ of the above equation. To consolidate the regression training, we add 1% random Gaussian distribution noises on the predictor vectors. For each subset, we random select 90% profiles for training to generate the coefficients and the rest 10% profiles are used for validate the training by applying the coefficients. Figures 2.4 and 2.5 show the low bias and standard deviations for land and snow surfaces, respectively, which indicate the regression training is robust.

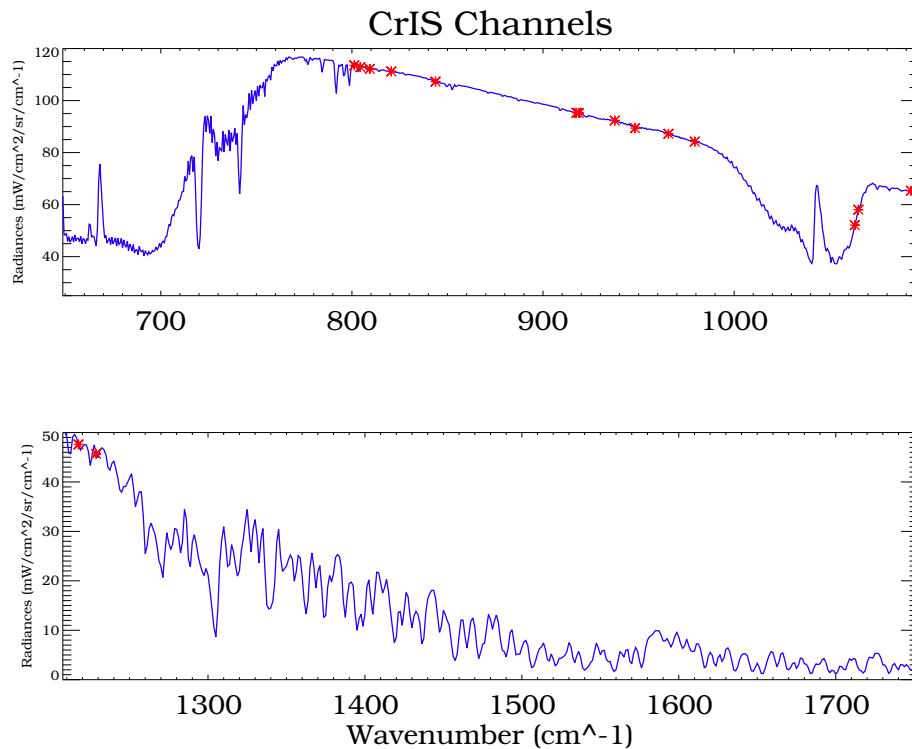


Figure 2.3: CrIS radiance spectrum with red asterisks showing the 16 pre-selected CrIS window channels for the regression training: (top) LWIR, (bottom) MWIR.

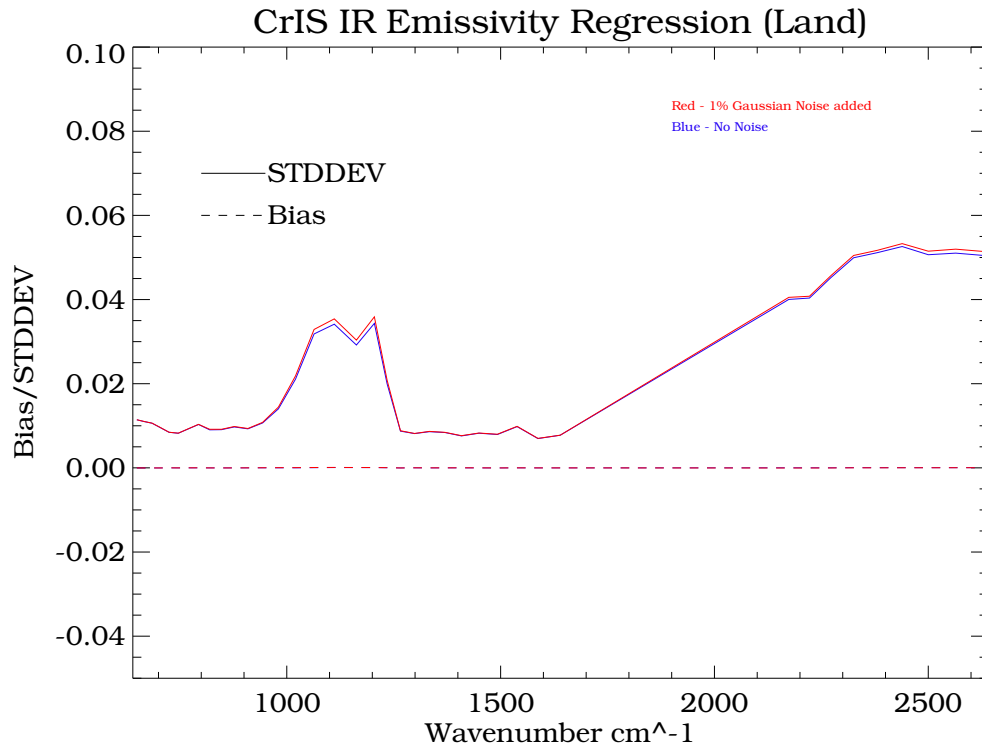


Figure 2.4: Regression bias and standard deviation over warm land.

2.2.5. Microwave and Infrared Tuning Coefficients

A large category of inversion algorithms relies on least square residual minimizations of observed brightness temperature and brightness temperatures computed from first guess profiles. In these algorithms, generally referred to as “physical,” radiative transfer calculations are performed by mean of theoretical forward models and there is a need for identifying and removing those components of the residuals arising from modeling, measurement errors and instrumental noise. This process, commonly referred to as brightness temperature tuning, is fundamental to achieve retrieval performance accuracy, in that it removes artificial systematic biases that could be otherwise ascribed to a physical atmospheric source and, in long term applications, erroneously confused with climate signals. Specifically, forward model errors may include both systematic and profile-dependent components. Systematic errors may include radiometric calibration, thermal emission from parts of the space-craft, and, for microwave sensors, antenna side lobe effects. These systematic sources of error can contribute to a large part of the overall bias and in the microwave case show dependence on

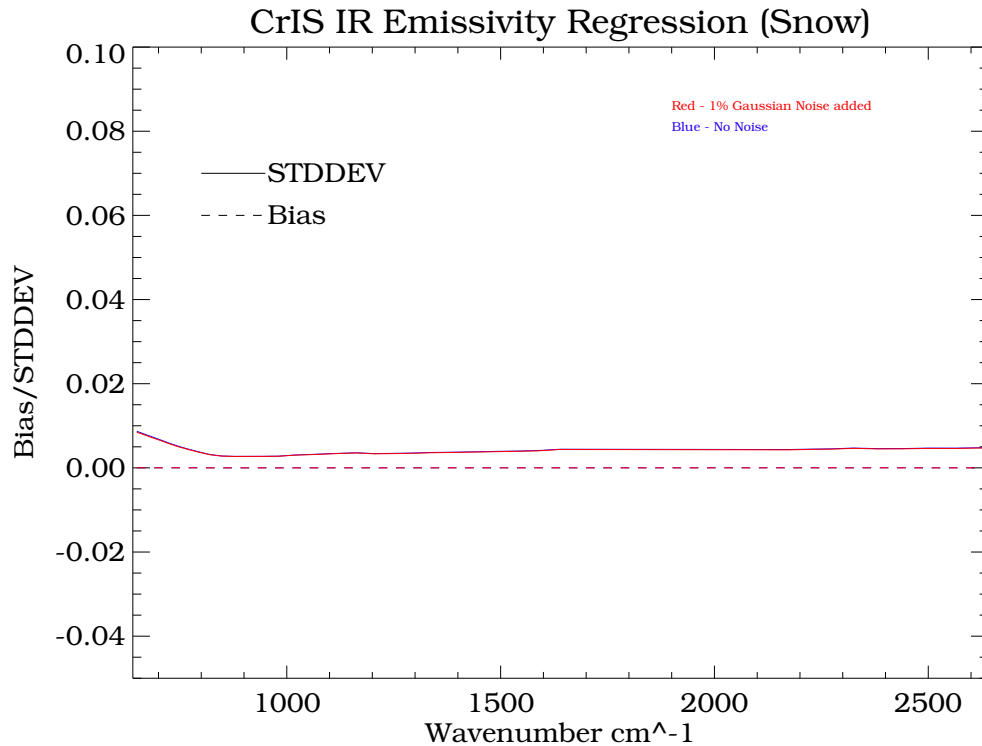


Figure 2.5: Regression bias and standard deviation over ice/snow land.

view angle and slightly on the temperature profile.

MW Tuning Coefficients

Using forward model computations, a tuning coefficient set is computed as an average bias difference of a global sample of observed minus computations (OBS – CALC), for each channel and in the microwave case, scan angle position (for ATMS there are 96 consecutive acquisitions per scanline). In reality, we limit the collection of OBS – CALC samples over a restricted area of the globe, which only includes open ocean, clear sky, day-time and non-high latitude areas, where the collection of correlative “truth” profiles is relatively more reliable. Specifically, the sub-field of view variability is usually higher over land, coastal and broken cloud scenarios, as opposed to the more uniform open ocean and clear sky conditions, hence our choice to restrict the tuning training sample to the more uniform ocean-only and clear-sky areas of the globe. The selection of non precipitating cases is also dictated by the fact that microwave forward

models, in general, do not handle precipitation.

Besides sampling errors, measurement errors can also represent a significant source of uncertainty in the truth. This is the case for high latitude and daytime atmospheric measurements, whether performed by mean of in situ acquisitions (radiosondes) or independent retrievals and re-analyses. Specifically, truth profiles collected over high latitude regimes by mean of Vaisala radiosondes tend to suffer from temperature dependent errors (the colder the temperature, the larger the error) in the form of a significant dry bias in the relative humidity measurements. Furthermore, radiosonde daytime measurements suffer from so called solar arm heating (SAH) errors, originated by radiative heating of the temperature and humidity sensor prior to launch, and resulting in a higher temperature and drier humidity measurements. It has been observed that a temperature difference of 1 degree Celsius between the ambient and the sensor arm corresponds to 4% SAH error in relative humidity. Alternative measurements, such as independent infrared retrievals or re-analyses, suffer from high latitude low signal to noise temperature gradients, besides being subject to large uncertainties in snow/ice infrared emissivity, daytime non local thermodynamic equilibrium and solar reflectivity parameterization. These measurement uncertainties in daytime and cold conditions dictate the necessity to further limit our sampling selection to nighttime and tropical to mid latitude regions only. The ATMS bias tuning is shown in Figure 2.6 as a function of view angle for both ATMS/TDR Block 1.0 and 2.0. This is basically the bias found between the ATMS observations and the calculated or synthetic brightness temperatures derived using a rapid atmospheric transmittance algorithm (RTA) or forward model (Rosenkranz, 1995) and ECMWF over restricted areas of the globe where the effects of land, Polar Regions and precipitation conditions have been removed. Significant differences between Block 1.0 and Block 2.0 bias corrections are observed, mostly associated to a better noise characterization, better instrument calibration and the bias reduction from Rayleigh-Jeans approximation. Figure 2.7 shows the standard deviation of the observed and calculated ATMS brightness temperatures, which is used in the NUCAPS microwave-only retrieval to define the RTA error. Here, it is observed that windows channels at 88.2 and 165.50 GHz show the largest errors, most probably associated to the surface or near surface inhomogeneity.

IR Tuning Coefficients

To correct the IR Radiative Transfer Algorithm (RTA) bias, a set of true cloud-free radiances and the corresponding truths of the atmospheric states, surface parameters are required. We select cases from four arbitrary focus days which meet the requirements. The four focus days are 20 December 2014, 17 February 2015, 21 March

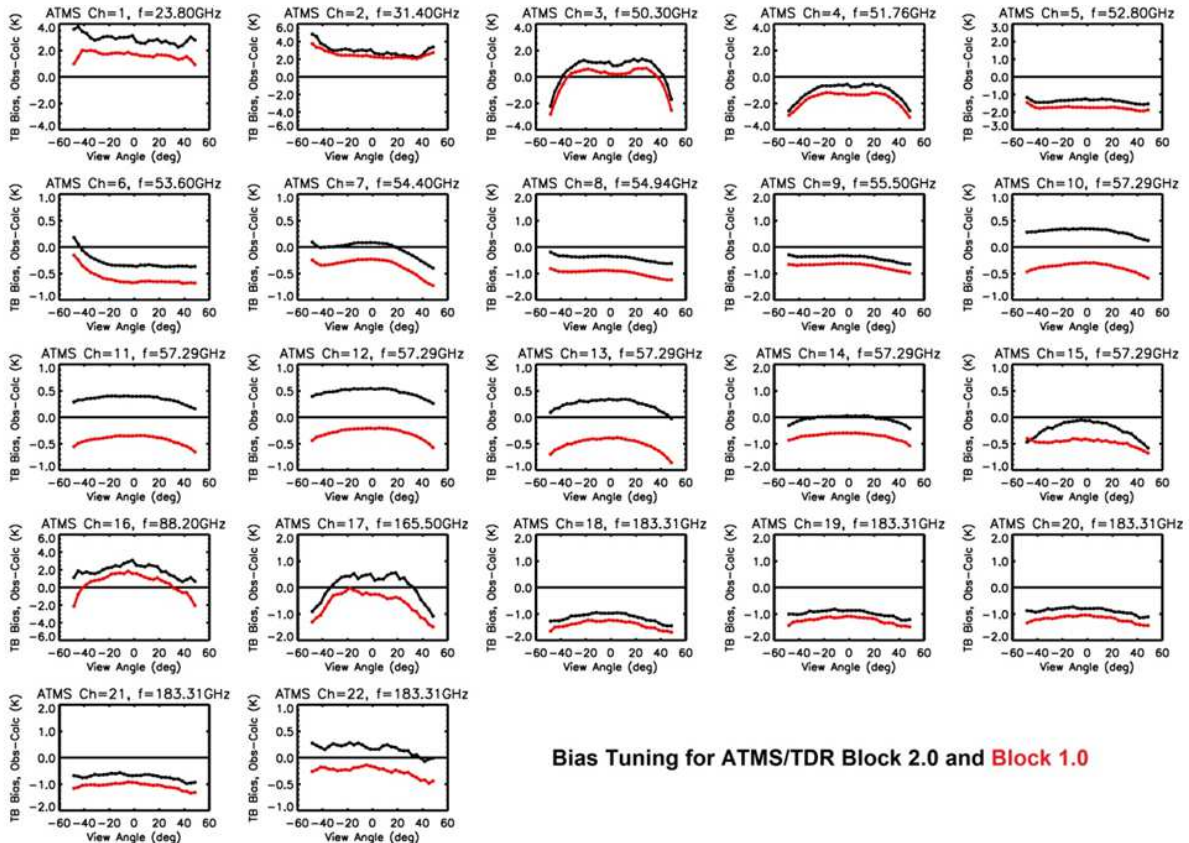


Figure 2.6: ATMS bias tuning correction for channels 1–22, as a function of view angle. Results show the actual bias correction for the ATMS/TDR Block 1.0, and the most recent correction made for ATMS/TDR Block 2.0.

2015, and 9 June 2015. The data sources that we use for this work are SNPP CrIS-FSR IR radiances (converted to brightness temperature), the Visible Infrared Imaging Radiometer Suite (VIIRS) cloud mask products, VIIRS M15 images, ECMWF numerical models, MOPITT CO retrievals and Japan Agency for Marine-Earth Science and Technology (JAMSTEC) trace gas numerical model profiles (including CH_4 and CO_2). To insure the cloud-free requirements, we precisely collocate the geolocation coordinates of CrIS and VIIRS (see Figure 2.8). First, the VIIRS cloud mask intermediate products are applied to select CrIS field of regards (FORs) with at least one clear CrIS field of view (FOV) that is confidently tested and validated without cloud contamination. Secondly, we multiply the VIIRS channel M15 spectral response function on the CrIS full spectral radiances measured by the clear CrIS FOV to reconstruct

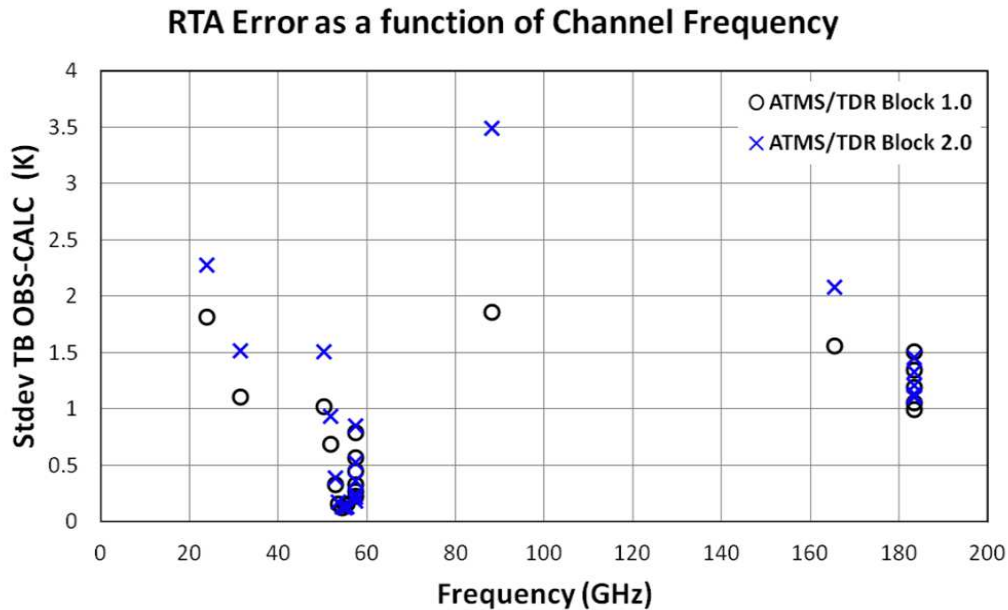


Figure 2.7: ATMS RTA error for channels 1–22. Results show the actual RTA error for the ATMS/TDR Block 1.0, and the most recent correction made for ATMS/TDR Block 2.0.

M15 radiances. Only those cases that the standard deviation of M15 brightness temperature within the clear CrIS FOV less than 0.3 K and the difference between the mean M15 observed brightness temperature and reconstructed M15 brightness temperature less than 1 K are considered as a candidate. As for the constraints of the atmospheric profile domain, we select cases that meet the following requirements:

1. the latitude should be within $\pm 60^\circ$
2. the footprint should anchor at ocean areas
3. the observation should be nighttime

The components of the atmospheric state “truths” are the combinations of the following

1. temperature, water vapor and ozone profiles and surface temperature, surface parameters from collocated ECMWF numerical model, including analysis and 3-hour forecast data

2. collocated CH_4 and CO_2 profiles are from JAMSTEC models
3. collocated CO profiles are from MOPITT retrievals

The composed profiles are ingested in to the SARTA forward model to simulate CrIS clear radiances. After the simulation, further criteria are used to screen out the outliers, those are the differences between simulated radiances (converted to brightness temperature) and observed radiances (converted to brightness temperature) at certain channels, e.g. 900, 751, 757, 784, 1040, 1429, 1491, 1616, 2499 and 2503 cm^{-1} , must less than 1.5 K. Based on all the requirements, there are total 2217 cases selected for IR RTA bias corrections. The channel RTA biases and standard deviations are shown in Figures 2.9 and 2.10, respectively.

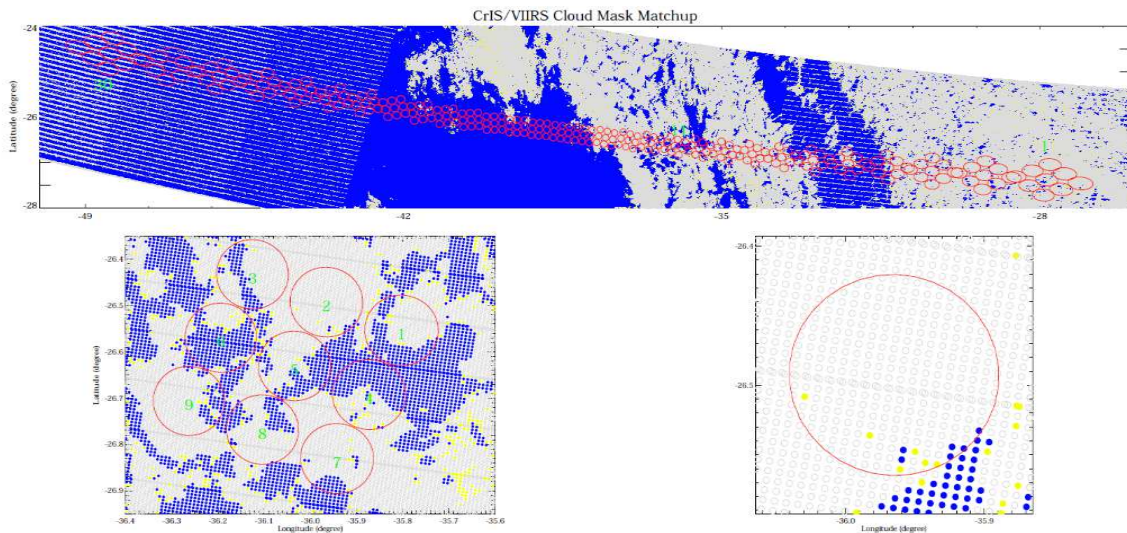


Figure 2.8: The collocation of CrIS FOVs and VIIRS pixels. The red circles (or ovals) represents the CrIS FOVs and the pixel dots are VIIRS pixels (blue: cloudy; yellow: probably cloudy; grey circles: clear). The upper panel shows the one single CrIS scan line. The lower left shows the 11th CrIS FOR of the particular scan line. The lower right even zooms in to show the 2nd FOV of the particular FOR.

The IR tuning for NOAA-20 CrIS is derived from the SNPP IR tuning by using a double difference method. This way allows the retrieval consistency between SNPP and NOAA-20 products. The CrIS observation-minus-simulation biases are calculated using the SARTA (RTA v11) and two days observations on June 20 and 30, 2019 for SNPP and NOAA-20, respectively. The NOAA-20 CrIS tuning is created by

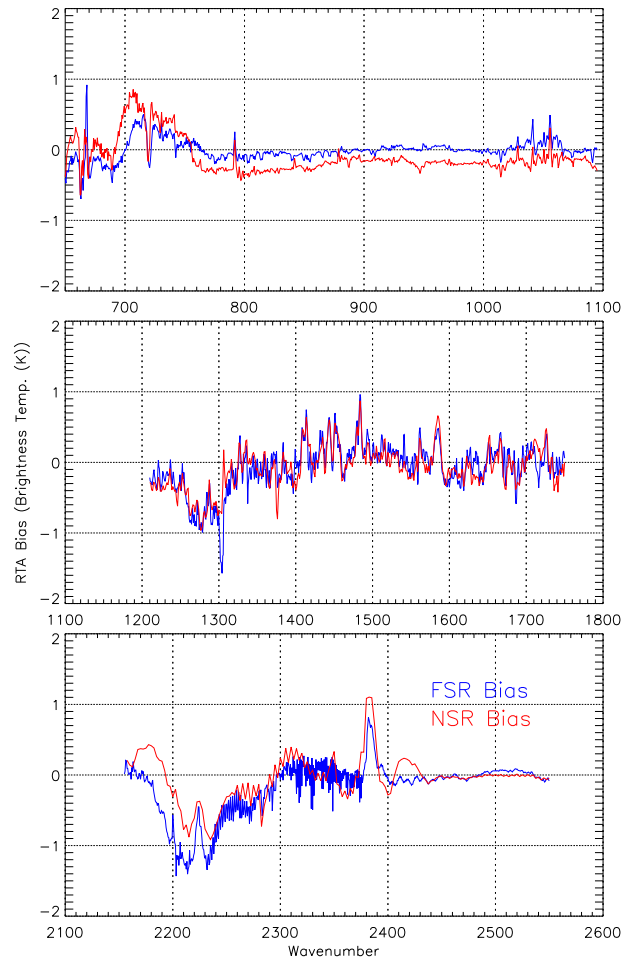


Figure 2.9: The CrIS full spectral-resolution (FSR) RTA bias versus nominal spectral-resolution (NSR) RTA bias. The blue shows the FSR RTA bias and the red shows the NSR RTA bias.

adding the bias between NOAA-20 and SNPP to the SNPP tuning bias (as shown in Fig. 2.11).

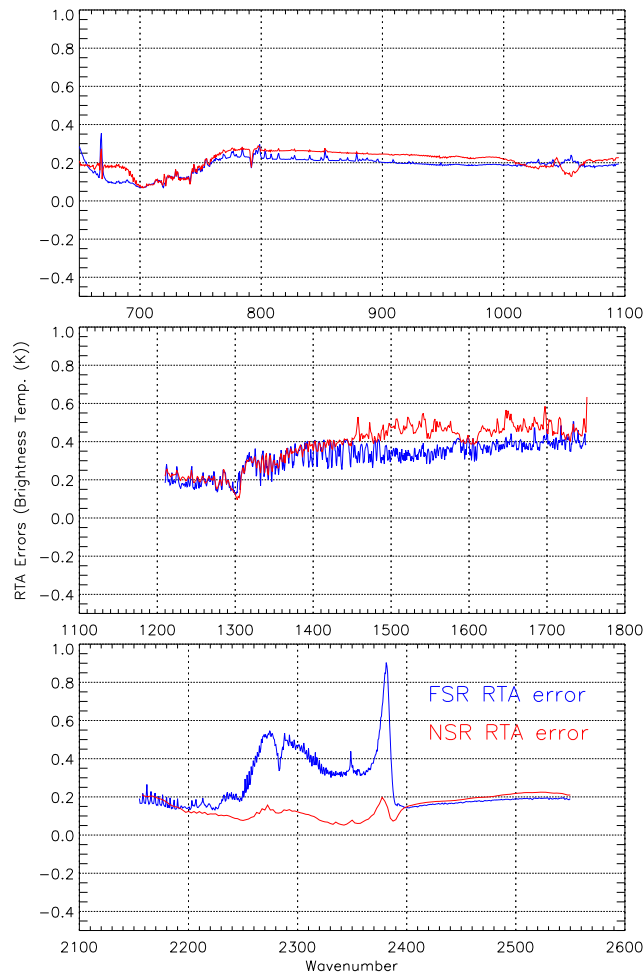


Figure 2.10: The CrIS-FSR RTA error (standard deviation) versus NSR RTA error. The blue shows the FSR RTA error and the red shows the NSR RTA error.

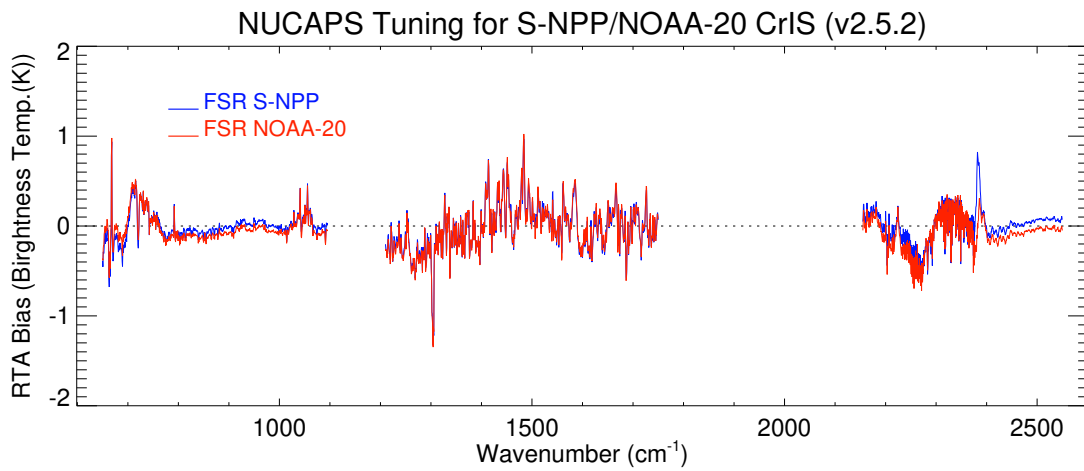


Figure 2.11: The comparison of CrIS-FSR RTA biases for SNPP (blue) and NOAA-20 (red) retrievals.

2.3. Radiative Transfer Models (RTM)

The physical retrieval methodology utilized by the NUCAPS depends on the ability to accurately and rapidly calculate the outgoing radiance based on the state of the surface and the atmosphere. The radiative transfer model consists of a parameterized algorithm to compute atmospheric transmittance, a model for surface brightness temperature, and a model for the reflected downwelling atmospheric emission. The following sections discuss the microwave and infrared radiative transfer models and error estimates.

2.3.1. MW RTM

At the frequencies measured by ATMS, the most important absorbing gases in the atmosphere are oxygen and water vapor. The oxygen molecule has only a magnetic dipole moment, and its lines are intrinsically much weaker than those which result from the electric dipole of water vapor; however, the much greater abundance of oxygen in the atmosphere more than compensates for this difference. When clouds are present, liquid water also plays a role in radiative transfer. However, fair-weather cirrus composed of ice particles small compared to the wavelength are generally transparent to the ATMS frequencies.

Oxygen

O₂ spin-rotation transitions comprise approximately 30 lines between 50 and 70 GHz and an isolated line at 118.75 GHz (which is not observed by AMSU or HSB). Several groups have measured the pressure-broadened widths of the lines in the 50-70 GHz band. The line parameters used for the forward model are from the Millimeter-wave Propagation Model (MPM92) (Liebe et al., 1992). The characteristic of oxygen's microwave spectrum that introduces difficulty for construction of models is the significant degree of line mixing. In MPM92, line mixing was treated by a first-order expansion in pressure. The coefficients for this expansion were determined by a constrained linear fit to laboratory measurements made on an O₂-N₂ mixture over the frequency range of 49-67 GHz and the temperature range 279–327 K, with a noise level of approximately 0.06 dB/km. Within that range, the model represents the measurements to 0.2 dB/km. It is possible that extrapolation to colder temperatures introduces larger errors. Measurements from the NASA ER-2 at 52-56 GHz (Schwartz, 1997) seem to be in agreement with the model, however.

Water Vapor

Water has a weak rotational line at 22.23 GHz that is semi-transparent at normal atmospheric humidity, and a much stronger, opaque line at 183.31 GHz. Intensities of these lines have been calculated and tabulated by Poynter and Pickett (1996 version of JPL line catalog) and Rothman et al. (1998) (HITRAN), among others. The HITRAN intensities are used here. For the 22-GHz line, the JPL intensity is higher than the HITRAN value by 0.3%. There is a measurement by Liebe et al., (1969) (estimated error 0.3%) which is 3.5% lower than the HITRAN value. At 183 GHz, the JPL line intensity is 0.1% higher than HITRAN. Widths have been measured by Liebe et al., (1969) and Liebe and Dillon (1969) at 22 GHz with estimated uncertainty of 1% for both self and foreign-gas broadening; and by Bauer et al., (1989) and Tretyakov et al. (2003) at 183GHz, with uncertainties of 0.5% for self-broadening and 1.0% for foreign-gas broadening, respectively. However, Gamache et al. (1994) concluded from a survey of measurements of many H₂O lines that, in general, measured line widths should be considered to have uncertainties of 10-15%. The line at 183 GHz is a case in which published measurements of width differ significantly, but the value of Tretyakov et al. (2003), which is used here, lies near the centroid of the measurements. At frequencies away from these two lines, microwave absorption by water vapor is predominantly from the continuum, which is attributed to the low-frequency wing of the intense infrared and submillimeter rotational band lines. In the microwave part of the spectrum, the foreign-broadened component of the continuum is stronger than the self-broadened component, for atmospheric mixing ratios. Measurements of continuum absorption as a function of temperature have been made at various frequencies by Liebe and Layton (1987), Godon, et al. (1992) and Bauer et al. (1993, 1995). There are also numerous measurements at single temperatures and frequencies in the laboratory, and in the atmosphere where temperature and mixing ratio are variable. The measurements do not present an entirely consistent picture. Rosenkranz (1998) proposed that the most satisfactory overall agreement with laboratory and atmospheric measurements of the water continuum was obtained with a combination of the foreign-broadened component from MPM87 (Liebe and Layton, 1987) with the self-broadened component from MPM93 (Liebe et al., 1993). The combined model is used here.

Liquid Water

It is useful to distinguish between precipitating and non-precipitating clouds with respect to their interactions with microwaves. Over the range of wavelengths measured by ATMS, non-precipitating droplets (with diameters of 50 μ m or less) can be treated

using the Rayleigh small-droplet approximation. In this regime, absorption is proportional to the liquid water content of the air, and scattering can be neglected. The model for the dielectric constant limits the accuracy of these calculations. The double-Debye model of Liebe et al., (1991) is used here; for temperatures $> 0^\circ\text{C}$, it has an estimated maximum prediction error of 3% between 5 and 100 GHz, and 10% up to 1 THz. Although some measurements of static dielectric constant at temperatures as low as -20°C were used by Liebe et al. to develop their model, its use for supercooled water must be considered to be an extrapolation, with uncertain accuracy. (The model is implemented using the alternate Eq. 2b in Liebe et al.) Precipitation, on the other hand, requires Mie theory to calculate both absorption and scattering. The latter is generally not negligible, and is the dominant term at some wavelengths. In the case of convective storms, scattering from ice at high altitudes is often the most important process. The rapid transmittance algorithm uses only the small-droplet approximation for cloud liquid water, and scattering is not included. For this reason, retrieved profiles with more than 0.5 kg/m^2 cloud liquid water are rejected, as probably rain-contaminated.

MW Rapid Transmittance Algorithm

The modeled brightness temperature T_b received by a space born microwave radiometer over a smooth surface with emissivity ϵ may be expressed as

$$\begin{aligned}
 T_B &= \frac{1}{\omega} \int_0^\infty H(\nu) d\nu \int_0^{P_s} -T(P) \frac{\partial \tau_\nu(0, P)}{\partial P} dP \\
 &+ \epsilon \tau_\nu(0, P_s) T_s + (1 - \epsilon) \tau_\nu(0, P_s) \int_0^{P_s} -T(P) \frac{\partial \tau_\nu(P_s, P)}{\partial P} dP \\
 &+ (1 - \epsilon) \tau_\nu(0, P_s)^2 T_{cb}
 \end{aligned} \tag{2.2}$$

where $H(\nu)$ represents the passband of the radiometer channel of frequency ν , ω is the spectral total width of the passband, $\tau_\nu(P_1, P_2)$ is the transmittance at frequency ν between the pressure levels P_1 and P_2 , $T(P)$ is the atmospheric temperature at level P , T_s and P_s are surface temperature and pressure, and T_{bc} is the cosmic background brightness temperature.

Near real time operations require rapid data processing which precludes the use of a line-by-line transmittance model. The rapid algorithm employed in this study and operationally used at NOAA/NESDIS to process the ATMS, AMSU-A and MHS instruments is the microwave rapid transmittance algorithm developed by Rosenkranz

(1995, 2003) and later validated by Rosenkranz (2006). In this rapid algorithm, the integration over frequency in (1) is replaced by a passband-averaged transmittance $\langle \tau(0, P) \rangle$. The average transmittance between two adjacent pressure levels, P_1 and P_2 , is computed as:

$$\langle \tau(P_1, P_2) \rangle = e^{-(\alpha + \beta V + \gamma L)} \quad (2.3)$$

where V is the vertical column density integral of water vapor between the two levels and L is the cloud liquid vertical column density integral; α represents the opacity of fixed gases (oxygen and nitrogen) in the layer. The coefficients α , β and γ are computed for each layer and channel, given the inputs of V , temperature, pressure and secant of observation angle. Window channels, water vapor channels and oxygen-band channels are considered separately. Each band employs tabular or polynomial approximations to line-wing or near-line absorption from water vapor or oxygen. Absorption by cloud liquid water and ozone is also included. For a complete description of the derivation of α , γ and β the reader can refer to Rosenkranz (1995, 2003).

For oxygen-band channels sounding the atmosphere above 40km, Zeeman splitting produced by the terrestrial magnetic field becomes important. For those channels, transmittance is parameterized as a function of the magnetic field strength B and the angle Θ_B between the direction of propagation and the magnetic field. Rosenkranz (1995, 2003) also provide an in depth description of the transmittance parametrization in presence of Zeeman splitting.

Transmittances are computed for 101 layers between 0.5 and 1100 hPa, chosen with approximately even spacing on $P^{2/7}$. The total transmittance is derived as the product of transmittances (2) for each of those layers. This total transmittance, $\langle \tau(0, P_s) \rangle$, is then used in a simplified form of the radiative transfer equation expressed by:

$$T_B = T_B^{\text{direct}} + \langle \tau(0, P_s) \rangle \left[T_B^{\text{sfsc}} + T_B^{\text{sky}} \left(1 - \frac{T_B^{\text{sfsc}}}{T_s} \right) \right] \quad (2.4)$$

T_B^{direct} represents the simplified version of direct path from surface footprint to satellite:

$$T_B^{\text{direct}} = \int_{P_s}^0 T(P) d\langle \tau(0, P) \rangle \quad (2.5)$$

T_B^{sfsc} is the surface brightness temperature given by the product between the surface emissivity and the skin temperature T_s , and T_B^{sky} is the downward propagating sky brightness temperature (including the cosmic background contribution, T_{cb}) as it would be observed from the surface and represented by:

$$T_B^{\text{sky}} = \int_0^{P_s} T(P) d\langle \tau(P, P_s) \rangle + T_{cb} \langle \tau(0, P_s) \rangle \quad (2.6)$$

Planck's equation for radiant intensity is a nonlinear function of temperature. For microwave frequencies, however, the physical temperatures encountered in the earth's atmosphere lie at the high-temperature asymptote of this function. Hence, as discussed by Janssen (1993), brightness temperature can be used as a surrogate for radiance in the equation of radiative transfer with an accuracy of a few hundredths of a Kelvin, provided that the cosmic background is assigned an effective brightness temperature at frequency of

$$T_{cb} = \frac{h\nu}{2K} \cdot \frac{\exp(h\nu/KT_c) + 1}{\exp(h\nu/KT_c) - 1} \quad (2.7)$$

instead of its actual temperature $T_c = 2.73K$, in order to linearize the Planck's function. It has been shown that this rapid transmittance model requires thirty times less computation than a line-by-line algorithm with an accuracy comparable to or better than the channel sensitivities.

MW ocean surface emissivity model

The polarized ocean surface emissivity for frequency ν , $\epsilon_p(\nu)$ for a flat surface at local thermodynamical equilibrium is defined by:

$$\epsilon_p(\nu) = 1 - r_p(\nu), \quad (2.8)$$

where p is the polarization of the signal, horizontal (h) or vertical (v), and r_p is the square of the Fresnel reflection coefficient for polarization p , defined as:

$$r_h = \left| \frac{\cos \theta - \sqrt{\epsilon - \sin^2 \theta}}{\cos \theta + \sqrt{\epsilon - \sin^2 \theta}} \right|^2, \quad (2.9)$$

and

$$r_v = \left| \frac{\epsilon \cos \theta - \sqrt{\epsilon - \sin^2 \theta}}{\epsilon \cos \theta + \sqrt{\epsilon - \sin^2 \theta}} \right|^2 \quad (2.10)$$

In these equations, ϵ is the dielectric permittivity of saline water (not to be confused with the polarized emissivity, denoted ϵ_p). We employ a revised Debye model, the *Double Debye model*, which is obtained as a linear fit of experimental data for synthetic seawater and at seven different temperatures representative of the world's oceans, in the frequency range 3–105 GHz. An extrapolation is being used for higher frequencies.

The ATMS radiometer front-end scanning optics are of a rotating reflector and fixed feedhorn type design. With this configuration, the polarization vector rotates

with the cross-track scanning reflector. As a result, at any beam position making an angle θ with respect to nadir, the received polarization is a linear combination of the vertical and horizontal polarization vectors.

ATMS channels 1 (23.8 GHz), 2 (31.4GHz) and 16 (88.2GHz) are vertically polarized (perpendicular to the ground track) at nadir and generally *quasi-vertically* polarized at any other viewing angle. All other ATMS channels are *quasi-horizontally* polarized and fully horizontally polarized at nadir (polarization vector parallel to the ground track). The surface emissivity for quasi-vertical and quasi-horizontal polarized channels can be expressed respectively as:

$$\epsilon_v(\nu) = (1 - r_v) \cos^2 \theta + (1 - r_h) \sin^2 \theta, \quad (2.11)$$

and

$$\epsilon_h(\nu) = (1 - r_v) \sin^2 \theta + (1 - r_h) \cos^2 \theta. \quad (2.12)$$

2.3.2. IR RTM

The total monochromatic radiance, $R(\nu, \theta, X)$, at frequency ν , zenith angle θ , for an atmosphere with geophysical state, X , emerging from the top of the atmosphere can be broken into the following components

$$R(\nu, \theta, X) = \underbrace{R_s(\nu, \theta, X)}_{\text{surface}} + \underbrace{R_a(\nu, \theta, X)}_{\text{atmospheric column}} + \underbrace{R_d(\nu, \theta, \theta', X)}_{\text{atmospheric downwelling}} + \underbrace{R_{\odot}(\nu, \theta, \theta_{\odot}, X)}_{\text{reflected solar}}. \quad (2.13)$$

Specifically, $R_s(\nu, \theta, X)$ is the contribution due to the surface radiance, averaged over the footprint, attenuated by the atmospheric column of the observation.

$R_a(\nu, \theta, X) \equiv \sum_{L=1}^{N_L} R_L(\nu, \theta)$ is the sum of all the contributions $R_L(\nu, \theta)$ from all the layers within the IFOV. $R_d(\nu, \theta, X)$ is the contribution due to the downwelling radiation from the entire atmospheric volume reflected by the surface and transmitted through the observed atmospheric column. $R_{\odot}(\nu, \theta, \theta_{\odot}, \rho_{\odot}, X)$ accounts for the transmission of sunlight from the TOA through the atmosphere at angle θ_{\odot} , reflected from the surface, and transmitted out of the atmosphere at angle θ to the spacecraft.

Since the Planck function is linear in the microwave region, Eq. (2.13) can be written in terms of brightness temperatures as well

$$T_B(\nu, \theta) = T_{Bs}(\nu, \theta) + T_{Ba}(\nu, \theta) + T_{Bd}(\nu, \theta) + T_{B\odot}(\nu, \theta). \quad (2.14)$$

Radiance Contribution from the Surface

The radiance emerging at the top of the atmosphere is given by the contributions from the surface and attenuated by the atmospheric transmittance. We will begin by

considering only the radiation upwelling from the surface emission. The component of out-going radiance from the surface is given by a black-body radiance at the surface skin temperature, T_s , multiplied by the surface emissivity, ϵ_ν . The surface radiance must pass through the entire atmosphere and is, therefore, multiplied by the column transmittance from the surface to the top of the atmosphere. The monochromatic out-going surface radiance is given by

$$R_s(\nu, \theta) = \epsilon_\nu B_\nu(T_s) \tau_\nu^\uparrow(P_s, \theta), \quad (2.15)$$

where we employ a short hand notation for the surface to space transmittance

$$\tau_\nu^\uparrow(P_s, \theta) \equiv \tau_\nu(P_s \rightarrow 0, \theta) \quad (2.16)$$

The monochromatic brightness temperature equation for the surface contribution is given by

$$T_{Bs}(\nu, \theta) = \epsilon_\nu T_s \tau_\nu^\uparrow(P_s, \theta) \quad (2.17)$$

and the channel averaged equation for the surface contribution is given by

$$T_{Bs}(n, \theta) = \epsilon_n T_s \tau_n^\uparrow(P_s, \theta) \quad (2.18)$$

The surface component, R_s , is given as

$$R_s(\nu, \theta) = \epsilon_\nu B_\nu(T_s) \tau_\nu^\uparrow(P_s, X, \theta), \quad (2.19)$$

where ϵ_ν is the spectral surface emissivity, $B_\nu(T)$ is the Planck function, $B_\nu(T)$, which is the specific intensity (brightness) of a blackbody emitter given by

$$B_\nu(T) = \frac{\alpha_1 \nu^3}{\exp(\frac{\alpha_2 \nu}{T}) - 1} \quad (2.20)$$

and $\tau_\nu^\uparrow(P_s, X, \theta)$ is the transmittance of the atmosphere from the surface, at pressure P_s to the instrument.

Radiance Contribution from the Atmosphere

For a thin layer of the atmosphere, defined between pressure layers at $p(L)$ and $p(L-1)$, the monochromatic radiance contribution at the top of the atmosphere from the atmospheric layer is analogous to the surface radiance and is given by

$$\begin{aligned} R_L(\nu) &= \mathcal{E}_L B_\nu(\overline{T}_L) \tau_\nu(p_{L-1} \rightarrow 0, \theta) \\ &= [1 - \tau_\nu(p_L \rightarrow p_{L-1}, \theta)] B_\nu(\overline{T}_L) \tau_\nu(p_{L-1} \rightarrow 0, \theta) \\ &= B_\nu(\overline{T}_L) [\tau_\nu(p_{L-1} \rightarrow 0, \theta) - \tau_\nu(p_L \rightarrow 0, \theta)] \\ &= B_\nu(\overline{T}_L) \Delta\tau_{\nu,L}^\uparrow(\theta), \end{aligned} \quad (2.21)$$

where

$$\Delta\tau_{\nu,L}^{\uparrow}(\theta) \equiv \tau_{\nu}(p_{L-1} \rightarrow 0, \theta) - \tau_{\nu}(p_L \rightarrow 0, \theta). \quad (2.22)$$

The term $\mathcal{E} \equiv 1 - \tau_{\nu}(p_L \rightarrow p_{L-1}, \theta)$ in Eq. (2.21) constitutes an *effective emissivity* of the layer. When the layer is opaque the gas emits as a blackbody; however, when completely transmissive (i.e., $\tau_{\nu} = 1$), there is no emission contribution from that layer.

The proper derivation begins with the equation of radiation transfer (e.g., Chandrasekhar, 1950),

$$\frac{\partial R_{\nu}}{\partial \phi_{\nu}} = \frac{1}{\mu} (S_{\nu} - R_{\nu}) \quad (2.23)$$

For an atmosphere in *local* thermal equilibrium with no scattering the radiation source function, $S_{\nu} = B_{\nu}(T)$, can be described by the Planck function. The radiative transfer equation (e.g., see Mihalas, 1978; p. 38) is a function of the optical depth, ϕ_{ν} , and the cosine of the zenith angle, μ ,

$$\frac{\partial R_{\nu}}{\partial \phi_{\nu}} = \frac{1}{\mu} (B_{\nu} - R_{\nu}). \quad (2.24)$$

We can find an integration factor to obtain

$$\frac{\partial R_{\nu}}{\partial \phi_{\nu}} e^{-\phi_{\nu}/\mu} = \frac{B_{\nu}(T)}{\mu} e^{-\phi_{\nu}/\mu} - \frac{R_{\nu}}{\mu} e^{-\phi_{\nu}/\mu}, \quad (2.25)$$

$$\frac{\partial (R_{\nu} e^{-\phi_{\nu}/\mu})}{\partial \phi_{\nu}} = \frac{B_{\nu}(T)}{\mu} e^{-\phi_{\nu}/\mu}. \quad (2.26)$$

The equation can then be integrated directly. The integration constant is the boundary condition, which is the surface term discussed earlier.

$$R_{\nu} = \int_{\infty}^0 \frac{1}{\mu} B_{\nu}[T(z)] e^{-\phi_{\nu}/\mu} d\phi \quad (2.27)$$

We may change the integration parameter from optical depth, ϕ , to either altitude, z , or pressure, p and obtain:

$$e^{-\phi_{\nu}/\mu} \frac{d\phi}{\mu} = \frac{\partial \tau_{\nu}}{\partial z} dz = \frac{\partial \tau_{\nu}}{\partial p} dp \quad (2.28)$$

so that

$$R_{\nu} = \int_0^{\infty} B_{\nu}[T(z)] \frac{\partial \tau_{\nu}}{\partial z} dz \quad (2.29)$$

The atmospheric radiance component, R_a , is the vertical integral of the Planck radiance as seen through the level to space transmittance

$$R_a(\nu, \theta) = \int_{P_s}^0 B_\nu[T(p)] \frac{\partial \tau_\nu^\uparrow(p, X, \theta)}{\partial p} dp \quad (2.30)$$

In remote sounding the contribution of a single channel usually comes from a narrow vertical region in which $\tau \simeq \frac{1}{2}$. For discrete radiative transfer algorithms the total contribution from the atmosphere is given by the sum of the individual layer contributions over the entire isobaric grid

$$R_a(\nu) = \sum_{L=1}^{N_L} R_L(n) = \sum_{L=1}^{N_L} B_\nu(\overline{T}_L) \Delta \tau_{\nu,L}^\uparrow(\theta). \quad (2.31)$$

In the microwave we can utilize the Rayleigh-Jeans approximation for write the total contribution from the atmospheric column in terms of microwave brightness temperature, T_B ,

$$T_{Ba}(\nu) = \sum_{L=1}^{N_L} T_{B,L}(\nu) = \sum_{L=1}^{N_L} \overline{T}_L \Delta \tau_{\nu,L}^\uparrow(\theta). \quad (2.32)$$

In the microwave spectrum used for remote sounding the channel averaged transmittance can be utilized because the spectral characteristics of the species used for sounding (O_2 and H_2) do not interact with interfering species such as water. This simplifies the atmospheric radiance computation and makes the radiative transfer equation much more linear

$$T_{Ba}(n) = \sum_{L=1}^{N_L} T_{B,L}(n) = \sum_{L=1}^{N_L} \overline{T}_L \Delta \tau_{n,L}^\uparrow(\theta). \quad (2.33)$$

Solar Reflected Component

In a non-scattering atmosphere sunlight is absorbed by the atmospheric particles. We utilize the radiative transfer equation (2.23) with the boundary condition (integration constant) equal to the solar radiance at the top of the atmosphere. The solar energy propagates down to the surface at which point it is reflected into the view of the satellite

$$R_\odot = \rho_\odot(\nu, \theta, \theta_\odot) \tau_\nu^\uparrow(p_s, X, \theta, \theta_\odot) \Omega(t) H_\odot(\nu) \cos(\theta), \quad (2.34)$$

where H_\odot is the solar radiance outside the Earth's atmosphere. The reflected solar component requires computation of the transmittance along the bi-directional path

from the sun to the surface, p_s , and back to the spacecraft. For channel radiances the bi-directional transmittance is not equal to the product of the downwelling and upwelling transmittances

$$\int \tau_{\nu}^{\downarrow\uparrow}(p_s, X, \theta, \theta_{\odot}) d\nu \neq \int \tau_{\nu}^{\downarrow}(p_s, X, \theta_{\odot}) d\nu \cdot \int \tau_{\nu}^{\uparrow}(p_s, X, \theta) d\nu \quad (2.35)$$

Ω is the solid angle, given in terms of the Sun's radius and distance. It varies by $\pm 3.4\%$ over the year,

$$\Omega(t) = \pi \cdot \left(\frac{0.6951 \cdot 10^9}{D_{\odot}(t)} \right)^2 \approx 6.79 \cdot 10^{-5} - 0.23 \cdot 10^{-5} \cdot \cos[2\pi(t - t_0)/t_y]$$

where, t is the time of year, t_y is the time the Earth takes to complete 1 orbit (365.25 days), and t_0 is the perihelion date (January 4 or $t_0=4$). The solar surface reflectivity, ρ_{\odot} , is a function of surface type, zenith angle, solar zenith angle, azimuth angle, and wavenumber.

Monochromatic Downwelling Thermal Component

The radiation from an atmospheric layer at $p(L)$ emits radiation in all directions. Some of that radiation reflects off the surface and into the solid angle of observation. The downwelling term requires integration over all zenith angles, θ' , and azimuthal angles, α , and all levels.

$$R_d(\nu, \theta) = \tau_{\nu}^{\uparrow}(P_s, X, \theta) \int_0^{2\pi} \int_0^{\frac{\pi}{2}} \rho_{\nu}(\theta, \theta'; \phi, \phi') \sin(\theta') \cos(\theta') d\theta d\phi \cdot \int_{P_s}^0 B_{\nu}[T(p)] \frac{\partial \tau_{\nu}^{\downarrow}(p, X, \theta')}{\partial p} dp, \quad (2.36)$$

where the thermal bidirectional reflectance distribution function (BRDF), $\rho_{\nu}(\theta, \theta'; \phi, \phi')$, is usually a small number $\simeq 1 - \epsilon_{\nu}$ (except at larger zenith angles and in the microwave). Effectively, there is a product of up-welling and downwelling transmittance so that this term is only important in channels in which the transmittance is $\approx \frac{1}{2}$. The short hand notation for the surface to space transmittance Eq. (2.16) has been employed and a short hand notation for the downwelling layer transmittance is

$$\Delta \tau_{\nu}^{\downarrow}(L, \theta') \equiv \tau_{\nu}[p(L-1) \rightarrow p(L), \theta'] \quad (2.37)$$

$$= \tau_{\nu}[p(L-1) \rightarrow P_s, \theta'] - \tau_{\nu}[p(L) \rightarrow P_s, \theta']. \quad (2.38)$$

But the monochromatic downwelling transmissivity is related to the upwelling transmissivity by

$$\tau_\nu[p(L) \rightarrow P_s, \theta'_\nu] = \frac{\tau_\nu(P_s \rightarrow 0, \theta'_\nu)}{\tau_\nu[p(L) \rightarrow 0, \theta'_\nu]} \quad (2.39)$$

so that

$$\Delta\tau_\nu^\downarrow(L, \theta'_\nu) = \frac{\tau_\nu(P_s \rightarrow 0, \theta'_\nu)}{\tau_\nu(p(L) \rightarrow 0, \theta'_\nu)} - \frac{\tau_\nu(P_s \rightarrow 0, \theta'_\nu)}{\tau_\nu(p(L-1) \rightarrow 0, \theta'_\nu)}. \quad (2.40)$$

Also, since the lines are resolved and not overlapping the channel averaged downwelling transmittance can be written in terms of the upwelling level-to-space channel averaged transmittances in the form shown in Eq. (2.40). The order of integration can be changed in Eq. (2.36) as

$$\begin{aligned} R_d(\nu, \theta) &= \tau_\nu^\uparrow(P_s, X, \theta) \int_{P_s}^0 B_\nu[T(p)] \frac{\partial \tau_\nu^\downarrow(p, X, \theta')}{\partial p} dp \\ &\cdot \int_0^{2\pi} \int_0^{\frac{\pi}{2}} \rho_\nu(\theta, \theta'; \phi, \phi') \sin(\theta') \cos(\theta') d\theta d\phi. \end{aligned} \quad (2.41)$$

Infrared Downwelling Term

The infrared downwelling term has been felt by anyone who has stood out on a warm humid day. The warmth of the hot atmosphere can be larger than the direct solar radiation in the mid- to far-IR. For a surface-based uplooking or downlooking instrument the thermal downwelling integral must be computed accurately. For a space-borne measurement only certain channels will have a measurable thermal downwelling radiation and even those channels the effect is still small. Many approximations are employed given that the surface reflectance, ρ , is a small number, usually only a few % for normal scan angles $\lesssim 40^\circ$. The term becomes important when $\tau \simeq \frac{1}{2}$ because when the atmosphere is opaque ($\tau \rightarrow 0$) the sensor cannot “see” the surface and when the atmosphere is transmissive ($\tau \rightarrow 1$) the downwelling radiance is small (again, for smaller incidence angles $\lesssim 40^\circ$). ϕ' and θ' have been approximated by an effective diffusive angle by the mean value theorem, and the dependence on azimuthal angle can be small over Lambertian surfaces (e.g., land), where integral with respect to $\int_0^{2\pi} d\phi$ can be replaced by 2π .

It has thus been assumed that the thermal reflectivity may be represented by a mean value so that Eq. (2.36) can be written as

$$R_d(\nu, \theta) \simeq \tau_\nu^\uparrow(P_s, X, \theta) \rho(\nu, \theta) \pi R_\nu^\downarrow \quad (2.42)$$

The factor of π arises by assuming azimuthal symmetry, $\int d\alpha = 2\pi$ and assuming we can represent the integral of zenith angle by a diffusive term $\int \cos(\theta) \sin(\theta) d\theta = 1/2$.

In Kornfield and Suskind (1977), the downwelling term is shown to be simplified as follows. First, we can insert the surface radiance into the integral

$$R_{\nu}^{\downarrow} = \int_{\tau(P_s)}^1 B_{\nu}(T) d\tau^{\downarrow} = \int_{\tau(P_s)}^1 B_{\nu}(T_s) d\tau^{\downarrow} + \int_{\tau(P_s)}^1 [B_{\nu}(T) - B_{\nu}(T_s)] d\tau^{\downarrow} \quad (2.43)$$

the left hand integral can be written exactly

$$R_{\nu}^{\downarrow} = B_{\nu}(T_s) [1 - \tau_{\nu}^{\downarrow}(P_s)] + \int_{\tau(P_s)}^1 [B_{\nu}(T) - B_{\nu}(T_s)] d\tau^{\downarrow} \quad (2.44)$$

Most of the absorption takes place very low in the atmosphere, say in the lowest 150 hPa (*i.e.*, between 1000 and 850 hPa) and $B_{\nu}(\tau) - B_{\nu}(T_s)$ is a slowly varying function, therefore, the integral is adequately represented by the mean value theorem

$$R_{\nu}^{\downarrow} \simeq B_{\nu}(T_s) [1 - \tau_{\nu}^{\downarrow}(P_s)] + \overline{B_{\nu}(T) - B_{\nu}(T_s)} [1 - \tau_{\nu}^{\downarrow}(P_s)] \quad (2.45)$$

where $\overline{B_{\nu} - B_{\nu}(T_s)}$ is the mean difference between atmospheric Planck function and the surface Planck function over the range of most absorption. This equation can be re-written in the form of

$$R_{\nu}^{\downarrow} \simeq F_{\nu} B_{\nu}(T_s) [1 - \tau_{\nu}^{\downarrow}(P_s)] , \quad \text{where} \quad F_{\nu} \equiv 1 + \frac{\overline{B_{\nu} - B_{\nu}(T_s)}}{B_{\nu}(T_s)} . \quad (2.46)$$

F_{ν} differs from unity to the extent that the mean value of the atmospheric Planck function differs from the surface Planck function.

Now it is seen that monochromatic downwelling radiance is a function of the product of τ and $(1 - \tau)$. The maximum thermal downwelling radiation will occur when $\tau \approx 1/2$. For channel averaged transmittances this is not necessarily true. In the top example the transmittance is constant across the channel integration whereas in the bottom example the channel is a mixture of opaque and transmissive components. In the top case, $\tau \cdot (1 - \tau)$ is simply equal to $1/4$, as expected. But in the bottom case τ is zero everywhere where $1 - \tau$ is unity and vice-a-versa. Therefore, the product is zero.

Therefore, the calculation of $\tau \cdot (1 - \tau)$ needs to be done in a channel averaged sense; however, we will show shortly that this usually introduces a small error. Given that the entire downwelling radiance is small at the spacecraft the error is tolerable. We can assume that the integral of the monochromatic product of τ is related to the channel averaged product with a correlation factor, and this will be absorbed into the F_{ν} factor. Inserting Eq. (2.46) into Eq. (2.42) yields

$$R_d(\nu, \theta) = \pi \rho_\nu(\theta, \bar{\theta}_i) B_\nu(T_s) F_\nu \tau_\nu(p_s, \theta) [1 - \tau_\nu(p_s, \bar{\theta})] . \quad (2.47)$$

A better fitting equation for channel averaged radiances might be

$$R_d(i, \theta) = \pi \rho_i(\theta, \bar{\theta}_i) B_{\nu_i}[T(\bar{p}_i)] F_i \tau_i(p_s, \theta) [1 - \tau_i(p_s, \bar{\theta}_i)] \quad (2.48)$$

where p_i is an effective pressure of downwelling for channel i . Each channel could have an effective diffusive angle or the effective diffusive angle, θ_i , could be defined w.r.t. the angle of observation, θ .

It may also be assumed that the bidirectional reflectance is given by either $\rho_i(\theta, \bar{\theta}_i) = (1 - \epsilon_i)/\pi$ for nighttime and long-wave (i.e., $\nu_i < 2300 \text{ cm}^{-1}$) or $\rho_i(\theta, \bar{\theta}_i) = \rho_i(\theta, \theta_\odot)$ for daytime short wave channels. To estimate the thermal downwelling term we can calculate an approximate form of the downwelling term using the nadir rapid algorithm

$$R_d(\nu, \theta) = \frac{1}{2} [1 - \epsilon(\nu)] \tau(p_s) [1 - \tau(p_s)] B_\nu[T(\bar{p})] , \quad (2.49)$$

where $\bar{p} = 700 \text{ hPa}$. To first order, if this effect is ignored entirely, a larger ϵ_i would be determined and radiance residuals would be smaller.

Rapid Transmittance Algorithm (RTA)

This fast transmittance model is based on methods developed and used by Larry McMillan, Joel Susskind, and others. An introduction to the theoretical development of the approximations employed can be found in: McMillin and Fleming (1976), Hannon et al. (1996), and Strow et al. (1998, 2003).

2.4. Microwave Retrieval Algorithm

The NUCAPS microwave (MW) module is a heritage algorithm of the AIRS Science Team microwave retrieval algorithm (Rosenkranz, 2001, 2006). The reader is referred to the AIRS ATBD for an in depth description of the subject of this chapter.

2.4.1. Precipitation Flags, Rate Retrieval and ATMS Corrections.

The precipitation algorithm produces the following: (1) flags indicating possible precipitation-induced perturbations impacting ATMS channels 5, 6, 7, 8, and 9, (2) estimates of corrections that may, at the user's option, be applied to ATMS brightness temperatures for channels 5, 6, 7, 8 and 9, to compensate for precipitation, if present, and (3) a precipitation-rate retrieval (mm/h) for each 50-km ATMS spot which was tuned for mid-latitudes using all-season NEXRAD data.

Precipitation Flags

The objective of the flags for each of ATMS channels 5–9 is to alert data users to the possibility that retrievals based on these microwave channels might be impacted by precipitation. The four possible flag states are given by the following

- Flag = 0: The magnitude of the detected precipitation perturbations (if any) are less than 0.5 K.
- Flag = 1: Small perturbations are present (nominally between 0.5 and 2 K), which are approximately correctable.
- Flag = 2: Estimated ATMS precipitation-induced brightness temperature perturbations for this channel may exceed 2 K in magnitude, so perturbation corrections are less reliable.
- Flag = -1: It is unknown whether perturbations due to precipitation are present (e.g., surface elevation greater than 2 km); these perturbations are discussed further later in this chapter.

Figure 2.12 shows the ability of the precipitation flag to detect precipitation conditions. Those regions where the MW-Only retrieval fails (red regions) are highly correlated with precipitation conditions as has been evaluated using the MiRS rainfall rate product as a reference.

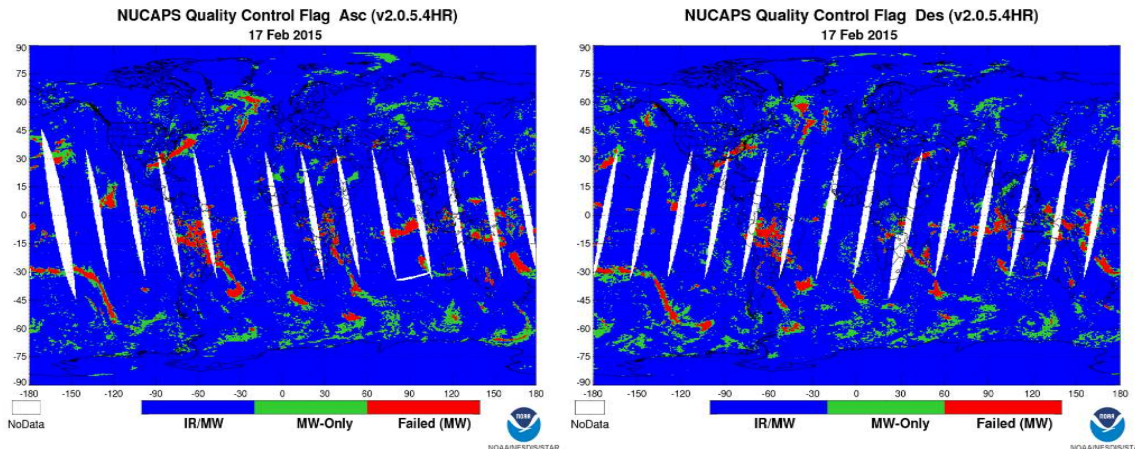


Figure 2.12: NUCAPS quality control flag showing regions where the IR/MW retrieval converges (blue regions) and where the MW-Only retrieval fails (red regions) for the ascending (left figure) and descending (right figure) satellite modes and for the NUCAPS version 2.0.5.4.

Perturbation Corrections

Perturbation corrections are entirely based on the methodology employed for the AMSU instrument. The reader is referred to the AIRS ATBD and the reference therein for a complete description of the methodology.

Perturbation corrections are estimated for ATMS Channels 5–9. In addition, for each ATMS beam position a precipitation-rate estimate (mm/h) is provided when flag states 0, 1, or 2 exist for ATMS channel 5 (52.8 GHz). Users of ATMS data for temperature profile retrievals should use brightness temperatures flagged with 2 or –1 with caution, even if the suggested perturbation corrections are employed. These perturbations are computed for ATMS channels 5–9 at 50-km resolution using the algorithm discussed further down. It should be noted that 52.8 GHz brightness temperatures can suffer warm perturbations over ocean due to low altitude absorption and emission by clouds or precipitation. Such warm perturbations could be flagged and corrected as are the cold perturbations. The 23.8/31.4 GHz combination could be used to validate the locations of such excess absorption and perturbations over ocean.

Rain Rate Retrieval Algorithm

The rain rate retrieval algorithm is an adaptation of the AQUA AMSU-A AMSU-B algorithm. The reader is referred to the AIRS ATBD for an in depth description of this

methodology.

Accurate remote sensing of precipitation rate is challenging because the radiometric signatures of irregularly formed hydrometeors can depend strongly on their distributions in size, temperature, ice content and structure. As a result, all active and passive microwave remote sensing methods rely on the statistical regularity of precipitation characteristics. Experimental validation typically involves comparisons with rain gauges, radar, and other sensors, each of which has its own limitations. The primary precipitation-rate retrieval products of ATMS are 15- and 50-km resolution contiguous retrievals over the viewing positions of ATMS within 43° of nadir. The two outermost 50-km viewing positions (six outermost for 15-km) on each side of the swath are currently omitted due to their grazing angles. The algorithm architectures for these two retrieval methods are presented below.

The 15-km resolution precipitation-rate retrieval algorithm begins with identification of potentially precipitating pixels. All 15-km pixels with brightness temperatures at 183 ± 7 GHz that are below a threshold T_7 are flagged as potentially precipitating, where

$$T_7 = 0.667 (T_{53.6} - 248) + 252 + 6 \cos(\theta) \quad (2.50)$$

and where θ is the satellite zenith angle. If, however, the spatially filtered brightness temperature $T_{53.6}$ at 53.6 GHz is below 249 K, then the brightness temperature at 183 ± 3 GHz is compared instead to a different threshold T_3 , where

$$T_3 = 242.5 + 5 \cos(\theta). \quad (2.51)$$

This spatial filter picks the warmest spot within an array of ATMS pixels. The 183 ± 3 GHz band is used to flag potential precipitation when the 183 ± 7 GHz flag could be erroneously set by low surface emissivity in very cold dry atmospheres, as indicated by $T_{53.6}$. These thresholds T_7 and T_3 are slightly colder than a saturated atmosphere would be, therefore lower brightness temperatures imply the presence of a microwave-absorbing cloud. If the locally filtered $T_{53.6}$ is less than 242 K, then the pixel is assumed not to be precipitating. Within these flagged regions strong precipitation is generally characterized by cold cloud-induced perturbations of the ATMS tropospheric temperature sounding channels in the range 52.5–55.6 GHz. Examples of 183 ± 7 GHz data and the corresponding cold perturbations at 52.8 GHz are illustrated in Figures 5.3(a) and (c), respectively, of the AIRS ATBD (see reference). These 50-km resolution 52.8 GHz perturbations $\Delta T_{50,52.8}$ are then used to infer the perturbations $\Delta T_{15,52.8}$ [see Figure 5.3(d) of AIRS ATBD] that might have been observed at 52.8 GHz with 15-km resolution had those perturbations been distributed spatially in the same way as the cold perturbations observed at either 183 ± 7 GHz or 183 ± 3 GHz, the choice between these two channels being the same as described

above. This requires the bi-linearly interpolated 50-km AMSU data to be resampled at the HSB beam positions. These inferred 15-km perturbations are computed for five ATMS channels using:

$$\Delta T_{15,54} = (\Delta T_{15,183} / \Delta T_{50,183}) \Delta T_{50,54} . \quad (2.52)$$

The perturbation $\Delta T_{15,183}$ near 183 GHz is defined to be the difference between the observed brightness temperature and the appropriate threshold given above. The perturbation $\Delta T_{50,54}$ near 54 GHz is defined to be the difference between the limb and surface-corrected brightness temperature and its Laplacian-interpolated brightness temperature based on those pixels surrounding the flagged region (Staelin and Chen, *IEEE Trans. Geosci. Remote Sensing*, **38**, 2000). Limb and surface-emissivity corrections to nadir for the five 54-GHz channels are produced by neural networks for each channel; they operate on nine AMSU-A channels above 52 GHz, the cosine of the viewing angle Φ from nadir, and a land-sea flag (see Figure 5.2 of AIRS ATBD). They were trained on 7 orbits spaced over one year for latitudes up to $\pm 55^\circ$. Inferred 50- and 15-km precipitation-induced perturbations at 52.8-GHz are shown in Figures 5.3(c) and (d), respectively, of AIRS ATBD, for a frontal system. Such estimates of 15-km perturbations near 54 GHz help characterize heavily precipitating small cells.

Such inferred 15-km resolution perturbations at 52.8, 53.6, 54.4, 54.9, and 55.5 GHz are then combined with (1) the 183 ± 1 -, ± 3 -, and ± 7 GHz 15-km ATMS data, (2) the leading three principal components characterizing the original five corrected 50-km ATMS temperature brightness temperatures, and (3) two surface-insensitive principal components that characterize the window channels at 23.8, 31.4, 50.3, and 89 GHz, plus the 166.31 and the five 183 GHz channels. All 13 of these variables, plus the secant of the satellite zenith angle θ , are input to the neural net used for 15-km precipitation rate retrievals, as shown in Figure 5.2 of AIRS ATBD. This network was trained to minimize the rms value of the difference between the logarithms of the ATMS and NEXRAD retrievals; use of logarithms prevented undue emphasis on the heaviest rain rates, which were roughly three orders of magnitude greater than the lightest rates. Adding 1 mm/h prevented undue emphasis on the lightest rates. NEXRAD precipitation retrievals with 2-km resolution were smoothed to approximate Gaussian spatial averages that were centered on and approximated the view-angle distorted 15- or 50-km antenna beam patterns. The accuracy of NEXRAD precipitation observations are known to vary with distance, so only points beyond 30 km but within 110 km of each NEXRAD radar site were included in the data used to train and test the neural nets. Eighty different networks were trained using the Levenberg-Marquardt algorithm, each with different numbers of nodes and water vapor principal components. A network with nearly the best performance over the testing data set

was chosen; it used two surface-blind water vapor principal components, and only slightly better performance was achieved with five water vapor principal components with increased surface sensitivity. The final network had one hidden layer with 5 nodes that used the tanh sigmoid function. These neural networks are similar to those described by Staelin and Chen (*IEEE TGARS*, **38**(5), 2000). The resulting 15-km resolution precipitation retrievals are then smoothed to yield 50-km retrievals. The 15-km retrieval neural network was trained using precipitation data from the 38 orbits listed in Table 5.1.1. Each 15-km pixel flagged as potentially precipitating using 183 ± 7 GHz or 183 ± 3 GHz brightness temperatures was used either for training, validation, or testing of the neural network. For these 38 orbits over the United States 15,160 15-km pixels were flagged and considered suitable for training, validation, and testing; half were used for training, and one-quarter were used for each of validation and testing, where the validation pixels were used to determine when the training of the neural network should cease. Based on the final ATMS and NEXRAD 15-km retrievals, approximately 14 and 38 percent, respectively, of the flagged 15-km pixels appear to have been precipitating less than 0.1 mm/h for the test set.

2.4.2. MW-Only Profile Retrieval Algorithm

The “MW-only” initial guess profile retrieval algorithm derives temperature, water vapor and non-precipitating cloud liquid water profiles from ATMS brightness temperatures without using IR data. This module was originally intended to provide the starting point for the cloud-clearing and retrieval algorithm but has been later replaced by a cloudy regression solution. Nonetheless, ATMS has improved spectral resolution and coverage with respect to previous AMSU/HSB and AMSU/MHS instruments. Since the ATMS retrieval performance is still under exam, it was decided to leave it as part of the NUCAPS processing flow.

The MW-only retrieval algorithm is an iterative algorithm in which the profile increments are obtained by the minimum-variance method, using weighting functions computed for the current temperature and moisture profiles with the rapid transmittance algorithm described later in this document. The input vector of measured brightness temperatures is accompanied by an input validity vector whose elements are either one or zero. This provides a way of handling missing or bad data.

Preliminary Surface Type Classification

The surface classification algorithm is diagrammed in Figure 5.4 of AIRS ATBD. The classification rules are from Grody et al. (2000), and make use of discriminant functions that are linear combinations of ATMS channels 1, 2, 3, and 16. If sea ice is

indicated by the classification algorithm, then its concentration fraction is estimated from a linear operation on channels 1, 2, and 3. If the surface type is glacier or snow-covered land, then the snow or ice fraction is estimated using channels 3 and 16. Parameters of the surface brightness model are assigned according to surface type as in Table 5.1. *A priori* emissivities for the ice and snow types were estimated from NOAA-15 and Aqua data. For land $\epsilon_0 = 0.95$ at all frequencies; for seawater, the dielectric constant model of Ellison et al. (2003) was used to compute the emissivity of a flat surface viewed in the polarization of the ATMS radiometer.

Atmospheric Moisture and Condensation Model

Brightness temperatures at the ATMS channels 16–22 depend on the vertical profile of atmospheric opacity relative to temperature, but do not by themselves distinguish, at any given altitude, between opacity due to water vapor and opacity due to liquid water. However, the physics of water vapor condensation add some *a priori* information or constraints. Cloud coverage is parameterized as in a stratiform condensation model, where a relative humidity threshold determines the onset of condensation. Although the water vapor profile is saturated within the cloudy part of the field of view, it is assumed that the condensation process is not spatially resolved, hence the threshold is less than 100% relative humidity. Currently, the threshold is set to 85%.

In the condensation model, the vapor and cloud liquid water density profiles are both linked to a single parameter H . When $H \leq 85\%$, H is equal to relative humidity; in the range 85% to 115%, changes from a water-vapor variable to liquid-water, and values of H greater than 115% increase liquid water while the vapor remains at saturation. Because convergence, to be discussed later, is determined from the brightness temperature residuals, which in turn are computed using the vapor and liquid column densities, the role of H in this algorithm is only to introduce the *a priori* statistics and constraints. The average vapor density in the field of view is related to H by

$$\rho_v = \frac{\rho_s}{10} [\text{ramp}(H, 10) - f(H)], \quad (2.53)$$

where ρ_s is the saturation value of mixing ratio and

$$\text{ramp}(x, c) \equiv x, \quad x \geq c, \quad (2.54)$$

$$\text{ramp}(x, c) \equiv c \exp(x/c - 1), \quad x < c, \quad (2.55)$$

and

$$f(H) = \text{ramp}(H - H_L, 6). \quad (2.56)$$

Thus, the value of ρ_v/ρ_s lies between zero and $H_L/100$. the liquid water mixing ratio averaged over the field of view is assumed to be given by:

$$\rho_L = c_1 f(H) \quad (2.57)$$

where c_1 is a coefficient equivalent to a liquid/air mass mixing ratio of 10^{-5} %.

The saturation vapor mixing ratio is computed from the temperature profile by the formula of Liebe (1981). Saturation is calculated with respect to liquid water (by extrapolation) even when the temperature is below 273 K. This model therefore allows supercooled liquid water and water vapor greater than the saturation value with respect to ice.

Estimation of Surface Brightness and Atmospheric Moisture

This section is taken from the AIRS ATBD, Chapter 5 and describes an algorithm based on retrieval methods described by Wilheit (1990), Kuo et al. (1994), Wilheit and Hutchison (1997), and Rosenkranz (2006). It uses ATMS channels 1, 2, 3, 16–22. The measurements are weighted averages over 3×3 spatial arrays which approximate the AMSU-A field of view. The H profile, H_L , and four surface parameters T_0 , T_1 , T_2 , and p_g are concatenated into a vector Y . The parameter p_g when the surface type is either water or coastline, determines the secant ratio ρ by:

$$\rho = \frac{\sec(\Theta_{\text{ref}})}{\sec(\Theta)} = 1 + \text{ramp}(p_\rho, 0.02). \quad (2.58)$$

The cost function to be minimized is given by

$$J = (\hat{Y} - Y_0)^T \mathbf{S}_y^{-1} (\hat{Y} - Y_0) + (\hat{T}_B - T_B - \Delta T_B)^T (\mathbf{S}_f - \mathbf{S}_e)^{-1} (\hat{T}_B - T_B - \Delta T_B), \quad (2.59)$$

in which \hat{Y} is the retrieved estimate of Y , Y_0 is its *a priori* value and \mathbf{S}_y is its covariance matrix with respect to *a priori* T_0 , T_B is a vector of the eight measured antenna temperatures, \mathbf{S}_e is their error covariance matrix (assumed diagonal), ΔT_B is the tuning correction for antenna side lobe effects and possible transmittance error, \hat{T}_B is a calculated brightness temperature vector computed from the current values of temperature, moisture and surface brightness, and \mathbf{S}_f is a diagonal covariance matrix which approximately represents errors in \hat{T}_B resulting from errors in the temperature profile retrieval and tuning. The retrieved estimate of Y (i.e., \hat{Y}) is obtained by Newtonian iteration (see Rodgers, 1976), except that Eyres (1989) method of damping is used to avoid large relative humidity increments, because of the nonlinearity of the problem.

Iteration Procedure and Convergence Tests

Convergence is tested separately for the temperature channels and for the moisture/surface channels. Iteration of either part of the algorithm is suspended when one of the following conditions is met : (1) the computed brightness temperature vector T_B meets the closure criterion; or (2) when successive computations of the residuals change by less than 1% for temperature channels and 2% for water vapor channels of a given threshold; or (3) when the number of iterations exceeds a preset limit, which is 12 for the temperature channels and 16 for the moisture/surface channels. Typically, iteration of the temperature profile ceases after one or two iterations, but the moisture profile often requires six or more iterations.

Given the previous estimate of temperature or water vapor given by \hat{P}_{n-1} (which is \hat{P}_0 on the first iteration), the next estimate of temperature or water vapor is obtained by Newtonian iteration, as shown in Equation (2.60) where a method of damping (represented by δ) is used for water vapor to avoid large relative humidity increments because of the nonlinearity of the problem. For temperature no damping is used ($\delta = 1$)

$$\hat{P}_n = \hat{P}_{n-1} - \delta(\hat{P}_{n-1} - \hat{P}_0) + \delta S_P W_P^T X_P. \quad (2.60)$$

In Equation (2.60), S_P is covariance matrix with respect to \hat{P}_0 , W_P is the Jacobian matrix (matrix of derivatives of brightness temperatures with respect to the atmospheric parameter P), computed and updated for the state represented by \hat{P}_{n-1} . The X_P term in Equation (2.60) is the solution vector as described in Rosenkranz (2001). Figures 2.13 and 2.14 show global maps of the atmospheric temperature and water vapor retrieved by the NUCAPS MW-only algorithm.

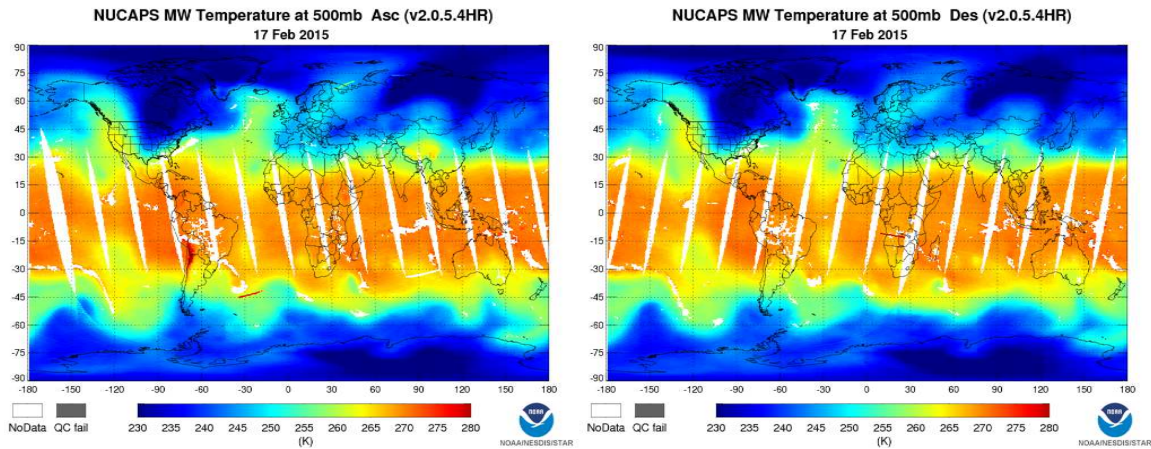


Figure 2.13: Temperature at 500 hPa for the ascending (left plot) and descending (right plot) satellite modes, retrieved by the NUCAPS MW-only retrieval (offline v2.0.5.4).

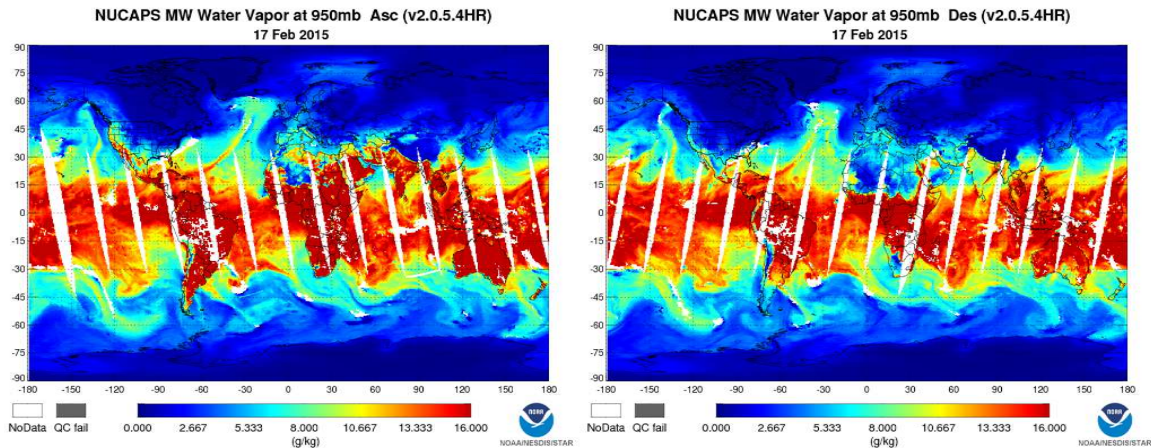


Figure 2.14: Water Vapor at 950 hPa for the ascending (left plot) and descending (right plot) satellite modes, retrieved by the NUCAPS MW-only retrieval (offline v2.0.5.4).

2.5. Regression Retrieval

2.5.1. Post-Launch First Guess Regression Procedure

NOAA/NESDIS uses an eigenvector global regression procedure to provide fast and accurate initial guesses for temperature and moisture profiles as well as surface emissivity and reflectivity using simulated CrIS data. Eigenvector regression for atmospheric sounding was first demonstrated by Smith and Woolf (1976). It is assumed that all independent CrIS radiances have been preprocessed by the cloud clearing module described in the last section. Eigenvectors are computed from a training dataset of radiances that have been normalized by the CrIS expected noise and are used as basis functions to represent the CrIS radiometric information. Eigenvectors are commonly referred to as empirical orthogonal functions (EOFs) in the literature, a convention that will be adopted throughout the remainder of this section. Because of the large number of channels measured by CrIS, the eigenvector form of regression is crucial for exploiting the information content of all channels in a computationally efficient form. By representing radiometric information in terms of a reduced set of EOFs (much fewer in number than the total number of instrument channels) the dimension of the regression problem is reduced by approximately one order of magnitude. Another advantage of using a reduced set of EOFs is that the influence of random noise is reduced by elimination of higher order EOFs which are dominated by noise structure. It should be noted that if all EOFs are retained as basis functions the eigenvector regression reduces to the ordinary least squares regression solution in which satellite measurements are used directly as predictors. The mathematical derivation of the EOF regression coefficients is detailed in the following sub-sections.

Generating the Covariance Matrix and Regression Predictors

A training ensemble of temperature, humidity, and ozone profile data are used to generate radiances for all CrIS channels that meet specified instrument performance. Expected instrumental noise is added to the simulated radiances. Note that real observations will be used after launch to generate the eigenvectors. Computed radiances are only used for prelaunch coefficients. The deviations of the radiance scaled by noise from their sample mean are stored in the matrix $\Delta\tilde{T}_{Bn(m),j}$ (i.e., Eq. (2.61)), a matrix of dimensions $M \times J$, where M is the total number of instrument channels, m , and J is the sample size of the training data set. We begin by normalizing the measured radiances, $R[n(m)]$, for a subset of channels $n(m)$, by the measured instrument noise, $\text{NER}[n(m)]$. The noise scaled radiance covariance matrix from which

the EOFs are derived is then generated as follows:

$$\Delta \tilde{T}_{B,n(m),j} \equiv \frac{R_{n(m),j}}{\text{NER}[n(m)]} - \frac{\langle R_{n(m),j} \rangle_j}{\text{NER}[n(m)]} \equiv \frac{R_{n(m),j}}{\text{NER}[n(m)]} - \langle \tilde{T}_B \rangle_{n(m)}. \quad (2.61)$$

The eigenvectors of the signal-to-noise covariance are computed for $\Delta \tilde{T}_{B,n(m),j}$. For the CrIS FSR v2.0, the eigenvector file was trained using one day CrIS block 2.0 SDR radiances of 15 January 2015.

$$T_{N,\text{cov}} \equiv \frac{1}{J} \sum_{j=1}^J \Delta \tilde{T}_{B,n(m),j} \Delta \tilde{T}_{B,j,n(m)}(\theta) = E_{n(m),k}^T \Lambda_{k,k'} E_{k',n(m)} \quad (2.62)$$

The diagonal elements of represent the variance of the respective channel noise scaled radiance while the off-diagonal elements represent the covariance between pairs of channels. An eigenvector decomposition is performed on the matrix.

The eigenvectors of the normalized signal-to-noise covariance are orthogonal and $\Lambda_{k,k'}$ is a diagonal matrix with elements equal to λ_k . We normalize $\Delta T_B \Delta T_B^T$ by the number of observations J so that the magnitude of the eigenvalues does not change with the size of the training ensemble.

NOAA Eigenvector File Format

The eigenvector file is written out with the following components

1. Header Block containing

- the number of channels in the subset ($M = 2211$) and sample size ($J = 77,790$)
- the eigenvectors, $K_{\text{store}} = 200$
- a flag if radiances are used
- a flag if the mean is subtracted
- the noise file filename

2. The average of $\tilde{\Theta}$ for the M channels

$$\langle \tilde{T}_B \rangle \equiv \frac{\langle R_{n(m),j} \rangle_j}{\text{NE} \Delta N_n(m)} \quad (2.63)$$

3. Each eigenvector, $E_{k,n(m)}$, is written out a single record for each value of $k = 1, K_{\text{store}}$

4. The value of $\lambda(k)$ for $k = 1, K_{\text{store}}$
5. The value of $\text{NE}\Delta\text{N}(n_m)$ for $m = 1, M$
6. The value of $f[n(m)]$ for $m = 1, M$
7. The value of $n(m)$ for $m = 1, M$

Post-Launch Regression Computation

The radiances can be represented by their principal component scores. We have two sets of regression coefficient files, for all sky regression, the principal components are calculated from measured CrIS radiances, and for cloud clear regression, they are calculated from cloud clear radiance (see details in next chapter). In this algorithm we normalize by the square root of the eigenvalue to normalize the principal component scores so that they are numerically significant. Otherwise, the first principal component would have values approximately 1000 times the signal as $P(K_{\text{max}})$.

$$P_{k,j} = \frac{1}{\sqrt{\lambda_k}} E_{k,n(m)} \Delta\tilde{T}_{B,n(m),j} \quad (2.64)$$

an estimate of the propagated error in the principal components for case j , $\delta\hat{P}_{k,j}$, can be given by the root-sum-square (RSS) of the linear combination and an estimate of the error in the radiance for case j , $\delta R_{n(m),j}$. This results in an error in the argument of $\delta\tilde{T}_{N,n(m),j} \equiv \delta R_{n(m),j}/\text{NE}\Delta\text{N}_{n(m)}$ and

$$\delta\hat{P}_{k,j} = \sqrt{\frac{1}{\lambda_k} \left(E_{k,n(m)} \delta\tilde{T}_{N,n(m),j} \right)^2} \quad (2.65)$$

Only $k = 1, K_{\text{max}}$ principal components are kept, where K_{max} is the number of significant eigenvalues. For IR plus MW retrieval, the predictors also include ATMS 17 channel brightness temperature and they are channels 5–15 and 17–22. But for IR only retrieval, we should exclude ATMS brightness temperature of these channels from the predictors. Currently, Focus Days from CrIS/ATMS observations for generating regression coefficients are, 15 April 2018, 15 July 2018, 15 October 2018, and 15 January 2019 for SNPP; and 15 July 2018, 15 October 2018, 15 January 2019, and 15 April 2019 for NOAA-20. Data are selected by screening out cases where the CrIS cloud cleared radiances may be affected by clouds and where there may be problems with the geophysical states used as “truth” using the following tests:

1. The brightness temperature of the CrIS observation in channel $\nu_0 = 2390 \text{ cm}^{-1}$ must be less than 2 K of a predicted brightness temperature, $\hat{T}_B(\nu_0)$, estimated from ATMS brightness temperatures, T_{Bn} , for ATMS channels $n = 5, 6$ and 7 , as follows

$$\hat{T}_B(\nu_0) = a_1 + a_2 T_{B5} + a_3 T_{B6} + a_4 T_{B7} + a_5 \cos(\theta_\odot) + a_6 [1 - \cos(\vartheta)], \quad (2.66)$$

where a_i , $i = 1, \dots, 6$, are the coefficients of the ATMS screening test used to predict CrIS channel at 2390 cm^{-1} (determined to be $+50.05$, $+0.4791$, $+0.5635$, -0.2332 , $+3.03$, -15.02 , respectively), θ_\odot is solar zenith angle and ϑ is the view angle.

2. The reconstruction score is less than 1.5.
3. The surface temperature T_s must be higher than 180.0 K.

The regression is trained using ensembles at similar view angles. Currently, there are four view angle regimes as defined in Table 2.1. A predictor array is constructed using the principal component scores for those cases, $j(v)$ with $\vartheta_1(v) < |\vartheta| \leq \vartheta_2(v)$, where ϑ is the instrument view angle. For CrIS this angle varies from $-48.3^\circ \leq \vartheta \leq 48.3^\circ$. The predictor argument for the sub-set of cases is assembled with the first K_{\max} elements being set equal to $P_{k,j}$. The element $i = K_{\max} + 1$ is set equal to one if $\vartheta < 0$ or zero if $\vartheta \geq 0$

$$P_{k,j(v)} = \begin{pmatrix} P_{1,j(v)} \\ P_{2,j(v)} \\ \vdots \\ P_{K_{\max},j(v)} \\ \frac{1}{2} \{1 - \text{sgn}[\vartheta(v)]\} \\ T_{B5}, \dots, T_{B15}, T_{B17}, \dots, T_{B22} \\ 1 - \cos[\vartheta(v)] \end{pmatrix}, \quad i = 1, K_{\max} + 2. \quad (2.67)$$

Another issue for the regression is that topography limits the available training ensemble for some altitude layers. For each case, j , there is a maximum number of vertical levels defined by the surface pressure (that is, some of the 100 layer grid is below the surface). If this lower level is given as L_{bot} then the number of cases in the training ensemble is a function of how many cases have surface pressure above that level, therefore, the number of cases, J , in the training ensemble is a function of both view angle and L_{bot} and will can write that index as $j(v, L_{bot})$ which is the subset of cases that satisfy the criteria in Table 2.1 and have valid geophysical parameters in

Table 2.1: View-Angle Regimes in Post-Launch Regression

v	$\vartheta_1(v)$	$\vartheta_2(v)$
1	53.130°	42.269°
2	42.269°	31.788°
3	31.788°	19.948°
4	19.948°	0.000°

the layer under consideration in X_i . See Table 2.2 for a translation from X_i to layer index L . The average predictor argument for this subset ensemble can be computed and subtracted from the training ensemble

$$\Delta P_{k,j(v,L_{bot})} = P_{k,j(v,L_{bot})} - \langle P_{k,j(v,L_{bot})} \rangle_{j(v,L_{bot})} \quad (2.68)$$

The equation to be solved is given by

$$X_{i,j(v,L_{bot})} = \langle X_{i,j(v,L_{bot})} \rangle_{j(v,L_{bot})} + A_{i,k}^v \Delta P_{k,j(v,L_{bot})} \quad (2.69)$$

where we can write,

$$\Delta X_{i,j(v,L_{bot})} = X_{i,j(v,L_{bot})} - \langle X_{i,j(v,L_{bot})} \rangle_{j(v,L_{bot})} \quad (2.70)$$

The geophysical parameters in the NOAA regression are defined in Table 2.2. For moisture the regression is trained on both the $\ln[r(L)]$ and $r(L)$, where r is the mass mixing ratio in grams/kilo-gram (g/kg).

$$q = \frac{M_w \Delta C_w(L)}{M_t \Delta C_t(L)} = \frac{M_w \Delta C_w(L)}{1000 \cdot \frac{M_t}{M_d} N_A \frac{\Delta p(L)}{g}} \quad (2.71)$$

If it is assumed that $M_t \simeq 0.98 M_d + 0.02 M_w \approx 1$ and $g = 980.64 \approx 1000$, the form used in the code (mx2mr.F) is obtained, which is

$$q(L) = \frac{M_w \Delta C_w(L)}{N_A \Delta p(L)} \quad (2.72)$$

and the mass mixing ratio is then given by

$$r_w(L) = \frac{q(L)}{1 - q(L)} \quad (2.73)$$

Table 2.2: Geophysical parameters, X_i , solved for in NUCAPS regression

i	L	interpretation
1	1	$T(1)$
2	1	$r_w(1)$
3	1	$\ln[r_w(1)]$
4	1	$\ln[r_o(1)]$
5	2	$T(2)$
6	2	$r_w(2)$
7	2	$\ln[r_w(2)]$
8	2	$\ln[r_o(2)]$
\vdots	\vdots	\vdots
385	97	$T(97)$
386	97	$r_w(97)$
387	97	$\ln[r_w(97)]$
388	97	$\ln[r_o(97)]$
393	99	$T(P_s)$
394	99	$r_w(P_s)$
395	99	$\ln[r_w(P_s)]$
396	99	$\ln[r_o(P_s)]$
397	100	T_s

$r_w \equiv$ mass mixing ratio of water, $r_o \equiv$ mass mixing ratio of ozone. The index i is used in the data file and the index $L = 1 + (i - 1)/4$ is used in a storage vector in the retrieval code.

and the least square solution is given by

$$A_{i,k}^v = \Delta X_{i,j(v,L_{bot})} \Delta P_{j(v,L_{bot}),k}^T \left[\Delta P_{k,j(v,L_{bot})} \Delta P_{j(v,L_{bot}),k}^T \right]^{-1} \quad (2.74)$$

No regularization is needed since the principal components have been essentially regularized by selecting only 85 of the principal components. Note that the regression coefficients can be related to empirical Kernel functions, $\tilde{K}_n(L)$, for channel n and pressure level L .

In the eigenvector regression the empirical Kernel functions can be computed by

$$\tilde{K}_n(L) = A_{i(L),k} E_{k,n}, \quad (2.75)$$

where $i(L)$ is the subset of indices for the selection of the geophysical parameter

group (e.g., $T(L)$, is given for $L = 1, 2, 3, \dots$, which is given by $i = 1, 5, 9, \dots$ in Table 2.2)

Once $A_{i,k}^v$ is determined we can combine the average of the geophysical parameter given in Eq. (2.70), $\overline{X}_j \equiv \langle X_{i,j(v,L_{bot})} \rangle_{j(v,L_{bot})}$, and the average of the predictor given in Eq. (2.68), $\overline{P}_k \equiv \langle P_{k,j(v,L_{bot})} \rangle_{J(v,L_{bot})}$ into a single value, called $\overline{A}_i = \overline{X}_i + A_{i,k} \overline{P}_k$, so that our regression equation can utilize the un-normalized predictors

$$X_{i,j(v,L_{bot})} = \overline{A}_i + A_{i,k}^v P_{k,j(v,L_{bot})} \quad (2.76)$$

where \overline{A}_i^v is defined as

$$\overline{A}_i^v \equiv \langle X_{i,j(v,L_{bot})} \rangle_{j(v,L_{bot})} - A_{i,k}^v \langle P_{k,j(v,L_{bot})} \rangle_{J(v,L_{bot})} \quad (2.77)$$

A propagated error estimate can be computed from the linear combination of principal components

$$\delta \hat{X}_{i,j(v,L_{bot})} = \sqrt{\sum_i (A_{i,k}^v \delta P_{k,j(v,L_{bot})})^2} \quad (2.78)$$

Once the regression matrix is known it is useful to compute the mean and standard deviation of the real error between the regression, applied to the training ensemble radiances, and the geophysical value in the training ensemble. Each case has an error, δX , given by

$$\delta X_{i,j(v,L_{bot})} = X_{i,j(v,L_{bot})} - [\overline{A}_i + A_{i,k}^v \cdot P_{k,j(v,L_{bot})}] \quad (2.79)$$

For each geophysical parameter we can compute a mean and standard deviation of the regression error (difference of regression from the training values). The mean is given by

$$\overline{\delta X}_i \equiv \frac{1}{J(v, L_{bot})} \sum_j \delta X_{i,j(v,L_{bot})} \quad (2.80)$$

and a standard deviation is given by

$$\sigma(\delta X_i) \equiv \sqrt{\frac{1}{J(v, L_{bot})} \sum_j (\delta X_{i,j(v,L_{bot})} - \overline{\delta X}_i)^2} \quad (2.81)$$

The standard deviation can be compared to the standard deviation of the training ensemble's departure from its mean, given in Eq. (2.70)

$$\sigma(X_i) \equiv \sqrt{\frac{1}{J(v, L_{bot})} \sum_j (\Delta X_{i,j(v,L_{bot})})^2} \quad (2.82)$$

NOAA Regression File Format

In the NOAA regression file each set of geophysical parameters is written for a view angle block. The index number system for the geophysical parameters is given in Table 2.2. In the profile regression, the 393 parameters (1–388, 393–397) are written out in 4 sequential blocks in the regression file. In the surface regression the 39 emissivity regressions are written out first for land and then for ocean.

- A header line for each parameter block contains
 - parameter number (see Table 2.2)
 - number of predictors
 - pressure at level L or frequency at emissivity L
 - number of cases in training ensemble, $J(v, L_{bot})$ or $J(l)$.
 - the mean of the training ensemble, $\langle X_{j(v, L_{bot}(L))} \rangle_{j(v, L_{bot})}$
 - the standard deviation of the training ensemble, $\sigma[X(L)]$
 - the standard deviation of the error in the training ensemble, $\sigma[\delta X(L)]$
- A block of $I + 1$ coefficients, starting with \overline{A}_i^v and then the I values of $A_i(L)$.

Post-Launch Surface Emissivity Regression

In the case of surface emissivity there is no truth file to train against with real radiance data. In this case, we simulated J cases where the infrared radiances were computed from the ECMWF forecast and a surface emissivity model (Fishbein *et al.*, 2003). The eigenvector approach was not used. In this case, radiances for window channels, $R[n(m), j]$, are selected. The emissivities, $\epsilon(L, j)$, were provided by a model at the 39 frequencies. Notice that short-wave observations are not used to predict shortwave emissivity. This regression relies on statistical correlations between the short-wave and long-wave to solve for these parameters.

In this case, the predictors consisted of the M radiances, written as signal-to-noise (see Eq. (2.61)), and the side of the scan and cosine of the view angle were used as additional predictors. In this case, all J cases see the surface, so there is no subset for topography. Also, window channels require only a minor adjustment for view angle, so the complete ensemble was used. The ocean emissivity is a well modeled function (e.g., Masuda *et al.*, 1988; Masuda, 2006; Nalli *et al.*, 2008b,a) and

the regression is performed on land and ocean separately; land or ocean is indicated by the superscript l . Therefore, the predictors are given by

$$P_{k,j}^l = \begin{pmatrix} R_{1,j(l)} \\ R_{2,j(l)} \\ \vdots \\ R_{M,j(l)} \\ \frac{1}{2} \{1 - \text{sgn}[\vartheta(v_{j(l)})]\} \\ 1 - \cos[\vartheta(v_{j(l)})] \end{pmatrix}, \quad i = 1, M + 2 \quad (2.83)$$

where

$$\Delta X_{i,j(l)} = X_{i,j(l)} - \langle X_{j(l)} \rangle_{j(l)} \quad (2.84)$$

with the least square solution is given by

$$A_{i,k}^l = \Delta X_{i,j(l)} \Delta P_{j(l),k}^T [\Delta P_{k,j(l)} \Delta P_{j(l),k}^T]^{-1}. \quad (2.85)$$

Again, once $A_{i,k}^l$ is determined we can combine the average of the geophysical emissivity parameter and the average of the predictor into a single value, called \bar{A}_i , so that our regression equation becomes

$$X_{j(v,L_{bot}(L))} = \bar{A}_i^l + A_{i,k}^l P_{k,j(v,L_{bot})} \quad (2.86)$$

where \bar{A}_i^l is defined as

$$\bar{A}_i^l \equiv A_{i,k}^l \langle P_{k,j(v,L_{bot})} \rangle_{J(v,L_{bot})} \quad (2.87)$$

These regression coefficients have the same format as the ones described in Section 2.5.1.

2.6. Cloud-Clearing

Cloud-clearing is the process of computing the clear column radiance for a given channel n , and represents what the channel would have observed if the entire scene were cloud free. The entire scene is defined as the ATMS field of regard (FOR) which includes an array of 3×3 CrIS fields of views (FOV).

The cloud clearing approach is based upon the following reasoning. For simplicity of argument, we momentarily consider using only $K = 2$ adjacent FOVs and one cloud formation. The observed radiances in FOV $j = 1$ and 2, corresponding to channel n are given by:

$$R_1(n, \phi_0) = (1 - \alpha_1(\phi_0)) R_{\text{chr}}(n, \phi_0) + \alpha_1(\phi_0) R_{\text{clid}}(n, \phi_0), \quad (2.88)$$

$$R_2(n, \phi_0) = (1 - \alpha_2(\phi_0)) R_{\text{chr}}(n, \phi_0) + \alpha_2(\phi_0) R_{\text{clid}}(n, \phi_0), \quad (2.89)$$

where $\alpha_1(\phi_0)$ and $\alpha_2(\phi_0)$ are the zenith angle dependent effective cloud fractions for each field of view, $R_{\text{chr}}(n, \phi_0)$ is the radiance which would be observed if the entire field of view were clear, and $R_{\text{clid}}(n, \phi_0)$ is the radiance which would be observed if the entire field of view were covered by the cloud. The basic assumption of cloud-clearing is that if the observed radiances in each field-of-view are different, the differences in the observed radiances are solely attributed to the differences in the fractional cloudiness in each field of view while everything else (surface properties and atmospheric state) is uniform across the field of regard. A process referred to as *local angle adjustment* is applied to these observed radiances, channel by channel, to generate angle adjusted radiances, $R_j(n, \phi_0)$, representative of the radiance that CrIS channel n would have observed in FOV j if the observation were taken at the satellite zenith angle of the center FOV, ϕ_0 rather than at its actual satellite zenith angle. Based on this assumption, both $R_{\text{chr}}(n, \phi_0)$ and $R_{\text{clid}}(n, \phi_0)$ are assumed to have the same respective values in each field of view. For simplicity, from now on we will omit the central satellite zenith angle term, ϕ_0 .

Combining (2.88) and (2.89) and eliminating $R_{\text{clid}}(n)$ one can solve for the cloud-cleared radiance term as a linear extrapolation of the radiances from the two cloudy fields of view as follows:

$$R_{\text{chr}}(n) = R_1(n) + \frac{\alpha_1}{\alpha_2 - \alpha_1} [R_1(n) - R_2(n)]. \quad (2.90)$$

This is done in two steps. We first use an estimate of the cloud clear radiance, $\widehat{R}_{\text{chr}}(n)$, to obtain the so called cloud-clearing parameter η , defined as:

$$\eta = \frac{\alpha_1}{\alpha_2 - \alpha_1} = \frac{\widehat{R}_{\text{chr}}(n) - R_1(n)}{R_1(n) - R_2(n)} \quad (2.91)$$

The cloud-clearing term η is channel independent and is used then in (2.90) to solve for $R_{\text{clr}}(n)$ and cloud clear the entire spectrum.

While it is true that a single channel and 2 fields of view can be used to cloud clear the full spectrum in the presence of one cloud, for the case of K clouds a total of $K + 1$ fields of view and many channels must be used in a least squares sense to discriminate the clouds at different levels. Using the uniform scene assumption described above, Chahine (1977) showed that the reconstructed field of regard clear-column radiance for channel n , $R_{\text{CCR}}(n)$, can be written as a linear combination of the measured radiances in $K + 1$ fields of view, according to:

$$R_{\text{clr}}(n) = R_1(n) + \eta_1 [R_1(n) - R_{K+1}(n)] + \dots + \eta_l [R_1(n) - R_{(K+2)-l}(n)] + \eta_K [R_1(n) - R_2(n)], \quad (2.92)$$

where η_K are unknown channel independent constants and $K + 1$ fields of view are needed to solve for K cloud formations.

Equation (2.92) was later replaced by a similar but more stable equation of the form:

$$R_{\text{clr}}(n) \equiv \bar{R}_n + \sum_{j=1}^K (\bar{R}_n - R_{n,j}) \eta_j \quad (2.93)$$

where \bar{R}_n is called the extrapolation point and is an average of K FOV's defined by

$$\bar{R}_n \equiv \frac{1}{K} \sum_{j=1}^K R_{n,j}, \quad (2.94)$$

where \bar{R}_n is the average radiance of all K fields of view. The expression in (2.93), $\bar{R}_n - R_{n,j}$ is defined as *radiance contrast*.

As in Susskind et al. (1998), the η_j values are determined from observations in a selected set of N_c cloud filtering channels which are primarily selected in between lines of the 15 micron CO_2 band. If, for each channel n , one substitutes an estimated value, $\hat{R}_{\text{clr}}(n)$, of the expected cloud-clear radiance for channel n , $R_{\text{clr}}(n)$ in Eq. (2.93), this gives N_c equations for K unknowns, of which only $K - 1$ are linearly independent. Therefore, the solution for the $K \eta_j$ is given by a least square minimization whose parametrization is derived below. The radiance contrast can be rewritten in matrix form as:

$$S_{n,j} \equiv \bar{R}_n - R_{n,j}. \quad (2.95)$$

For nine FOVs the components of this matrix are given by:

$$S_{n,j} = \begin{pmatrix} \overline{R}_1 - R_{1,9} & \overline{R}_1 - R_{1,8} & \dots & \overline{R}_1 - R_{1,1} \\ \overline{R}_2 - R_{2,9} & \overline{R}_2 - R_{2,8} & \dots & \overline{R}_2 - R_{2,1} \\ \vdots & \vdots & \ddots & \vdots \\ \overline{R}_N - R_{N,9} & \overline{R}_N - R_{N,8} & \dots & \overline{R}_N - R_{N,1} \end{pmatrix}. \quad (2.96)$$

The equation to be solved can be written as:

$$\widehat{R}(n) - \overline{R}_n = S_{n,j} \eta_j. \quad (2.97)$$

The estimate of the clear radiances can be derived from

1. IR radiances computed from an estimate of the clear atmosphere from a MW physical retrieval, $R_n(X_L^{s,i-1})$,
2. IR radiances computed from an estimate of the clear atmosphere from a IR+MW physical retrieval which agrees with the MW radiances,
3. IR radiances computed from regression with MW radiances.

We apply a weight to the channels used in the least squares fit of this equation, $W_{n,n'}$, which is the inverse of an estimate of the covariance of $\widehat{R}(n) - \overline{R}_n$. The error covariance is given by computational error estimates associated with $\widehat{R}(n)$ derived from error estimates in the geophysical parameters, $C_{n,n'}$ and instrumental noise, $I_{n,n'}$, associated with \overline{R}_n .

$$W_{n,n'} = \left(\frac{I_{n,n'}}{N_A} + C_{n,n'} \right)^{-1} \quad (2.98)$$

The computational covariance matrix, $C_{n,n'}$, is composed of a summation of all the radiance error estimates, $E_{n,g}^{s,i}$, for all geophysical parameters held constant during a retrieval:

$$C_{n,n'} \equiv \sum_g E_{n,g}^{s,i} (E_{g,n}^T)^{s,i}. \quad (2.99)$$

The radiance error estimate, $E_{n,g}^{s,i}$, due to uncertainties in geophysical quantities is computed from error estimates in geophysical groups $X_{L,g}^{s,i}$ (*e.g.*, an entire temperature profile). As with the sensitivity functions, this can be thought of as an error estimate of a parameter, δA_g , and an associated function, $F_g^s(L)$. The partial derivatives are calculated from the current estimate of the geophysical state, $X_L^{s,i}$, and an estimate of the uncertainty in each geophysical group to be held constant in this stage

of the retrieval, $\delta X_{L,g}^{s,i}$, and is calculated by a finite difference for infrared channels (with additive functions)

$$E_{n,g}^{s,i} \equiv \delta A_j^{s,i} \cdot \left. \frac{\partial R_n (X_L^{s,i} + F_j \otimes \hat{A}_j)}{\partial A_j} \right|_{X_L^{s,i}} \quad (2.100)$$

$$\approx [R_n (X_L^{s,i} + \delta X_{L,g}^{s,i} \otimes Q_g) - R_n (X_L^{s,i})] , \quad (2.101)$$

and for microwave channels

$$E_{n,g}^{s,i} \approx T_{Bn} (X_L^{s,i} + \delta X_{L,g}^{s,i} \otimes Q_g) - T_{Bn} (X_L^{s,i}) . \quad (2.102)$$

Since $\delta X_{L,g}$ is an RSS error estimate it can be correlated vertically and spectrally and correlated with respect to other parameters (e.g., surface spectral emissivity error can be correlated with skin temperature). We use Q_g as a scaling to compensate for assumed anti-correlation in these error estimated. Currently we set Q_g to 0.5 for $T(p)$ and $q(p)$ error estimates and 1.0 for all other error estimates.

The instrument noise correlation matrix, $I_{n,n'}$, is given by

$$I_{n,n'} = \text{NER}_n \delta_{n,n'} \text{NER}_{n'} , \quad (2.103)$$

where the Kronecker delta function, $\delta_{n,n'}$

$$\begin{aligned} \delta_{n,n'} &= 1 , & n &= n' \\ &= 0 , & n &\neq n' . \end{aligned} \quad (2.104)$$

For an apodized interferometer the correlation matrix and noise reduction factor for the apodization function would replace the Kronecker delta function (e.g., Barnett et al., 2000).

The iterative methodology to determine clear-column radiances consists of four passes to determine η_s , $s = 1, 2, 3, 4$, using four sets of conditions, described later, to compute $R_{\text{clr}}(n)$. At each iteration, both $R_{\text{clr}}(n)$ and η_s become increasingly more accurate. Each set of conditions has its own covariance matrix, reflecting expected errors in $R_{\text{clr}}(n)$ and $R_j(n)$. The diagonal term of the noise covariance matrix is mod-

eled according to:

$$\begin{aligned}
(W_{n,n}^s)^{-1} = & (I_{n,n})^2 + \left[\frac{\partial R_n}{\partial T_s} \delta T_s^s \right]^2 + \left[\frac{\partial R_n}{\partial \epsilon_n} \delta \epsilon_n^s \right]^2 \\
& + \left[\frac{\partial R_n}{\partial \rho_n} \delta \rho_n^s \right]^2 + \left[\frac{\partial R_n}{\partial T(p)} \delta T(p)^s \right]^2 \\
& + \left[\left(\frac{\partial R_n}{\partial q(p)/q} \right) \left(\frac{\delta q(p)^s}{q} \right) \right]^2 + 0.1^2 \left(\frac{dB}{dT} \right)_{T_{B,n,clr}}^2 \\
& + N_{n,n}'^2 \left(\frac{dB}{dT} \right)_{T_{B,n,clr}}^2, \tag{2.105}
\end{aligned}$$

where $I_{n,n'}$ is the channel i instrumental noise and the next 5 terms are contributions to errors in the computed value $R_{clr}(n)$ resulting from errors in estimated surface skin temperature, surface spectral emissivity, surface spectral bi-directional reflectance of solar radiation, and temperature and moisture profile respectively. Two additional sources of radiance uncertainty are included in the equation, representative of the physics error estimate, $N_{n,n}'$ (see ahead), and an additional radiance uncertainty term. Both terms are in brightness temperature units. The off-diagonal term of the noise covariance matrix is given by:

$$(W_{n,n'})^{-1} = \left[\frac{\partial R_n}{\partial T_{sfc}} \frac{\partial R_{n'}}{\partial T_{sfc}} \delta T_{sfc}^s \right]^2 + \left[\frac{\partial R_n}{\partial \epsilon_n} \frac{\partial R_{n'}}{\partial \epsilon_{n'}} \delta \epsilon_n \delta \epsilon_{n'} \right] + \dots$$

Multiplying both sides of Eq. (2.97) with Eq. (2.98) yields

$$W_{n,n}^s [\hat{R}(n) - \bar{R}_n] = W_{n,n}^s S_{n,j} \eta_j^s, \tag{2.106}$$

then multiplying both sides by the transpose of the S -matrix yields

$$(S_{j,n})^T W_{n,n}^s [\hat{R}(n) - \bar{R}_n] = (S_{j,n})^T W_{n,n}^s S_{n,j} \eta_j^s, \tag{2.107}$$

and the least squares determination of the extrapolation parameters would be

$$\eta_j^s = [(S_{j,n})^T W_{n,n}^s S_{n,j}]^{-1} (S_{j,n})^T W_{n,n}^s [\hat{R}(n) - \bar{R}_n] \tag{2.108}$$

In low signal-to-noise or clear scenes the signal-to-noise matrix, $[(S_{j,n})^T W_{n,n}^s S_{n,j}]$, can vanish and the solution would become unstable. In addition, we would like to determine the error covariance of the cloud clearing parameters, $\delta \eta' \delta \eta$, which, we will discover, is equal to the inverse of the signal-to-noise matrix. The error covariance is highly non-diagonal which makes both damping and noise determination difficult.

Selection of Optimal Fields of View

The effects of instrumental noise on the clear column radiances will generate in general be amplified from single spot noise because the clear column radiance are expressed as a linear combination of the observations in different fields of view. We can compute the amplification of the random noise that results from cloud-clearing using Eq. (2.90). Taking again the case of two FOVs, Eq. (2.90) is first rewritten as

$$R_{\text{clr}}(n) = R_1(n) (1 + \eta) - R_2(n) \eta \quad (2.109)$$

and note that the standard deviation of the error in $R_1(n)$ and $R_2(n)$ are both given by $\text{NE}\Delta\text{N}$. The error in R_{clr} is given by

$$\delta R_{\text{clr}}^2(n) = \text{NER}^2 (1 + \eta)^2 + \text{NER}^2 \eta^2 \quad (2.110)$$

$$= \text{NER}^2 [(1 + \eta)^2 + \eta^2], \quad (2.111)$$

therefore, the error has been “amplified” by

$$A = \sqrt{(1 + \eta)^2 + \eta^2}. \quad (2.112)$$

Analogously, for the case of $n = 9$ field of view, we have:

$$A \equiv \sqrt{\sum_{j=1}^n \left[\frac{1}{n} \left(1 + \sum_{j'=1}^n \eta_{j'} \right) - \eta_j \right]^2}. \quad (2.113)$$

A is approximately equal to $\sqrt{\sum_{j=1}^n \eta_j^2}$ because the first term, containing the factor $1/n$, is small. It is desirable to find an accurate expression for clear column radiance which minimizes the amplification factor. We can do this by expressing Equation (2.93) in terms of radiances in an optimal set of fields of view, given by linear combination of the original set.

The matrix to be inverted can be transformed to a vector of eigenvalues, λ_k , with a unitary transformation matrix, $U_{j,k}$. The index j denotes the parameters in transformed space versus k for the untransformed parameters. This is equivalent to transforming the original $S_{n,j}$ matrix to an optimum linear combination of the original radiance differences, $S_{n,j} U_{j,k}$.

$$\Lambda_{k,k} \equiv (U_{k,j})^T (S_{j,n})^T W_{n,n}^s S_{n,j} U_{j,k}, \quad (2.114)$$

where λ_k are the diagonal elements of $\Lambda_{k,k}$. Eigenvalues where $\lambda_k < \lambda_c$, where λ_c is determined empirically, are not used in the solution. Removing low eigenvalues has

the effect of reducing noise in the solution. The number of non-zero eigenvalues is an estimate of the number of cloud formations determined by the observed radiances and the signal-to-noise analysis. The linear combination associated with each eigenvalue represents is uncorrelated with the other eigenvalues. The total number of cloud formations, N_ζ can be computed from the total number of significant eigenfunctions, defined by

$$\begin{aligned}\phi_k^s &= 1, & \lambda_k &\geq \lambda_c \\ &= 0, & \lambda_k &< \lambda_c,\end{aligned}\tag{2.115}$$

$$N_\zeta = \sum_{k=1}^K \phi_k^s.\tag{2.116}$$

Equation (2.97) can then be written in transformed ζ space or un-transformed η space as follows

$$R(n)^{\text{CCR}} = \bar{R}_n + (S_{n,j} U_{j,k}) \zeta_k^s\tag{2.117}$$

$$= \bar{R}_n + S_{n,j} (U_{j,k} \zeta_k^s) = \bar{R}_n + S_{n,j} \tilde{\eta}_j^s.\tag{2.118}$$

Multiplying both sides of Eq. (2.117) with Eq. (2.98) yields

$$W_{n,n}^s [\hat{R}(n) - \bar{R}_n] = W_{n,n}^s (S_{n,j} U_{j,k}) \zeta_k^s,\tag{2.119}$$

then multiplying both sides by the transpose of the transformed S -matrix yields

$$(U_{k,j})^T (S_{j,n})^T W_{n,n}^s [\hat{R}(n) - \bar{R}_n] = (U_{k,j})^T (S_{j,n})^T W_{n,n}^s U_{j,k} S_{n,j} \zeta_k^s,\tag{2.120}$$

and the least squares determination of the extrapolation parameters would be

$$\zeta_k^s = \left[(U_{k,j})^T (S_{j,n})^T W_{n,n}^s S_{n,j} U_{j,k} \right]^{-1} (U_{k,j})^T (S_{j,n})^T W_{n,n}^s [\hat{R}(n) - \bar{R}_n],\tag{2.121}$$

however, the inverse can be replaced with Eq. (2.114)

$$\zeta_k^s = (\Lambda_{k,k})^{-1} (U_{k,j})^T (S_{j,n})^T W_{n,n}^s [\hat{R}(n) - \bar{R}_n]\tag{2.122}$$

$$= \left(\frac{1}{\lambda_k} \right) (U_{k,j})^T (S_{j,n})^T W_{n,n}^s [\hat{R}(n) - \bar{R}_n].\tag{2.123}$$

Equation (2.122) is exactly equal to the transform of Eq. (2.108)

$$\eta_j^s = U_{j,k} \zeta_k^s,\tag{2.124}$$

however, we can now remove the ζ associated with low eigenvectors

$$\tilde{\zeta}_k^s = \frac{\phi_k^s}{\lambda_k} (U_{k,j})^T (S_{j,n})^T W_{n,n}^s [\hat{R}(n) - \bar{R}_n], \quad (2.125)$$

$$\tilde{\eta}_j^s \equiv U_{j,k} \tilde{\zeta}_k^s = U_{j,k} \frac{\phi_k^s}{\lambda_k} (U_{k,j})^T (S_{j,n})^T W_{n,n}^s [\hat{R}(n) - \bar{R}_n], \quad (2.126)$$

where $\tilde{\eta}_j^s$ is the extrapolation parameters from the damped least squares solution.

Discarding low eigenvalues reduces the noise amplification factor by suppressing noise in the solution for η , resulting in lower values of η . The values of η_j^s are used in Eq. (2.93) to determine the cloud-cleared radiance.

Definition of Cloud Clearing Symbols Used in Section 2.6

symbol	description
X^s	superscript s refers to the step
i	FOV index
j	η index
J	number of η_j
k	ζ index
n	channel index
N_F	the number of FOV's within an AMSU footprint
N_A	the number of FOV's within \overline{R}_n
$\delta_{n,n'}$	Kronecker delta function
η_j	extrapolation parameters, determined w/o damping
$\tilde{\eta}_j$	extrapolation parameters, determined w/ damping
$\delta\tilde{\eta}_j$	error in η with damping
A_n^s	noise amplification factor
$R_{n,j}$	observed radiance in FOV j
X_L^s	geophysical state ($T(p), q(p), O_3(p), \epsilon(n), \dots$)
$R_n(X_L^{s,i-1})$	Radiance Computed from a geophysical state
$R(n)^{CCR}$	clear column radiance
$\hat{R}(n)$	clear radiance estimate
\overline{R}_n	average of observed cloudy FOV's
$I_{n,n'}$	instrument noise covariance
NER	standard deviation of instrumental noise
$N_{n,n'}$	error covariance of $(\hat{R}(n) - \overline{R}_n)$
$W_{n,n'}$	inverse of error covariance of $(\hat{R}(n) - \overline{R}_n)$
$S_{n,j}$	FOV contrast, $\overline{R}_n - R_{n,j}$
$U_{j,k}$	eigenvectors of $[(S_{j,n})^T W_{n,n'}^s S_{n,j}]$
$\Lambda_{k,k}$	eigenvalue matrix of $[(S_{j,n})^T W_{n,n'}^s S_{n,j}]$
λ_k	diagonal elements of $\Lambda_{k,k}$
ζ_k^s	transformed extrapolation parameters
$\left(\delta\tilde{\zeta}_k \delta\tilde{\zeta}_k^T \right)^s$	error covariance of solved components of ζ
$\left(\delta\hat{\zeta}_k \delta\hat{\zeta}_k^T \right)^s$	error covariance of components of ζ not solved for
$\left(\delta\zeta_k \cdot \delta\zeta_k^T \right)^s$	total error covariance of ζ

2.7. Physical Retrieval Algorithm

2.7.1. The Inverse Problem

The retrieval of geophysical quantities, such as the atmospheric water, from satellite radiances is highly non-linear, requiring inversion of the equations of the form

$$R_n(\nu, X) \approx \int_{\nu} \Phi_{\nu} \int_p B[T(p)] \frac{\partial}{\partial p} \{ \exp[-\tau_i(\nu)] \} dp d\nu, \quad (2.127)$$

where $\tau_i(\nu)$ is the optical depth for species i and channel ν defined as

$$\tau_i(\nu) \equiv \int_{\infty}^{z(p)} \sum_i \kappa_i(\nu, X, \dots) dz'. \quad (2.128)$$

It should be kept in mind that Eq. (2.127) is an approximation and that the real radiative transfer equation (RTE) has non-linear components resulting from

1. The temperature dependence of the transmittance,
2. The non-linearity of the Planck function,
3. The downwelling component of the radiative transfer equation.

Brightness temperature, T_{Bn} , is usually more linear with temperature (a NUCAPS core product EDR), provides improved numerical stability, and is a convenient way to display multi-spectral radiance information

$$T_{Bn} \equiv B_{\nu_0}^{-1}(R_n) = \frac{\alpha_2 \nu_0}{\ln \left[1 + \frac{\alpha_1 \nu_0^3}{R_n} \right]}. \quad (2.129)$$

Usually, only radiance differences (i.e., observations minus calculations, abbreviated “obs – calc” or “O – C”), are needed in remote sounding so that a radiance difference, ΔR_n , can be converted to a brightness temperature difference, ΔT_{Bn} , as follows

$$\Delta T_{Bn} \simeq \Delta R_n \left[\frac{\partial B_{\nu}}{\partial T} \right]_{B_{\nu}^{-1}[R_n(X_L^{s,i-1})]}^{-1}. \quad (2.130)$$

2.7.2. Linearization of the RTE

The first step to retrieving the atmospheric state is the linearization of the RTE. This can be achieved via a Taylor expansion integrand about a reference or background state, X_0 .

For a temperature retrieval this is accomplished by first linearizing the Planck function a the reference temperature profile as follows:

$$T(z) \equiv T_0(z) + \Delta T(z), \quad (2.131)$$

so that

$$B_\nu[T(z)] = B_\nu[T_0(z)] + \left. \frac{\partial B_\nu[T_0(z)]}{\partial T} \right|_{T_0(z)} \Delta T(z). \quad (2.132)$$

In general, the radiance of the reference state, X_0 , can be computed. In our example, we will consider only the atmospheric component of the RTE:

$$R_{\nu_0} = \int_0^\infty B_\nu[T_0(z)] \frac{\partial \tau_\nu(X_0)}{\partial z} dz. \quad (2.133)$$

Everything is known within this equation except the temperature profile correction, $\Delta T(z)$. Inserting Eq. (2.132) into (2.133) leaves

$$\Delta R_\nu = R_\nu - R_{\nu_0} = \int_0^\infty \left\{ B_\nu[T_0(z)] + \left. \frac{\partial B_\nu[T_0(z)]}{\partial T} \right|_{T_0(z)} \Delta T(z) \right\} \frac{\partial \tau_\nu}{\partial z} dz - R_{\nu_0}, \quad (2.134)$$

which can be simplified

$$\Delta R_\nu = \int_0^\infty \left. \frac{\partial B_\nu[T_0(z)]}{\partial T} \right|_{T_0(z)} \frac{\partial \tau_\nu}{\partial z} \Delta T(z) dz, \quad (2.135)$$

Then defining the *kernel function* as

$$K(z, \nu) \equiv \left. \frac{\partial B_\nu[T_0(z)]}{\partial T} \right|_{T_0(z)} \frac{\partial \tau_\nu}{\partial z}, \quad (2.136)$$

we arrive at a *linearized RTE*, written as

$$\Delta R_\nu = \int_0^\infty K(z, \nu) \Delta T(z) dz. \quad (2.137)$$

Thus, the frequency dependence of the Planck function and the temperature dependence of the transmittance are both ignored. Note that for unapodized interferometers and broad band instruments this expansion is not justified. For narrowband

channels (i.e., $\Delta\nu \geq O(10^1) \text{ cm}^{-1}$, e.g., MODIS, HIRS, etc.), an effective Planck function can be computed by integration over the band pass, $\Delta\nu$. For an un-apodized interferometer the side-lobes are significant for 100's of cm^{-1} . The linearization of the integrand is one of the principal reasons for use of apodized interferometer spectra.

Equation (2.137) can be approximated by a numerical integral which has the advantage of being solved by matrix inversion.

$$\Delta R_n \approx \sum_{L=1}^{N_L} [\Delta z(L) K(n, L)] \Delta T(L) = \tilde{K}_{n,L} \Delta T(L). \quad (2.138)$$

The thickness of the layer for the finite difference form is usually absorbed into the definition of K , written as \tilde{K} above.

As an example, For $N_\nu = 3$ and $N_z = 4$ the matrix would look like:

$$\begin{bmatrix} \Delta R(\nu_1) \\ \Delta R(\nu_2) \\ \Delta R(\nu_3) \end{bmatrix} = \Delta z \begin{bmatrix} K(z_1, \nu_1) & K(z_2, \nu_1) & K(z_3, \nu_1) & K(z_4, \nu_1) \\ K(z_1, \nu_2) & K(z_2, \nu_2) & K(z_3, \nu_2) & K(z_4, \nu_2) \\ K(z_1, \nu_3) & K(z_2, \nu_3) & K(z_3, \nu_3) & K(z_4, \nu_3) \end{bmatrix} \begin{bmatrix} \Delta T(z_1) \\ \Delta T(z_2) \\ \Delta T(z_3) \\ \Delta T(z_4) \end{bmatrix}, \quad (2.139)$$

which can be written in matrix form as (the Δz component is included in the matrix $K_{n,L}$):

$$\Delta R_n = K_{n,L} \Delta T_L. \quad (2.140)$$

If N_ν is greater than N_z then there are more equations than unknowns and an inverse for $K_{n,L}$ exists, $K_{L,n}^{-1}$, then the correction to the initial temperature profile can be found as follows:

$$K_{L,n}^{-1} \Delta R_n = K_{L,n}^{-1} K_{n,L} \Delta T_L = \Delta T_L, \quad (2.141)$$

$$\Delta T_L = K_{L,n}^{-1} \Delta R_n = [K_{L,n}^T K_{n,L}]^{-1} K_{L,n}^T \Delta R_n. \quad (2.142)$$

where we employ the definition of a an inverse of a non-square matrix to find the expression for K^{-1} as follows

$$\begin{aligned} K_{n,L} K_{L,n}^{-1} &= I_{n,n} \\ K_{L,n}^T (K_{n,L} K_{L,n}^{-1}) &= K_{L,n}^T I_{n,n} \\ (K_{L,n}^T K_{n,L}) K_{L,n}^{-1} &= K_{L,n}^T \\ K_{L,n}^{-1} &= (K_{L,n}^T K_{n,L})^{-1} K_{L,n}^T. \end{aligned} \quad (2.143)$$

Unfortunately, N_ν is usually much smaller than N_z . This is because the kernel functions tend to overlap and, therefore, are not independent. This is a condition

generally referred to as *information redundancy* which makes the inversion equation ill-posed. Least squares techniques need to be applied and the solution for ΔT can be found by iterative techniques. The above expression is generalized as follows. Using the notation of the generalized sensitivity matrix, $S_{n,L}$, in place of the traditional kernel function, $K_{n,L}$ the unconstrained expression to be solved has the form of

$$\Delta R_n = R_n - f(X_L) = S_{n,L} \Delta X_L. \quad (2.144)$$

The inverse solution is given by:

$$\Delta X_L = S_{L,n}^{-1} \Delta R_n. \quad (2.145)$$

Again, from the definition of an inverse

$$S_{n,L} S_{L,n}^{-1} = I_{n,n} \quad (2.146)$$

$$S_{L,n}^T (S_{n,L} S_{L,n}^{-1}) = S_{L,n}^T I_{n,n} \quad (2.147)$$

$$(S_{L,n}^T S_{n,L}) S_{L,n}^{-1} = S_{L,n}^T, \quad (2.148)$$

therefore, for a non-square matrix, $S_{n,L}$, the inverse is given by

$$S_{j,n}^{-1} = [S_{L,n}^T S_{n,L}]^{-1} S_{L,n}^T. \quad (2.149)$$

So that Eq. (2.145) becomes

$$\Delta X_L = [S_{L,n}^T S_{n,L}]^{-1} S_{L,n}^T \Delta R_n. \quad (2.150)$$

In addition to the redundancy problem, ΔR_n has a large fraction of noise (due to low signal-to-noise related to the low temperatures) which makes the solution unstable. Careful attention must be given to the select channels containing the maximum amount of unique information from the spectra and with the lowest instrumental noise. See ahead the section on the channel selection methodology. To take into account the noise problem, a weighted least squares solution can be computed

$$\Delta X_L = [S_{L,n}^T W_{n,n} S_{n,L}]^{-1} S_{L,n}^T W_{n,n} \Delta R_n. \quad (2.151)$$

Another critical problem is represented by the fact that the kernel functions $S_{n,L}$ are very broad functions and, therefore, are insensitive to high frequency oscillations in ΔX_L . As a result, the inversion process usually converges with unrealistic vertical profiles.

In the most crude sense, regularization is the stabilization of the inverse by adding something to the matrix to avoid an in-determinant solution (*i.e.*, a zero divided by

zero). This, in effect, will dampen the solution, ΔX_L , and make it “stick” to the previous iteration. This results in a need for a *background* term, Ψ_n , in order to iterate the solution

$$\Delta X_L = [S_{L,n}^T W_{n,n} S_{n,L} + H_{L,L}]^{-1} S_{L,n}^T W_{n,n} (\Delta R_n - \Phi_n) . \quad (2.152)$$

The atmospheric state, X_L^s , and the error estimate of that state, δX_L^s , are used to minimize the residuals in observed minus computed radiances in each retrieval step s .

2.7.3. IR+MW Physical Retrieval Module

The current NUCAPS retrieval system is a modular set of retrieval steps. Each retrieval step solves for certain parameters while holding all others constant. The geophysical state of the clear atmosphere, $X_L^{s,i}$, at a given retrieval step, s , and iteration, i , is given in Table 2.3.

Table 2.3: Definition of the Geophysical State, $X_L^{s,i}$, in the NUCAPS Algorithm

$T(p)$	vertical temperature profile
$q(p)$	vertical water vapor profile (7.7 g/kg @ surface)
$L(p)$	vertical liquid water profile
$O_3(p)$	vertical ozone profile (0.4 ppmv, 8ppmv @ 6 hPa)
T_s	surface temperature
$\epsilon(\nu)$	spectral surface emissivity
$\rho_{\odot}(\nu)$	spectral surface reflectivity of solar radiation
$CO_2(p)$	carbon dioxide profile
$CH_4(p)$	methane profile
$CO(p)$	carbon monoxide profile
$N_2O(p)$	nitrogen oxide profile
$SO_2(p)$	sulfur dioxide profile
HNO_3	nitric acid profile

Each step solves for specific geophysical parameters while holding others constant. The parameters considered as error sources in the error covariance matrix are shown in the table. Some parameters are not accurately known and, therefore, they are only considered on the diagonal of the error covariance matrix. These are shown with a dagger symbol, †.

Each step uses its own subset of channels. If the error covariance matrix is large for a given channel or it has large spectroscopic uncertainties then it is permanently removed from the computation. This has obvious improvements for execution time and it also improves results, since error estimates and damping are the least accurate components of the retrieval process.

The clear-column radiance is calculated from the N_F FOV's using the equation:

$$R(n)^{\text{CCR}} = \bar{R}_n + \sum_{j=1}^{N_F} (\bar{R}_n - R_{n,N_F+1-j}) \tilde{\eta}_j^{s,i} \quad (2.153)$$

It is possible for the cloud-cleared radiance observations to be close to zero or even negative due to instrumental noise and cloud clearing errors. Therefore, we never attempt to compute a clear column brightness temperature from these radiances.

The retrieval algorithm minimizes the weighted difference between the clear column radiance observations, $R(n)^{\text{CCR}}$, and radiances computed using a forward model, $R_n(X_N^{s,i})$, by varying the geophysical state, $X_L^{s,i}$, where i is the iteration number within the current retrieval step, s . The forward model at iteration $i = 1$ uses the previous iteration's retrieved geophysical state, $X_L^{s,i}$. For $s = 1, i = 1$, $X_L^{1,1}$ comes from a first guess (climatology) and for $s > 1, i = 1$ the retrieval uses the result from the last iteration, $I + 1$, from the previous step as a first guess, $X_L^{s,1} = X_L^{s-1,I+1}$.

For multi-spectral retrievals the radiances can vary many orders of magnitude over the spectral regions (e.g., microwave, long-wave infrared, and short-wave infrared). To maintain numerical precision it is desirable to normalize the obs – calc (or O – C). We would like to mimic a brightness temperature difference and we can approximate this by

For IR channels O – C is computed as

$$\Delta T_{B,n}^{s,i} \equiv [R(n)^{\text{CCR}} - R_n(X_N^{s,i})] \left[\frac{\partial B_\nu}{\partial T} \right]_{B_\nu^{-1}(R_n(X_N^{s,i}))}^{-1}, \quad (2.154)$$

while for MW channels, where the data is given in brightness temperature, a brightness temperature difference can be computed as

$$\Delta T_{B,n}^{s,i} \equiv [T_{B,n,\text{CCR}} - T_{B,n}(X_L^{s,i})], \quad (2.155)$$

where $T_{B,n,\text{CCR}}$ is either the observed microwave brightness temperatures or the average of the 9 brightness temperatures within the ATMS field-of-regard (FOR).

2.7.4. Specification of Geophysical Functions

A change to a group of the geophysical state are represented by a geophysical perturbation parameters, $\Delta A_j^{s,i}$, and an associated perturbation function, $F_{L,j}^s$. This is the generalized sensitivity matrix. For vertical profiles, such as $T(p)$, $q(p)$, $O_3(p)$, the perturbation function, $F_{L,j}^s = F_j^s(p)$, is a trapezoid (with dimensionless maximum value of 1.0) covering a vertical range of layers. For spectral parameters such as $\epsilon(n)$ and $\rho(n)$, $F_{L,j}^s = F_j^s(\nu)$ is a wedge or triangle covering a range of frequencies with a dimensionless peak value of 1.0. For surface temperature and microwave emissivity $F_{L,j}^s$ is a value equal to unity. These are summarized in the following table:.

Temperature functions are expressed as additive vertical trapezoids, the atmospheric profile being

$$T^{s,i+1}(p) = T^{s,i}(p) + \sum_j F_j^s(p) \Delta A_j^{s,i+1}, \quad (2.156)$$

and the surface skin temperature being

$$T_s^{s,i+1} = T_s^{s,i} + F_j^s \Delta A_j^{s,i+1}. \quad (2.157)$$

Composition functions are expressed as multiplicative vertical trapezoids. The radiance kernel is $\propto \exp[\kappa(X_L^{s,i})]$ and $\kappa(X_L^{s,i})$, is the optical depth $\propto X_L^{s,i}$. Therefore, composition variables are more linear in $\ln(X_L^{s,i})$, with $\partial \ln(X_L^{s,i}) \propto \partial X_L^{s,i} / X_L^{s,i}$ being a % change in $X_L^{s,i}$; thus

$$q^{s,i+1}(p) = q^{s,i}(p) \left[1 + \sum_j F_j^s(p) \Delta A_j^{s,i+1} \right]. \quad (2.158)$$

Emissivity functions are expressed as additive spectral triangles

$$\epsilon^{s,i+1}(n) = \epsilon^{s,i}(n) + \sum_j F_j^s(\nu) \Delta A_j^{s,i+1}. \quad (2.159)$$

The scaling parameter \hat{A}_j^s is used to create dimensionless parameters and adjust scale between different functional groups (e.g., when mixing $T(p)$, $q(p)$, and emissivity in one retrieval). The Jacobian, $K_{n,L}^{s,i}$ becomes a set of new derivatives, $S_{n,j}^{s,i}$, in which groups of parameters in L space are grouped together in J space. Subsets (e.g., temperature) of vertical and spectral functions must sum to unity: $\sum_j F_{L,j}^s = 1$ for a group of functions.

The entire geophysical state is expressed as a vector X_L , with associated geophysical perturbation functions $\Delta X_{L,j} = F_{L,j}^s \otimes \Delta \hat{A}_j^s$ and perturbation parameters $\Delta A_j^{s,i}$. The \otimes symbol represents a scale factor for $F_{L,j}^s$ and not a matrix multiply

and is equivalent to an identity matrix multiplication, $F_{L,j}^s \otimes \Delta \hat{A}_j^s \equiv F_{L,j}^s I_{j,j} \Delta \hat{A}_j^s$. For vertical functions the index L will specify pressure intervals while for spectral parameters the functions will represent frequency intervals and L will specify the channel numbers, n . For other functions, such as skin temperature the function is a value that is, the index L is single valued, and there is only one value of j

$$X_L^{s,i+1} = X_L^{s,i} + \sum_j \left(F_{L,j}^s \otimes \Delta \hat{A}_j^s \right) \Delta A_j^{s,i+1}. \quad (2.160)$$

The sensitivity matrix, $S_{n,j}^{s,i}$ is calculated for each channel n and each geophysical parameter, denoted by index j , to be solved for in the current retrieval step, s , and iteration, i . The sensitivity matrix is computed for a pre-set perturbation functions, $F_{L,j}^s \otimes \Delta \hat{A}_j^s$ as follows

For additive functions the S -matrix is given by

$$S_{n,j}^{s,i} \equiv \Delta \hat{A}_j^s \frac{\partial R_n (X + F_{L,j}^s A_j)}{\partial A_j} \Bigg|_{X_L^{s,i}} \left[\frac{\partial B_\nu}{\partial T} \right]_{B_\nu^{-1}[R_n(X_N^{s,i})]}^{-1} \quad (2.161)$$

$$\approx \left[R_n \left(X_L^{s,i} + F_{L,j}^s \Delta \hat{A}_j^s \right) - R_n \left(X_N^{s,i} \right) \right] \left[\frac{\partial B_\nu}{\partial T} \right]_{B_\nu^{-1}[R_n(X_N^{s,i})]}^{-1} \quad (2.162)$$

for IR channels, and for MW channels given by

$$S_{n,j}^{s,i} \simeq T_{Bn} \left(X_L^{s,i} + F_{L,j}^s \Delta \hat{A}_j^s \right) - T_{Bn} \left(X_L^{s,i} \right). \quad (2.163)$$

For multiplicative functions the S -matrix is given by

$$S_{n,j}^{s,i} \equiv \Delta \hat{A}_j^s \frac{\partial R_n [X (1 + F_{L,j}^s A_j)]}{\partial A_j} \Bigg|_{X_L^{s,i}} \left[\frac{\partial B_\nu}{\partial T} \right]_{B_\nu^{-1}[R_n(X_N^{s,i})]}^{-1} \quad (2.164)$$

$$\approx \left\{ R_n \left[X_L^{s,i} \left(1 + F_{L,j}^s \Delta \hat{A}_j^s \right) \right] - R_n \left(X_N^{s,i} \right) \right\} \left[\frac{\partial B_\nu}{\partial T} \right]_{B_\nu^{-1}[R_n(X_N^{s,i})]}^{-1}, \quad (2.165)$$

and for MW channels

$$S_{n,j}^{s,i} \approx T_{Bn} \left[X_L^{s,i} \left(1 + F_{L,j}^s \Delta \hat{A}_j^s \right) \right] - T_{Bn} \left(X_L^{s,i} \right). \quad (2.166)$$

Analytic derivatives on the RTM/RTA grid does not help the algorithm and δ -function perturbations are sub-optimal (Backus and Gilbert). Single-sided finite differences have been used, although the benefit of double-sided and dynamically scaled derivatives will be explored (this is not the algorithm's biggest error source).

2.7.5. Retrieval Error Covariance Matrix

The error covariance matrix, $N_{n,n'}^s$, is computed in the first iteration of every step and is the estimate of the uncertainty in the observed minus computed effective brightness temperature difference, $\Delta T_{Bn}^{s,i}$. It consists of the clear column radiance error estimate, discussed earlier and computational uncertainties in the forward calculation of $R_n(X_N^{s,i})$. The computational uncertainty is calculated for all geophysical parameters, X , not modified by the retrieval and, therefore, assumed known in a given step of the retrieval process.

The radiance error estimate, $E_{n,g}^{s,i}$, due to uncertainties in geophysical quantities is computed from error estimates in geophysical groups $X_{L,g}^{s,i}$ (e.g., an entire temperature profile). As with the sensitivity functions, this can be thought of as an error estimate of a parameter, δA_g , and an associated function, $F_g^s(L)$. The partial derivatives are calculated from the current estimate of the geophysical state, $X_L^{s,i}$, and an estimate of the uncertainty in each geophysical group to be held constant in this stage of the retrieval, $\delta X_{L,g}^{s,i}$, and is calculated by a finite difference

For IR channels the error estimate is converted to effective brightness temperature units using

$$E_{n,g}^{s,i} \equiv \delta A_j^{s,i} \frac{\partial R_n(X_L^{s,i})}{\partial A_j} \bigg|_{X_L^{s,i}} \left[\frac{\partial B_\nu}{\partial T} \right]_{B_\nu^{-1}[R_n(X_N^{s,i})]}^{-1} \quad (2.167)$$

$$\approx [R_n(X_L^{s,i} + \delta X_{L,g}^{s,i} \otimes Q_g) - R_n(X_L^{s,i})] \left[\frac{\partial B_\nu}{\partial T} \right]_{B_\nu^{-1}[R_n(X_N^{s,i})]}^{-1} \quad (2.168)$$

and for MW channels the computation is

$$E_{n,g}^{s,i} \approx T_{Bn}(X_L^{s,i} + \delta X_{L,g}^{s,i} \otimes Q_g) - T_{Bn}(X_L^{s,i}) . \quad (2.169)$$

Since $\delta X_{L,g}$ is an RSS error estimate it can be correlated vertically and spectrally and correlated with respect to other parameters (e.g., surface spectral emissivity error can be correlated with skin temperature). We use Q_g as a scaling to compensate for assumed anti-correlation in these error estimated. Currently we set Q_g to 0.5 for $T(p)$ and $q(p)$ error estimates and 1.0 for all other error estimates.

The computational covariance matrix, $C_{n,n'}^{s,i}$, is composed of a summation of all the radiance error estimate for all geophysical parameters held constant during a retrieval

$$C_{n,n'}^{s,i} \equiv \sum_g E_{n,g}^{s,i} (E_{g,n}^T)^{s,i} . \quad (2.170)$$

The retrieval error covariance matrix is a combination of the cloud cleared radiance error covariance and the computational error covariance terms

$$N_{n,n'}^{s,i} = C_{n,n'}^s + \frac{\left[\delta R(n)^{\text{CCR}} (\delta R_{n',\text{obs}})^T + \delta R_n^U \delta_{n,n'} (\delta R_{n'}^U)^T \right]}{\left[\frac{\partial B_\nu}{\partial T} \right]_{B_\nu^{-1}[R_n(X_N^{s,i})]} \cdot \left[\frac{\partial B_\nu}{\partial T} \right]_{B_\nu^{-1}[R_{n'}(X_L^{s,i})]}}, \quad (2.171)$$

where δR_n^U is a small term for additional unknown sources of error which is presently computed from

$$\delta R_n^U \equiv 0.1 \left[\frac{\partial B_\nu}{\partial T} \right]_{B_\nu^{-1}[R_n(X_N^{s,i})]}^{-1}. \quad (2.172)$$

In the retrieval code, the cloud-cleared radiance error estimates are computed in the routine `noisecv.F` and the computation terms are computed and added to the noise covariance matrix in the individual retrieval routines (e.g., `rettmpc.F`, `retwatr.F`, etc.)

2.7.6. The Retrieval of the Geophysical State

The brightness temperature difference residuals can be written in terms of a linear Taylor expansion change to the geophysical parameters, $\Delta A_j^{s,i}$, which is dimensionless due to $\Delta \hat{A}_j^s$ in Eqs. (2.161) or (2.164). In any given retrieval step, we separate the parameters we are solving for into the matrix $S_{n,j}^{s,i}$ and the parameters we are not solving for into the matrix $E_{n,g}^{s,i}$. If it is assumed for the moment that the value of the parameters not being solved for are known, such that $E_{n,g}^{s,i}$ could be known, the following could be written

$$\Delta T_{Bn}^{s,i} = S_{n,j}^{s,i} \Delta A_j^{s,i+1} + \sum_g \pm E_{n,g}^{s,i}. \quad (2.173)$$

But the sign of the errors are not known in the parameters not being solved for, otherwise that uncertainty could be eliminated. At best there is only an estimate for the covariance and spectral correlation of these uncertainties, therefore, $\sum_g \pm E_{n,g}^{s,i}$ enters into the error covariance matrix via Eqs. (2.170) and (2.171) so that the brightness temperature residuals, $\Delta T_{Bn}^{s,i}$, can be related to the parameters being solved for via

$$(N_{n,n}^s)^{-1} S_{n,j}^{s,i} \Delta A_j^{s,i+1} = (N_{n,n}^s)^{-1} \Delta T_{Bn}^{s,i} \quad (2.174)$$

$$(S_{j,n}^T)^{s,i} (N_{n,n}^s)^{-1} S_{n,j}^{s,i} \Delta A_j^{s,i+1} = (S_{j,n}^T)^{s,i} (N_{n,n}^s)^{-1} \Delta T_{Bn}^{s,i}. \quad (2.175)$$

The assumption that is implicit here is that properly weighted geophysical parameter errors, $(N_{n,n}^s)^{-1} \sum_g \pm E_{n,g}^{s,i}$, are uncorrelated with the parameters we are trying to solve for. That is, the properly weighted equation is one that has the smallest standard deviation.

The change required to the parameters can be solved in a weighted least-squares sense. If there were no damping then the solution would be given by

$$\Delta A_j^{s,i+1}(0) = \left[(S_{j,n}^T)^{s,i} (N_{n,n}^s)^{-1} S_{n,j}^{s,i} \right]^{-1} (S_{j,n}^T)^{s,i} (N_{n,n}^s)^{-1} \Delta T_{Bn}^{s,i} \quad (2.176)$$

however, this solution would be highly unstable, given the under-determined nature of atmospheric retrievals. The adjustment to the parameters is found by solving for the eigenvalues, $\lambda_k^{s,i}$, and eigenvector transformation matrix, $U_{j,k}^{s,i}$, of $(S_{j,n}^T)^{s,i} (N_{n,n}^s)^{-1} S_{n,j}^{s,i}$, such that

$$\Lambda_{k,k}^{s,i} \equiv (U_{k,j}^T)^{s,i} (S_{j,n}^T)^{s,i} (N_{n,n}^s)^{-1} S_{n,j}^{s,i} U_{j,k}^{s,i}. \quad (2.177)$$

Press *et. al* (1986) (pp. 350–363) provide Fortran routines for computing $\lambda_k^{s,i}$ and $U_{j,k}^{s,i}$. The 2-D matrix $\Lambda_{k,k}^{s,i}$ has only diagonal elements equal to $\lambda_k^{s,i}$. The transformation matrix, $U_{j,k}^{s,i}$, can be thought of as a transformed sensitivity matrix given by $S_{n,j}^{s,i} U_{j,k}^{s,i}$. At this point in the derivation we have not changed anything except how we are computing the inverse. Note that when computing $[\Lambda_{k,k}^{s,i}]^{-1}$ any components of $\lambda_k < 0.05^2 \lambda_k^s$ are set to zero, that is we remove the singular values. When λ_k is approaching zero both the numerator and denominator are tending toward zero. Therefore, setting those components of $\Delta A_k^{s,i+1}(0)$ to zero is most logical

$$\Delta A_j^{s,i+1}(0) = U_{j,k}^{s,i} \frac{1}{\lambda_k^{s,i}} (U_{k,j}^T)^{s,i} (S_{j,n}^T)^{s,i} (N_{n,n}^s)^{-1} \Delta T_{Bn}^{s,i}. \quad (2.178)$$

These new optimal functions can be utilized to compute a change made in transformed parameter space, is given by $\Delta B_k^{s,i+1}(0)$. Solving Eq. (2.181)

$$\begin{aligned} \Delta T_{Bn}^{s,i} &= S_{n,j}^{s,i} U_{j,k}^{s,i} \Delta B_k^{s,i+1}(0) \\ (N_{n,n}^s)^{-1} \Delta T_{Bn}^{s,i} &= (N_{n,n}^s)^{-1} S_{n,j}^{s,i} U_{j,k}^{s,i} \Delta B_k^{s,i+1}(0) \\ (U_{k,j}^T S_{j,n}^T)^{s,i} (N_{n,n}^s)^{-1} \Delta T_{Bn}^{s,i} &= (U_{k,j}^T S_{j,n}^T)^{s,i} (N_{n,n}^s)^{-1} S_{n,j}^{s,i} U_{j,k}^{s,i} \Delta B_k^{s,i+1}(0) \\ (U_{k,j}^T)^{s,i} (S_{j,n}^T)^{s,i} (N_{n,n}^s)^{-1} \Delta T_{Bn}^{s,i} &= \Lambda_{k,k}^{s,i} \Delta B_k^{s,i+1}(0), \end{aligned} \quad (2.179)$$

and

$$\begin{aligned} \Delta B_k^{s,i+1}(0) &= [\Lambda_{k,k}^{s,i}]^{-1} (U_{k,j}^T)^{s,i} (S_{j,n}^T)^{s,i} (N_{n,n}^s)^{-1} \Delta T_{Bn}^{s,i} \\ \Delta B_k^{s,i+1}(0) &= \frac{1}{\lambda_k^{s,i}} (U_{k,j}^T)^{s,i} (S_{j,n}^T)^{s,i} (N_{n,n}^s)^{-1} \Delta T_{Bn}^{s,i}. \end{aligned} \quad (2.180)$$

Again, note that when computing $[\Lambda_{k,k}^{s,i}]^{-1}$ any values of $\Delta B_k^{s,i+1}(0)$ are set to zero when $\lambda_k < 0.05^2 \lambda_c^s$. When λ_k is approaching zero both the numerator and denominator are tending toward zero, therefore, setting $\Delta B_k^{s,i+1}(0)$ to zero is most logical.

And note that the transformed parameters are related to the original parameters by the eigenvectors

$$\Delta T_{Bn}^{s,i} = S_{n,j}^{s,i} \Delta A_j^{s,i+1} = S_{n,j}^{s,i} U_{j,k}^{s,i} \Delta B_k^{s,i+1}. \quad (2.181)$$

Equation (2.181), that is, that $\Delta A_j^{s,i+1} = U_{j,k}^{s,i} \Delta B_k^{s,i+1}$, is also a statement that the original functions Eq. (2.160) have been transformed to new *optimal* functions

$$X_L^{s,i+1} = X_L^{s,i} + \sum_j \left(F_{L,j}^s \otimes \Delta \hat{A}_j^s \right) \Delta A_j^{s,i+1} = \sum_j \left(F_{L,j}^s \otimes \Delta \hat{A}_j^s \right) U_{j,k}^{s,i} \Delta B_j^{s,i+1}. \quad (2.182)$$

If no damping is required the change made in transformed parameter space, is given by $\Delta B_k^{s,i+1}(0)$. Combining Eqs. (2.176) and (2.181) yields

$$\Delta A_j^{s,i+1}(0) = U_{j,k}^{s,i} \Delta B_k^{s,i+1}(0) = U_{j,k}^{s,i} \frac{1}{\lambda_k^{s,i}} (U_{k,j}^T)^{s,i} (S_{j,n}^T)^{s,i} (N_{n,n}^s)^{-1} \Delta T_{Bn}^{s,i} \quad (2.183)$$

The changes can be damped by adding a value of $\Delta \lambda_k^{s,i}$ to the $\lambda_k^{s,i}$ such that $\lambda_k^{s,i} \geq \lambda_c^s$. This limits the noise in ΔB to a maximum value

$$\delta B_{max}^s \equiv \frac{1}{\sqrt{\lambda_c^s}} \quad \text{or} \quad (2.184)$$

$$\lambda_c^s \equiv \left(\frac{1}{\delta B_{max}^s} \right)^2. \quad (2.185)$$

The damping parameter, δB_{max}^s is determined empirically for each step. Therefore, the fraction of the transformed function solved for is defined as

$$\phi_k^{s,i} \equiv \frac{\lambda_k^{s,i}}{\lambda_k^{s,i} + \Delta \lambda_k^{s,i}} \quad (2.186)$$

which is a diagonal matrix and where $\phi_k^{s,i} = 0$ represents a parameter which is completely damped and $\phi_k^{s,i} = 1$ is completely solved for. For completely damped eigenvalues, the change to the geophysical parameters is set to zero and the first guess is unchanged for that component of the solution.

The size of $\lambda_k^{s,i}$ and, therefore, λ_c^s will be proportional to the size of the perturbation functions, $\Delta \left(\hat{A}_j^s \right)^2$ (see Eqs. (2.161) or (2.164)).

The degrees of freedom (DOF) is given by the sum of the significant eigenvalues. Given that damping has been employed, the DOF is given by

$$\text{DOF} = \sum_{k=1}^K \phi_k^{s,i} = \sum_{k=1}^K \frac{\lambda_k^{s,i}}{\lambda_k^{s,i} + \Delta\lambda_k^{s,i}}. \quad (2.187)$$

The damped change made to the transformed parameters is given by $\Delta B_k^{s,i+1} \equiv \phi_k^{s,i} \Delta B_k^{s,i+1}(0)$ which makes the damped change equal to

$$\Delta A_j^{s,i+1} = U_{j,k}^{s,i} \Delta B_k^{s,i+1} = U_{j,k}^{s,i} \phi_k^{s,i} \frac{1}{\lambda_k^{s,i}} (U_{k,j}^T)^{s,i} (S_{j,n}^T)^{s,i} (N_{n,n}^s)^{-1} \Delta T_{Bn}^{s,i}. \quad (2.188)$$

Therefore, the difference between $\Delta A_j^{s,i+1}$ and $\Delta A_j^{s,i+1}(0)$ is the amount of the solution we did not believe. If Eq. (2.188) is to be iterated we will ultimately believe all of $\Delta A_j^{s,i+1}(0)$. Therefore, the radiances need to be adjusted.

2.7.7. Rejection Criteria

A profile is rejected if any of the conditions itemized below is true. The # refers to the step # in Table 2.4.

- A row of $S_{n,j}^{s,i}$ is zero. That is all $S_{n,j}^{s,i}$ for a given j are zero in any step.
- The determined cloud fraction within ATMS footprint exceeds 80% (step # 18).
- The cloud clearing quality indicator (etarej in previous chapter) exceeds 3 on the cloud clearing after the NOAA regression (step # 12).
- The effective amplification factor exceeds 30.
- The RMSE of O – C brightness temperatures exceed 2.5 for a sub-set of ATMS channels (currently ATMS channels, . . . , are used after step # 21)

$$\left[\frac{\sum_{n=1}^L \left(\frac{1}{\text{NE}\Delta T} \right)^2 (T_{B,n,CCR} - T_{B,n}(X_L^{s=21}))^2}{\sum_{n=1}^L \left(\frac{1}{\text{NE}\Delta T} \right)^2} \right]^{\frac{1}{2}} \geq 1.75^\circ \quad (2.189)$$

- If the amplification factor exceeds 5.0 *and* the retrieval cloud fraction is between 65% and 80% *and* there is more than 10% of the cloudiness with cloud top pressure exceeding 500 hPa after step # 19.

- The quality indicator from final surface retrieval exceeds 4 (step # 20)
- The quality indicator from final temperature retrieval exceeds 4 (step # 21)
- The quality indicator from final water vapor retrieval exceeds 5

Table 2.4: Retrieval Steps in the NUCAPS Algorithm

step s	solve for	step name	computational error sources in error covariance	CrIS channels	ATMS channels
1	$T(p), \epsilon(\nu), T_s$	MIT	$q(p), L(p)$		12
2	$q(p), L(p)$	MIT	$T^\dagger(p), T_s, \epsilon(\nu), \rho_\odot(\nu)$		3
3	$T(p), \epsilon(50.3), T_s$	AMSU(Ts)	$q(p), L(p)$		11
4	$P_{\text{cld}}(i), \alpha_{\text{cld}}(i)$	ETA	$T^\dagger(p), q^\dagger(p), T_s, \epsilon(\nu), \rho_\odot(\nu)$	≤ 58	
5	R_{ccr}	ETA	$T^\dagger(p), q^\dagger(p), T_s, \epsilon(\nu), \rho_\odot(\nu)$	≤ 58	
6	$T(p), q(p), \text{O}_3$	RT_NOAA		1680	
7	$T_s, \epsilon(\nu), \rho_\odot(\nu)$	RT_NOAA		1680	
8	$T(p), \epsilon(50.3), T_s$	AMSU(Ts)	$R_{\text{ccr}}(\nu), q(p), L(p)$		11
9	$P_{\text{cld}}(i), \alpha_{\text{cld}}(i)$	ETA	$T^\dagger(p), q^\dagger(p), T_s, \epsilon(\nu), \rho_\odot(\nu)$	≤ 58	
10	R_{ccr}	ETA	$T^\dagger(p), q^\dagger(p), T_s, \epsilon(\nu), \rho_\odot(\nu)$	≤ 58	
11	$T_s, \epsilon(\nu), \rho_\odot(\nu), \bar{q}$	SURFACE	$T^\dagger(p)$	25	
12	$T(p)$	TEMP	$R_{\text{ccr}}(\nu), q(p), \text{O}_3(p), L(p), T_s,$ $\epsilon(\nu), \rho_\odot(\nu), \text{CO}_2$	108	7
13	$q(p)$	WATER	$R_{\text{ccr}}(\nu), T^\dagger(p), L(p), T_s,$ $\epsilon_{\text{mw}}(f), \rho_\odot(\nu), \text{CH}_4(p)$	44	3
14	$\text{O}_3(p)$	OZONE	$R_{\text{ccr}}(\nu), q(p), T_s, \epsilon(\nu)$	34	
15	$T(p), \epsilon(50.3)$	AMSU(RJ)	$R_{\text{ccr}}(\nu), q(p), L(p), T_s$		11
16	$P_{\text{cld}}(i), \alpha_{\text{cld}}(i)$	ETA	$T^\dagger(p), q^\dagger(p), T_s, \epsilon(\nu), \rho_\odot(\nu)$	≤ 58	
17	R_{ccr}	ETA	$T^\dagger(p), q^\dagger(p), T_s, \epsilon(\nu), \rho_\odot(\nu)$	≤ 58	
18	$T_s, \epsilon(\nu), \rho_\odot(\nu)$	SURFACE	$R_{\text{ccr}}(\nu), T^\dagger(p), q^\dagger(p)$	25	
19	$T(p)$	TEMP	$R_{\text{ccr}}(\nu), q(p), \text{O}_3(p), L(p), T_s,$ $\epsilon(\nu), \rho_\odot(\nu), \text{CO}_2$	124	7
20	$\text{CO}(p)$	CO	$R_{\text{ccr}}(\nu), T(p), q(p), T_s$	36	
21	$\text{CH}_4(p)$	CH4	$R_{\text{ccr}}(\nu), T(p), q(p), T_s$	71	
22	CO_2	CO2	$R_{\text{ccr}}(\nu), T(p), q(p), T_s$ $\text{O}_3, \rho_\odot(\nu)$	70	
23	$\text{HNO}_3(p)$	HNO3	$R_{\text{ccr}}(\nu), T(p), q(p), T_s$	8	
24	$\text{N}_2\text{O}(p)$	N2O	$R_{\text{ccr}}(\nu), T(p), q(p), T_s$	52	
25	$\text{SO}_2(p)$	SO2	$R_{\text{ccr}}(\nu), T(p), q(p), T_s$	63	

† indicates that off-diagonal elements are not used

Table 2.5: Scale Size of Perturbation Functions in v2.0

retrieval step	$\Delta \hat{A}_j^s$					trace
	T_s	$\epsilon(\nu)$	$\rho(\nu)$	$T(p)$	$q(p)$	
RETAMSU	1K	1%		1K		
RETSURF	3K	1%	0.5%	3K	20%	
RETTMP				1K		
RETWATR					10%	
RETOZON						10%
RET_CO						10%
RET_CH4						2%
RET_CO2						1%
RET_HNO3						20%
RET_N2O						5%
RET_SO2						50%

2.8. Validation

2.8.1. Sounder Validation Methodology

This section overviews the NUCAPS validation methodology, which is generally applicable to operational products obtained from the NUCAPS CrIS/ATMS, IASI and AIRS systems. Section 2.8.1 focuses on EDRs required to be validated on profile layers (viz., temperature, water vapor and ozone), whereas Section 2.8.2 focuses on carbon trace gas EDRs required only to be validated on total atmospheric columns. Validation results for NOAA-20 and Metop-A/B/C NUCAPS are discussed in Section 2.8.2.

Temperature, Moisture and Ozone Profiles

The standard methodology and theoretical basis for validation of satellite sounder retrieved atmospheric temperature, $T(p)$, moisture, $Q(p)$, and ozone, O_3 , profile EDRs was formalized by Nalli et al. (2013) and is overviewed here. Sounder profile EDR validation is performed versus a quasi-independent baseline measurement often referred to as “truth” data. Because validation is an ongoing process, a *sounder validation hierarchy* paradigm has been established based roughly upon the relative strengths of the datasets used (Barnet, 2009; Nalli et al., 2013). Techniques/datasets at the beginning of the hierarchy are those typically used at the early stages of EDR validation (i.e., early in the satellite mission), whereas those near the end are typically applied in the later stages. For example, the Joint Polar Satellite System (JPSS) cal/val program has adopted a phased approach to cal/val over the satellite mission lifetimes (Barnet, 2009; Zhou et al., 2016).

1. **NWP Model Global Comparisons.** Numerical weather prediction (NWP) models (e.g., ECMWF, NCEP/GFS) allow for large, truly global samples acquired from global “Focus Days”; they are useful for sanity checks, bias tuning and regression, but are otherwise not considered independent truth data. But more importantly, models are essential for performing “double-differences” and can serve as a “transfer-standard” for analyzing retrievals from different platforms.
2. **Satellite EDR Intercomparisons.** As with NWP models, intercomparisons with other independent satellite EDRs (e.g., AIRS, COSMIC) allow for global samples acquired from Focus Days, however other sensors (e.g., AIRS) may have similar error characteristics, and a rigorous assessment would need to account for the averaging kernels of both systems (e.g., Rodgers and Connor, 2003).

-
3. **Radiosonde Matchup Assessments.** Operational sonde networks can be collocated with satellite overpasses within broad space-time matchup windows to allow characterization of the satellite EDRs versus *in situ* measurements with representation of global zones and large samples within a couple month's acquisition period (e.g., Divakarla et al., 2006, 2008; Nalli et al., 2018b). This technique has been routinely implemented as part of the NOAA Products Validation System (NPROVS) (Reale et al., 2012; Sun et al., 2017), which also facilitates long-term monitoring. However, limitations include skewed distribution toward NH-continent, mismatch errors (Sun et al., 2010), and the assimilation of these data into models, thereby limiting their independence.
 4. **Dedicated/Reference Radiosonde Assessments.** Dedicated radiosondes and ozonesondes are allocated for the explicit purpose of satellite validation, these generally being state-of-the-art instrument packages (e.g., Vaisala radiosondes) that are launched synchronized in space and time with satellite overpasses, thereby minimizing measurement and mismatch uncertainties. Reference measurements (e.g., frost-point hygrometer and GRUAN-processed sondes) are traceable measurements typically including uncertainty estimates. While these datasets provide an optimal truth measurement (with minimized combined measurement uncertainties), they are limited by relatively small sample sizes and sparse geographic coverage.
 5. **Intensive Field Campaign Assessments/Dissections.** Intensive field campaigns typically include dedicated sondes and ancillary datasets (e.g., lidar, sunphotometer, etc.); ideally they also include a funded aircraft IR spectrometer (e.g., NAST-I, S-HIS) for SDR cal/val. The combination of these datasets enables detailed performance specification, geophysical state specification, as well as deep-dive case studies. Examples of traditional funded cal/val intensive field campaigns include European Aqua Thermodynamic Experiment (EAQUATE) (Taylor et al., 2008), Joint Airborne IASI Validation Experiment (JAIVEX) (Newman et al., 2012), the AIRS Water Vapor Experiment–Ground (AWEX-G) (Milochevich et al., 2006). More recently, multi-disciplinary opportunistic campaigns have been leveraged for the remote sensing cal/val objective, including Aerosols and Ocean Science Expeditions (AEROSE) (Morris et al., 2006; Nalli et al., 2006, 2011), the CalWater and ARM Cloud Aerosol and Precipitation Experiment (ACAPEX), and the El Niño Rapid Response (ENRR).

The Joint Polar Satellite System (JPSS) Level 1 Performance Requirements for temperature and moisture profiles are given in Tables 2.6 and 2.7, respectively. The

requirements are defined for global, non-precipitating cases on 3–5 atmospheric “broad-layers” that are computed as an average of 1–5 km “coarse-layers” for temperature and 2 km for moisture. “Partly Cloudy” conditions are defined by successful cloud-clearing and IR retrieval, whereas “Cloudy” conditions are defined by cases where cloud-clearing was not successful, thereby resulting in a MW-only algorithm solution as the final product. These tables provide the metrics by which the system is considered to have reached Validated Maturity and has met mission requirements (Zhou et al., 2016; Nalli et al., 2018a).

Conversion of Profile Truth Data to Correlative Layers. Comparisons between high-resolution *in situ* measurements (e.g., RAOBs) with coarser-resolution satellite EDR retrievals require that the RAOB measurements first be reduced to correlative effective RTA layer quantities consistent with the forward model utilized by the retrieval. The approach is to integrate column density weighted quantities from the top to the bottom of the observed atmospheric column, interpolate those to the RTA layer boundaries (i.e., levels), then compute the RTA layer quantities from the interpolated level values. MATLAB and Fortran programs, `conv_layers.m` and `conv_layers.F`, has been developed for calculating performing the reduction to layers. The theoretical basis is overviewed below (Nalli et al., 2013).

Effective layer pressures, \bar{p}_L , are defined as $\bar{p}_L \equiv \int_{z_{l+1}}^{z_l} p(z) dz / \int_{z_{l+1}}^{z_l} dz$ where z is geopotential height, and subscripts l denote layer boundaries (i.e., levels). It can be shown that for the $n_l = 101$ standard RTA standard pressure levels (Strow et al., 2003), the $n_L = n_l - 1 = 100$ RTA layer pressures can then be derived as (Nalli et al., 2013)

$$\bar{P}_{\text{RTA},L} = \frac{P_{l+1} - P_l}{\ln(P_{l+1}/P_l)}, \quad l = L = 1, 2, \dots, n_L, \quad (2.190)$$

where uppercase P denote RTA pressures, and subscripts L and l denote layer and level, respectively.

For correlative measurements or observations, lowercase p denotes pressure, and subscripts \mathcal{L} and ℓ denote layer and level, respectively. Generally speaking, RAOB data are at higher vertical resolution than the RTA, with the number of RAOB points much greater than the RTA pressure levels. Given a typical sounding measuring pressure, temperature and humidity (PTU), the number density (molecules/cm³) for air is given (in CGS units) by (e.g., Wallace and Hobbs, 1977)

$$N_{a,\ell}(p_\ell, T_\ell) = 10^3 \frac{p_\ell}{k T_\ell}, \quad \ell = 1, 2, \dots, n_\ell, \quad (2.191)$$

where k is the Boltzmann constant in ergs, p_ℓ and T_ℓ are pressure (hPa) and temperature (K) measured at observation level ℓ , and the 10^3 factor converts pressure from

Table 2.6: JPSS Level 1 Requirements^a for CrIS/ATMS Atmospheric Vertical Temperature Profile (AVTP) EDR Measurement Uncertainty

GLOBAL AVTP MEASUREMENT UNCERTAINTY REQUIREMENT ^b		
Atmospheric Broad-Layer	Threshold	Objective
<i>Cloud-Free to Partly Cloudy (IR+MW)^c</i>		
Surface to 300 hPa ^d (1 km layers)	1.6 K	0.5 K
300 hPa to 30 hPa (3 km layers)	1.5 K	0.5 K
30 hPa to 1 hPa (5 km layers)	1.5 K	0.5 K
1 hPa to 0.5 hPa (5 km layers)	3.5 K	0.5 K
<i>Cloudy (MW-only)^e</i>		
Surface to 700 hPa (1 km layers)	2.5 K	0.5 K
700 hPa to 300 hPa (1 km layers)	1.5 K	0.5 K
300 hPa to 30 hPa (3 km layers)	1.5 K	0.5 K
30 hPa to 1 hPa (5 km layers)	1.5 K	0.5 K
1 hPa to 0.5 hPa (5 km layers)	3.5 K	0.5 K

^a Source: Joint Polar Satellite System (JPSS) Program Level 1 Requirements Supplement – Final, Version 2.10, 25 June 2014, NOAA/NESDIS.

^b Expressed as an error in layer average temperature.

^c Partly cloudy conditions are those where both the IR and MW retrievals are used and are typically scenes with $\leq 50\%$ cloudiness.

^d The IR+MW surface to 300 hPa requirement is for over global ocean. Over land and ice mass, the Uncertainty is relaxed slightly to 1.7 K due to the state of the science of the land emissivity knowledge within the temperature sounding algorithm.

^e Cloud conditions are those where only the MW retrievals are used and are typically scenes with $> 50\%$ cloudiness.

hPa to dPa. Number densities for moisture and ozone, $N_{w,\ell}$ and $N_{o,\ell}$ (molecules/cm³), are calculated from the radiosonde measurements of relative humidity (RH) % and O₃ partial pressure (mPa). For ozone the total atmospheric pressure in (2.191) is

Table 2.7: JPSS Level 1 Requirements^a for CrIS/ATMS Atmospheric Vertical Moisture Profile (AVMP) EDR Measurement Uncertainty

GLOBAL AVMP MEASUREMENT UNCERTAINTY REQUIREMENT ^b		
Atmospheric Broad-Layer	Threshold	Objective
<i>Cloud-Free to Partly Cloudy (IR+MW)^c</i>		
Surface to 600 hPa	greater of 20% or 0.2 g kg ⁻¹	10%
600 hPa to 300 hPa	greater of 35% or 0.1 g kg ⁻¹	10%
300 hPa to 100 hPa	greater of 35% or 0.1 g kg ⁻¹	10%
<i>Cloudy (MW-only)^d</i>		
Surface to 600 hPa	greater of 20% or 0.2 g kg ⁻¹	10%
600 hPa to 300 hPa	greater of 40% or 0.1 g kg ⁻¹	10%
300 hPa to 100 hPa	greater of 40% or 0.1 g kg ⁻¹	NS

^a Source: Joint Polar Satellite System (JPSS) Program Level 1 Requirements Supplement – Final, Version 2.10, 25 June 2014, NOAA/NESDIS.

^b Expressed as a percent of average in 2 km layers.

^c Partly cloudy conditions are those where both the IR and MW retrievals are used and are typically scenes with $\leq 50\%$ cloudiness.

^d Cloud conditions are those where only the MW retrievals are used and are typically scenes with $> 50\%$ cloudiness.

replaced with the measurement of O₃ partial pressure (in mPa) and multiplied by a factor of 10⁻² to convert to dPa. Similarly, number density for water vapor can be obtained by replacing the total pressure p_ℓ in Eq. (2.191) by the water vapor partial pressure, e_ℓ . The vapor pressure can be calculated directly from RAOB RH as (e.g., Stull, 2000)

$$e_\ell = e_s(T_\ell) \frac{\text{RH}}{100\%}, \quad (2.192)$$

where e_s is the saturation vapor pressure (SVP) for temperature T_ℓ . Because radiosondes typically measure RH, Eq. (2.192) requires the calculation of SVP (e_s) (Miloshevich et al., 2006; Wexler, 1976; Hyland and Wexler, 1983). The H₂O number

Table 2.8: JPSS Level 1 Requirements* for IR Ozone Profile EDR

IR OZONE PROFILE (CRIS) LAYER AVERAGE REQUIREMENT		
Atmospheric Broad-Layer	Threshold	Objective
<i>Precision (random error, σ)</i>		
Surface to 260 hPa (6 statistic layers)	20%	10%
260 hPa to 4 hPa (1 statistic layer)	20%	10%
<i>Accuracy (systematic error, bias)</i>		
Surface to 260 hPa (6 statistic layers)	$\pm 10\%$	$\pm 5\%$
260 hPa to 4 hPa (1 statistic layer)	$\pm 10\%$	$\pm 5\%$
<i>Combined Uncertainty (RMSE)</i>		
Surface to 260 hPa (6 statistic layers)	25%	15%
260 hPa to 4 hPa (1 statistic layer)	25%	15%

*Source: Joint Polar Satellite System (JPSS) Program Level 1 Requirements Supplement — Final, Version 2.9, 27 June 2013, NOAA/NESDIS, p. 49.

density can be calculated from mass mixing ratio (r_ℓ) as

$$N_{w,\ell}(p_\ell, T_\ell, r_\ell) = 10^3 \frac{p_\ell}{(1 + \epsilon/r_\ell) k T_\ell}, \quad \ell = 1, 2, \dots, n_\ell. \quad (2.193)$$

where ϵ is the ratio of the molecular masses of water vapor and dry air, $\epsilon \equiv M_w/M_d \approx 0.622$.

Integrated column abundances (from the top measurement z_t to the measurement

level height z) for atmospheric species x (molecules/cm²), defined as

$$\Sigma_x(z) \equiv \int_{z_t}^z N_x(z') dz', \quad (2.194)$$

are calculated as

$$\begin{aligned} \Sigma_x(z) &\approx \Sigma_{x,\mathcal{L}} \equiv \sum_{\mathcal{L}}^{n_{\mathcal{L}}} \bar{N}_{x,\mathcal{L}} \delta z_{\mathcal{L}}, & \mathcal{L} = \ell = 1, 2, \dots, n_{\mathcal{L}} \\ &\approx \sum_{\ell}^{n_{\ell}} \left(\frac{N_{x,\ell+1} + N_{x,\ell}}{2} \right) (z_{\ell+1} - z_{\ell}), & (N_{x,\ell+1} \wedge N_{x,\ell}) > 0. \end{aligned} \quad (2.195)$$

where $\bar{N}_{x,\mathcal{L}} \delta z_{\mathcal{L}}$ are the $n_{\mathcal{L}} = n_{\ell} - 1$ fine-layer (geopotential thicknesses $\delta z_{\mathcal{L}} \equiv z_{\ell+1} - z_{\ell}$) mean abundances.

In a similar manner, the temperature profile is integrated weighted by the air number density,

$$\Sigma_T(z) \equiv \int_{z_t}^z T(z') N_a(z') dz', \quad (2.196)$$

which is calculated as

$$\begin{aligned} \Sigma_T(z) &\approx \Sigma_{T,\mathcal{L}} \equiv \sum_{\mathcal{L}}^{n_{\mathcal{L}}} \bar{T}_{\mathcal{L}} \bar{N}_{a,\mathcal{L}} \delta z_{\mathcal{L}}, & \mathcal{L} = \ell = 1, 2, \dots, n_{\mathcal{L}}, \\ &\approx \sum_{\ell}^{n_{\ell}} \left(\frac{T_{\ell+1} + T_{\ell}}{2} \right) \left(\frac{N_{a,\ell+1} + N_{a,\ell}}{2} \right) (z_{\ell+1} - z_{\ell}), & (N_{a,\ell+1} \wedge N_{a,\ell}) > 0. \end{aligned} \quad (2.197)$$

The calculations from Eqs. (2.195) and (2.197) are linearly interpolated to the truncated RTA pressure vector \mathbf{P} (spanning the measured column), and simply denoted $\Sigma_{x,\mathcal{L}}(\mathbf{P})$ and $\Sigma_{T,\mathcal{L}}(\mathbf{P})$, respectively. \mathbf{P} is defined as RTA pressure levels P_l including the observed surface and top levels. The top RTA level l_0 is defined simply as the level just below the top observed pressure level, p_0 (e.g., at balloon burst altitude). Because of variable terrain and surface pressure, the bottom level, l_b , is defined consistent with the RTA calculation used in the retrieval algorithm. The interpolation vector \mathbf{P} is given by

$$\mathbf{P} \equiv \begin{cases} [p_t, P_{l_t}, P_{l_t+1}, \dots, P_{l_b-1}, P_{l_b}, p_s], & 0 < p_s - P_{l_b} < 5 \text{ hPa} \\ [p_t, P_{l_t}, P_{l_t+1}, \dots, P_{l_b-1}, p_s, P_{l_b}], & p_s - P_{l_b-1} \geq 5 \text{ hPa}. \end{cases} \quad (2.198)$$

Given $\Sigma_{x,\mathcal{L}}(\mathbf{P})$ and $\Sigma_{T,\mathcal{L}}(\mathbf{P})$, the effective RTA layer quantities are calculated as follows. The effective layer pressures \bar{P}_L are computed from (2.190) using the levels defined in (2.198). Given $\Sigma_{a,\mathcal{L}}(\mathbf{P})$ and $\Sigma_{T,\mathcal{L}}(\mathbf{P})$, the effective layer temperatures,

$T_L(\bar{P}_L)$ are calculated as

$$T_L(\bar{P}_L) = \frac{\Sigma_{T,\mathcal{L}}(P_{l+1}) - \Sigma_{T,\mathcal{L}}(P_l)}{\Sigma_{a,\mathcal{L}}(P_{l+1}) - \Sigma_{a,\mathcal{L}}(P_l)}, \quad l = L = 1, 2, \dots, m_L, \quad (2.199)$$

where m_L is the length of vector \mathbf{P} . Given $\Sigma_{x,\mathcal{L}}(\mathbf{P})$, and $\bar{T}_L(\bar{P}_L)$ from (2.199), effective layer water vapor mass mixing ratio (g/kg relative to dry air) is calculated as

$$r_{w,L}(\bar{P}_L) = \epsilon \cdot 10^3 \frac{\Sigma_{w,\mathcal{L}}(P_{l+1}) - \Sigma_{w,\mathcal{L}}(P_l)}{\bar{N}_{a,L} \delta z_L - [\Sigma_{w,\mathcal{L}}(P_{l+1}) - \Sigma_{w,\mathcal{L}}(P_l)]}, \quad (2.200)$$

where $\epsilon \equiv M_w/M_d \approx 0.622$ (M_w and M_d the molecular weights of water and dry air, respectively), and the atmospheric mean layer abundance is given by

$$\bar{N}_{a,L} \delta z_L \equiv 10^3 \frac{\bar{P}_L}{k \bar{T}_L(\bar{P}_L)} \delta z_L, \quad (2.201)$$

and $\delta z_L \equiv z(P_l) - z(P_{l+1})$. Likewise, the effective layer ozone volumetric mixing ratio (ppbv, dry air) is calculated as

$$r_{o,L}(\bar{P}_L) = 10^9 \frac{\Sigma_{o,\mathcal{L}}(P_{l+1}) - \Sigma_{o,\mathcal{L}}(P_l)}{\bar{N}_{a,L} \delta z_L - [\Sigma_{w,\mathcal{L}}(P_{l+1}) - \Sigma_{w,\mathcal{L}}(P_l)]}. \quad (2.202)$$

Coarse-Layer Statistics. Given correlative truth profiles on effective RTA layers (§2.8.1), profile error statistics are computed on coarse-layers using the SIMSTAT program developed and maintained at NOAA (separate Fortran, MATLAB and IDL code versions have been developed). The theoretical basis for this is detailed in Nalli et al. (2013) and overviewed below.

The root mean square error (RMSE) provides a single metric that includes all deviations (systematic and random) in the matchup sample. RTA effective layer temperatures T_L are averaged to obtain coarse layer values

$$T_{\mathcal{L}} = \frac{\sum_{L(\mathcal{L})} \ln\left(\frac{P_{\ell}}{P_{\ell-1}}\right) T_L}{\ln\left(\frac{P_{\mathcal{L}}}{P_{\mathcal{L}-1}}\right)}, \quad (2.203)$$

where $L(\mathcal{L})$ are the RTA layers that fall within the coarse layer \mathcal{L} . Defining the deviation of a temperature profile retrieval from a correlative profile on $n_{\mathcal{L}} \simeq 20$ coarse layers at a matchup location j as $\Delta T_{\mathcal{L},j} \equiv \hat{T}_{\mathcal{L},j} - T_{\mathcal{L},j}$, the RMSE deviation is given by

$$\text{RMSE}(\Delta T_{\mathcal{L}}) = \sqrt{\frac{1}{n_j} \sum_{j=1}^{n_j} (\Delta T_{\mathcal{L},j})^2} \quad \mathcal{L} = 1, 2, \dots, n_{\mathcal{L}}, \quad (2.204)$$

where n_j is the matchup sample size. The measure of sample bias is calculated simply as the mean difference

$$\text{BIAS}(\Delta T_{\mathcal{L}}) \equiv \overline{\Delta T}_{\mathcal{L}} = \frac{1}{n_j} \sum_{j=1}^{n_j} \Delta T_{\mathcal{L},j}. \quad (2.205)$$

Variability is measured by the standard deviation, σ

$$\text{STD}(\Delta T_{\mathcal{L}}) \equiv \sigma(\Delta T_{\mathcal{L}}) = \sqrt{\frac{1}{n_j} \left[\sum_{j=1}^{n_j} (\Delta T_{\mathcal{L},j})^2 - \frac{(\sum_{j=1}^{n_j} \Delta T_{\mathcal{L},j})^2}{n_j} \right]}, \quad (2.206)$$

which from Eqs. (2.204) and (2.205) can be conveniently expressed in terms of the RMSE and BIAS as

$$\text{STD}(\Delta T_{\mathcal{L}}) = \sqrt{[\text{RMSE}(\Delta T_{\mathcal{L}})]^2 - [\text{BIAS}(\Delta T_{\mathcal{L}})]^2}. \quad (2.207)$$

For computing vertical profile statistics of gas concentration EDRs (viz., H₂O and O₃) on coarse-layers, both retrieval and truth profiles (in RTA layer abundances) are summed over each coarse-layer and converted to mass abundances in g/cm². For H₂O, the RTA layer abundances are denoted as q_L , and the coarse-layer mass abundances $q_{\mathcal{L}}$ are calculated as

$$q_{\mathcal{L}} = \frac{M_w}{N_A} \sum_{L(\mathcal{L})} q_L, \quad (2.208)$$

where M_w is H₂O molecular mass, N_A is Avogadro's number, and $L(\mathcal{L})$ is as above in Equation (2.203), with the bottom partial layer L_b multiplied by the bottom-layer (BLMULT) factor

$$\mathcal{F}_{\text{BL}} \equiv \frac{p_s - P_{l_b-1}}{P_{l_b} - P_{l_b-1}}, \quad (2.209)$$

where l_b denotes the bottom layer lower boundary.

Given coarse layer abundances, $q_{\mathcal{L}}$, the fractional deviation is taken to be the absolute deviation divided by the observed (e.g., RAOB) value

$$\Delta q_{\mathcal{L},j} \equiv \frac{\widehat{q}_{\mathcal{L},j} - q_{\mathcal{L},j}}{q_{\mathcal{L},j}}, \quad \mathcal{L} = 1, 2, \dots, n_{\mathcal{L}}. \quad (2.210)$$

The denominator in Eq. (2.210) can result in large $\Delta q_{\mathcal{L},j}$ in dry atmospheres (e.g., mid to upper troposphere or polar regions) and thereby skew the statistics toward these cases. Therefore, sounder science team cal/val convention has been to implement

general weighted means (as opposed to simple arithmetic means) as the basis for the statistics:

$$\text{RMSE}(\Delta q_{\mathcal{L}}) = \sqrt{\frac{\sum_{j=1}^{n_j} W_{\mathcal{L},j} (\Delta q_{\mathcal{L},j})^2}{\sum_{j=1}^{n_j} W_{\mathcal{L},j}}}, \quad (2.211)$$

$$\text{BIAS}(\Delta q_{\mathcal{L}}) = \frac{\sum_{j=1}^{n_j} W_{\mathcal{L},j} \Delta q_{\mathcal{L},j}}{\sum_{j=1}^{n_j} W_{\mathcal{L},j}}, \quad (2.212)$$

where the water vapor weighting factor, $W_{\mathcal{L},j}$, assumes one of three forms (W^0 , W^1 or W^2)

$$W_{\mathcal{L},j} = \begin{cases} 1 & , \quad W^0 \\ q_{\mathcal{L},j} & , \quad W^1 \\ (q_{\mathcal{L},j})^2 & , \quad W^2. \end{cases} \quad (2.213)$$

W^0 ($W_{\mathcal{L},j} = 1$) reduces Eqs. (2.211) and (2.212) to arithmetic means. To minimize skewing impact of dry atmospheres, sounder science team convention has been to use W^2 for RMSE Eq. (2.211). Because JPSS Level 1 requirements for RMSE were derived based upon statistics using W^2 weighting, it is reasonable that validation requirement assessments should also use this weighting (Nalli et al., 2013). It is also suggested that BIAS calculations consistently use the W^2 weighting (rather than W^1) to avoid confusion and allow compatible calculations of STD from

$$\text{STD}(\Delta q_{\mathcal{L}}) = \sqrt{[\text{RMSE}(\Delta q_{\mathcal{L}})]^2 - [\text{BIAS}(\Delta q_{\mathcal{L}})]^2}. \quad (2.214)$$

For ozone, given a correlative ozone sounding (e.g., from an ozonesonde), statistics are calculated in a manner similar to the water vapor, namely Eqs. (2.211) and (2.212), with W^2 weighting recommended for RMSE and BIAS. Once coarse-layer statistics are obtained, approximate “broad-layer” results are taken to be the averages of coarse-layers over the broad-layers.

Carbon Trace Gas Validation

Unlike previous sounder systems (e.g., AIRS and IASI), the JPSS satellite sounder EDR cal/val program has for the first time specified requirements for carbon trace gases. Because NUCAPS has relatively limited degrees-of-freedom (DoF) for carbon gases (DoF ≈ 1), JPSS requirements are defined for total column quantities as given in Table 2.9.

In response to the JPSS requirements, an analogous validation hierarchy was subsequently devised as follows (Nalli et al., 2020):

Table 2.9: JPSS Level 1 Requirements for CrIS Infrared Carbon Trace Gas EDR Measurement Uncertainty*

CRIS TOTAL COLUMN TRACE GAS EDR* MEASUREMENT UNCERTAINTY REQUIREMENT		
EDR Attribute	Threshold	Objective
<i>Carbon Monoxide (CO) EDR</i>		
Precision	15%	3%
Accuracy	±5%	±5%
<i>Carbon Dioxide (CO₂) EDR</i>		
Precision	0.5% (2 ppmv)	1.05–1.4 ppmv
Accuracy	±1% (4 ppmv)	NS
<i>Methane (CH₄) EDR</i>		
Precision	1% (≈20 ppbv)	NS
Accuracy	±4% (≈80 ppmv)	NS

*Source: Joint Polar Satellite System (JPSS) Program Level 1 Requirements Supplement – Final, Version 2.10, 25 June 2014, NOAA/NESDIS.

- 1. Global Dynamical-Chemistry Model Comparisons.** As in Section 2.8.1, comparisons NUCAPS carbon gas retrievals may be compared against global chemistry models for global Focus Days, and can be used as a “transfer-standard” as above. Models suitable for trace gases include the NOAA CarbonTracker (Jacobson et al., 2020), and the Copernicus Atmosphere Monitoring Service (CAMS) (Inness et al., 2019).
- 2. Satellite EDR Intercomparisons.** Also as in Section 2.8.1, intercomparisons can be performed for global Focus Days against EDRs retrieved from other satellite sensors, especially air quality and carbon missions, including the Tropospheric Monitoring Instrument (TROPOMI) onboard the Copernicus Sentinel-5, the NASA Orbiting Carbon Observatory (OCO-2), Greenhouse gases Observ-

ing Satellite (GOSAT), and the Aura Microwave Limb Sounder (MLS). Note that the JPSS requirements to validate total column quantities (as opposed to profiles) mitigates the need for applying averaging kernels in performing intercomparisons.

3. **Surface-Based Network Matchup Assessments.** Ground-based observations obtained periodically from surface-based observing networks provide independent truth datasets with a global distribution reasonably representing global latitude zones roughly analogous to sondes, including total column profiles from the Total Carbon Column Observing Network (TCCON) Wunch et al. (2011), and *in situ* vertical profiles obtained from the balloon-borne AirCore sampling system (Karion et al., 2010; Membrive et al., 2017). Although sample sizes are thus limited, these data nevertheless provide valuable independent “spot checks” at collocated stations for given Focus Days, these supplementing large datasets available from the model and satellite comparisons stated above.
4. **Aircraft Campaign Data Assessments.** At the top of the hierarchy are aircraft campaigns that provide comprehensive sets of *in situ* vertical profile data from ascents and descents of dedicated aircraft flying over specified regions. Examples of atmospheric composition campaigns suitable for IR sounder validation include the Atmospheric Tomography (ATom) mission (Wofsy et al., 2018) and, previously, the HIAPER Pole-to-Pole Observations (HIPPO) (Wofsy et al., 2011) campaigns.

Computation of Total Column Abundances. Both NUCAPS and AIRS perform retrievals of trace gas concentrations carbon monoxide (CO) and methane (CH₄) (as well as H₂O) in layer abundance space (molecules/cm²). Carbon dioxide (CO₂), on the other hand, is treated differently (for reasons explained elsewhere in this ATBD) and is retrieved in mole fraction mixing ratios in ppm. Thus, for CO and CH₄, the column assessments are performed for total column quantities simply by integrating the retrieved layer abundances, whereas for CO₂ the assessments are performed for simply column averages. As in Section 2.8.1, integrated total column abundances for CO and CH₄ are obtained based on Equation (2.194) and computed as

$$\Sigma_x(z_s) \approx \mathcal{F}_{\text{BL}} \overline{N}_{x,L_b} \delta z_{L_b} + \sum_L^{L_b-1} \overline{N}_{x,L} \delta z_L, \quad (2.215)$$

where z_s is the surface altitude and the quantities $\overline{N}_{x,L} \delta z_L$ are the NUCAPS retrieved layer abundance for gas species x and RTA layer L , L_b is the bottom partial layer, and \mathcal{F}_{BL} is the bottom-layer multiplier factor defined by Equation (2.209).

TCCON data are provided in total column dry mole fractions (in ppm), x_i , which thus require conversions to total column abundances (molecules/cm²). Details on the conversions, integration and application of the TCCON averaging kernels may be found in the appendix of Nalli et al. (2020).

2.8.2. SNPP, NOAA-20 and Metop-A/B/C NUCAPS Validation

Validation of the operational NOAA operational sounder algorithms has been ongoing and has proceeded in phases in response to changes in the CrIS/ATMS SDRs, the EDR algorithm, and target satellite missions (Aqua, SNPP, NOAA-20 and Metop-A/B/C satellites). Prior to the selection of NUCAPS as the operational algorithm, the NPOESS-era SNPP Cross-track Infrared Microwave Sounder Suite (CrIMSS) was first developed and validated (Divakarla et al., 2014). After the switch from SNPP CrIMSS to NUCAPS, the SNPP CrIS nominal spectral resolution (NSR) NUCAPS algorithm formally attained Validated Maturity in September 2014 (Zhou et al., 2016) based upon global analyses detailed in Nalli et al. (2018a,b) and supported by additional analyses performed by Sun et al. (2017). Changes to the SNPP CrIS SDRs included the switch to full spectral resolution (FSR) mode in December 2014 along with the switch to Side-2 in July 2019, both events requiring re-validation of the NUCAPS EDR products. The addition of the carbon trace gas (CO, CH₄, CO₂) to the suite of JPSS program sounder EDRs then required their own updates and development, followed by formal global validation for both SNPP and NOAA-20 (demonstrating compliance with mission requirements without degrading the usual temperature, moisture and O₃ EDRs). The results of the carbon trace gas validation are now detailed in Nalli et al. (2020).

JPSS has directly and indirectly funded a dedicated radiosonde program leveraging a number of collaborating institutions. Dedicated radiosondes are optimally collocated and synchronous with SNPP overpasses at various selected sites. In addition, we have leveraged GCOS Reference Upper Air Network (GRUAN) RAOB sites. Collocations of NUCAPS FORs with RAOBs are facilitated via the NOAA Products Validation System (NPROVS) Reale et al. (2012). Based on this RAOB-satellite collocation system, an EDR validation archive (VALAR) has been created whereby CrIS SDR and ATMS temperature data record (TDR) granules in the vicinity of RAOB “anchor points” are acquired for running offline retrievals, thus allowing validation flexibility (e.g., enables ozone and trace gas validation) and ongoing algorithm optimization and development.

Figure 2.15 shows JPSS-funded dedicated RAOB sites for the SNPP NUCAPS temperature and moisture profile validation effort as of this writing through 2016. These include U.S. DOE Atmospheric Radiation Measurement (ARM) sites (Tobin

et al., 2006; Mather and Voyles, 2013) and the ship-based 2019 NOAA Aerosols and Ocean Science Expedition (AEROSE) (Morris et al., 2006; Nalli et al., 2011). Additionally, collaborative land-based sites-of-opportunity have included the Howard University Beltsville Campus (BEL) site in Beltsville, Maryland, and there are three GRUAN sites that fortuitously collocate with NOAA-20 (and SNPP) overpasses Bodeker et al. (2016). Likewise, Figure 2.16 shows ozonesonde sites for the NOAA-20 NUCAPS IR

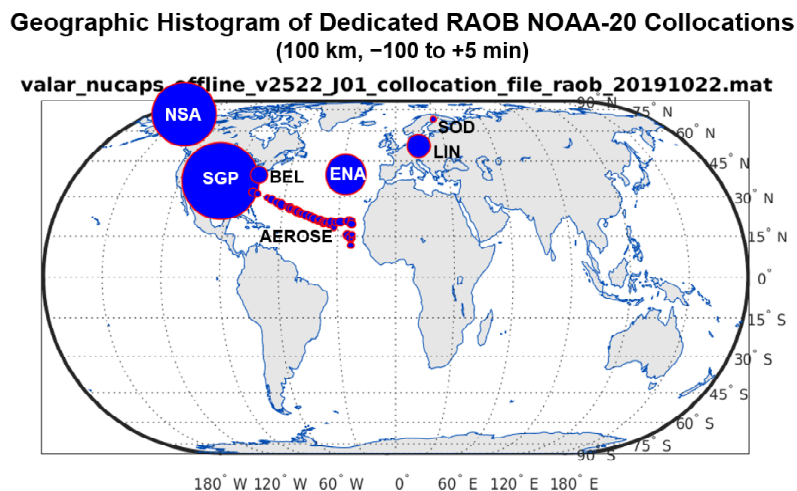


Figure 2.15: Geographic histograms of NOAA-20 dedicated and GRUAN reference RAOB collocations NUCAPS EDR validation, including ARM sites, collaborative partner sites (BEL), collocated GRUAN reference sites, and the 2019 AEROSE campaign.

ozone profile validation, which include Southern Hemisphere Additional Ozonesonde (SHADOZ) (Thompson et al., 2004) and Ozone and Ultraviolet Radiation Data Centre (WOUDC) network sites, along with unique ship-based dedicated ECC ozonesondes launched during the 2019 AEROSE cal/val campaigns.

Result Highlights

Coarse-layer and broad-layer uncertainties (using the methodologies described in Section 2.8.1) for the operational NUCAPS algorithm for NOAA-20 (offline v2.5.2.2) and Metop-A/B/C are highlighted here. To minimize mismatch error in the statistical analyses, stringent space-time collocation criteria were employed, along with a geographic zonal and land/sea surface area weighting scheme has been employed. This latter scheme provides proportionately greater weight to tropical ocean RAOB collocations and lesser weight to high-latitude land-based collocations, which is in accordance with the JPSS global requirements.

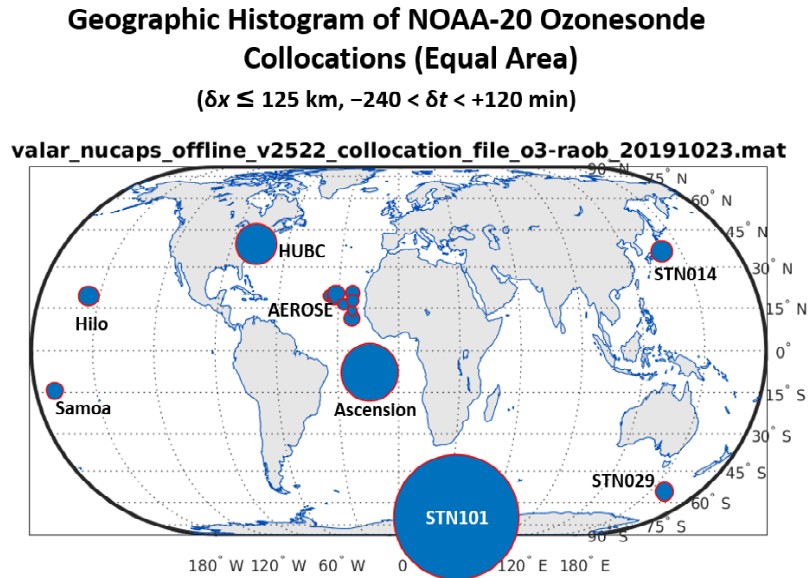


Figure 2.16: Geographic histograms of NOAA-20 ozonesonde collocations used for NOAA-20 NUCAPS IR ozone profile EDR validation, including SHADOZ, WOUDC sites, and NOAA-20 dedicated ozonesondes launched from ship-based intensive campaigns.

Global profile error statistics for NUCAPS NOAA-20 AVTP and AVMP versus dedicated RAOBs (Fig. 2.15) are given in Figures 2.17 and 2.18, respectively. The right plots show the bias statistics given by the coarse-layer means with $\pm 1\sigma$ variability about the mean given by the error bars. The JPSS Level 1 specification requirements are defined in terms of RMSE statistics shown with dashed lines in the left plots. The corresponding broad-layer results are shown with asterisks. Results of NOAA-20 NUCAPS IR ozone profile EDRs versus global ozonesondes (Fig. 2.16) are summarized in Fig. 2.19, which shows coarse- and broad-layer profile statistics. When one accounts for the uncertainties inherent in the radiosonde and ozonesonde data along with the mismatch errors, the NOAA-20 NUCAPS AVTP/AVMP/ O_3 retrievals, as summarized in these figures, are considered to have reached Validated Maturity.

NUCAPS is a NOAA/STAR “enterprise algorithm” that not only runs on SNPP and NOAA-20, but also the EUMETSAT Metop satellite series (Metop-A/B/C). Because these satellites are in a different orbit, we do not have dedicated sonde data for validation. However, we can use global numerical model comparisons (Hierarchical Method #1) as a transfer-standard to compare against similar global analyses for SNPP/NOAA-20. Global statistics for NUCAPS Metop-A/B/C versus collocated

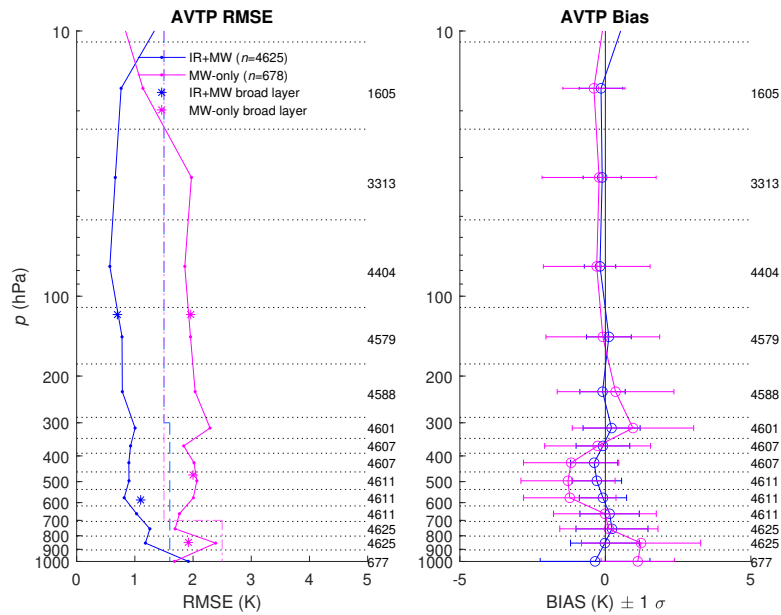


Figure 2.17: Coarse- and broad-layer statistical uncertainty assessment of the NOAA-20 NUCAPS AVTP EDR (offline v2.5.2.2 operational emulation) versus collocated dedicated/reference RAOBs (Figure 2.15) for retrievals accepted by the quality flag within space-time collocation criteria. The left and right plots show the RMSE and bias ($\pm 1\sigma$ variability) results, respectively. NUCAPS IR+MW (clear to partly cloudy) and MW-only (cloudy) performances are given in blue and magenta respectively, with collocation sample size for each coarse layer given in the right margins.

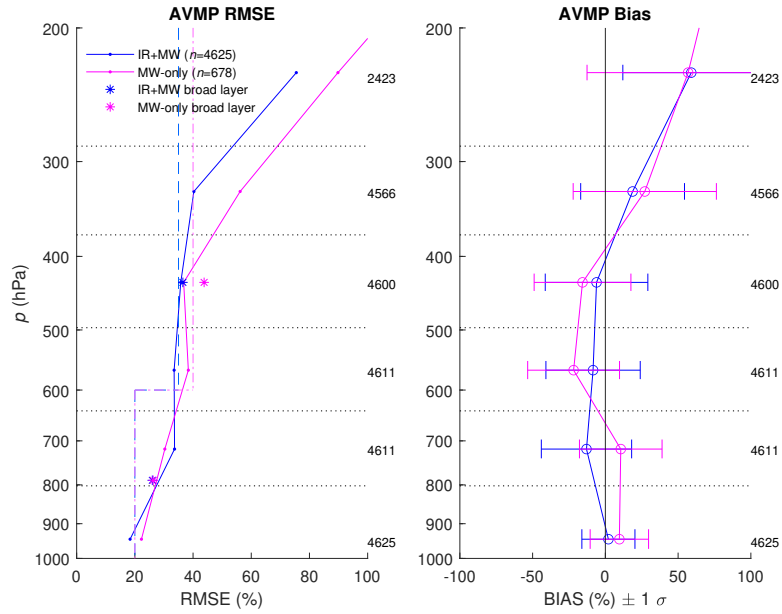


Figure 2.18: As Figure 2.17 except for AVMP.

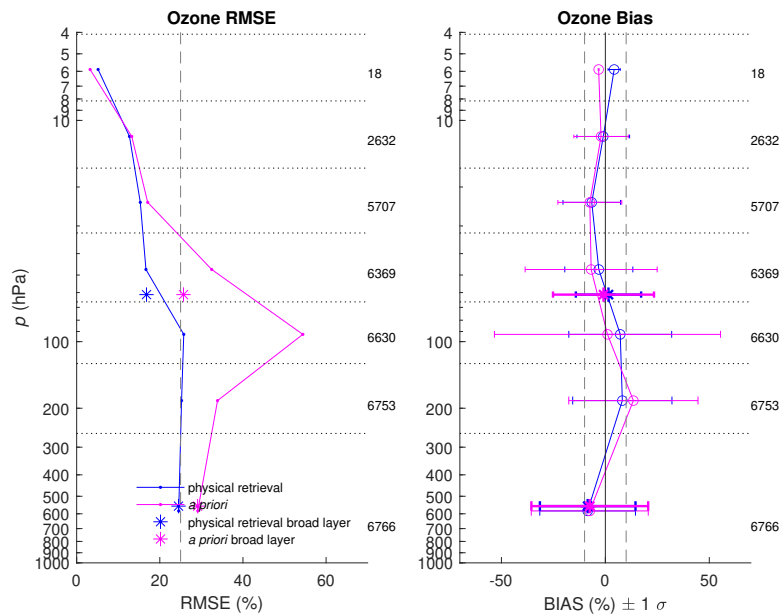


Figure 2.19: As Figure 2.17 except for IR ozone profile.

ECMWF are shown in Figures 2.20 and 2.21.

NUCAPS v3.0 Carbon Trace Gas Product Upgrades. The NOAA-20 NUCAPS carbon trace gas EDR data have been produced since 23 May 2018 with the NUCAPS Hyperspectral Enterprise Algorithm Package (HEAP 2.1) running in operations effective 16 June 2020. The primary change from HEAP 2.1 (CO₂ Beta maturity version based on the maturity review dated 24 October 2019) to the current version HEAP 2.3 (CO₂ Validated Maturity version based on the Maturity Review dated 17 December 2020) is the inclusion of updated CO₂ QC flags. The trace gas retrieval product QA/QC criteria are based on many acceptance checks associated with cloud-cleared radiances (CCRs). In addition, retrieval quality, chi-square (χ^2), and degrees-of-freedom for Signals (DOFs) associated with each trace gas (CO, CH₄, and CO₂) are applied in optimizing trace gas product quality.

This version also includes major improvements to the trace gas climatological *a priori* profiles (i.e., CO, CH₄, and CO₂). The *a priori* profiles for CO were derived from the NCAR MOZART-GEOSS model. Different climatological background *a priori* profiles are used for northern and southern hemispheres, and a smoothly varying *a priori* is used across the tropics from 15°S to 15°N. The CO₂ *a priori* profiles are interpolated from a 12-month compilation, but there is no interannual variability. Methane (CH₄) *a priori* profiles are based on *in situ* measurements from HIAPER Pole-to-Pole Observations (HIPPO) and Atmospheric Tomography Mission (ATom) field campaigns. Latitudinal variations are included in the methane *a priori*, but do not contain any seasonal or interannual variability. The CO₂ *a priori* is derived using the NOAA Global Monitoring Laboratory (GML) CarbonTracker model and includes both latitudinal and seasonal variabilities. The NOAA/GML surface measurement anomalies derived from observations from 2002 through 2020 are used to define the CO₂ linear trend.

NUCAPS v3.0 Carbon Trace Gas Validated Maturity. Validation of the NUCAPS trace gas products was carried out based on the following hierarchy of reference datasets (cf. Section 2.8.1): (1) global comparisons against the Copernicus Atmospheric Monitoring Service (CAMS) model, (2) intercomparisons against TROPOMI satellite products, (3) assessments versus surface-based network of measurements (TCCON and AirCore), and (4) *in situ* aircraft data from the Atmospheric Tomography Mission (ATom). Future validation work will leverage campaigns of opportunity such as Western Wildfire Experiment for Cloud Chemistry, Aerosol Absorption, and Nitrogen (WE-CAN), Fire Influence on Regional and Global Environments Experiment (FIREX).

Comparisons of the NUCAPS SNPP/NOAA-20 CO retrievals at 506 hPa with

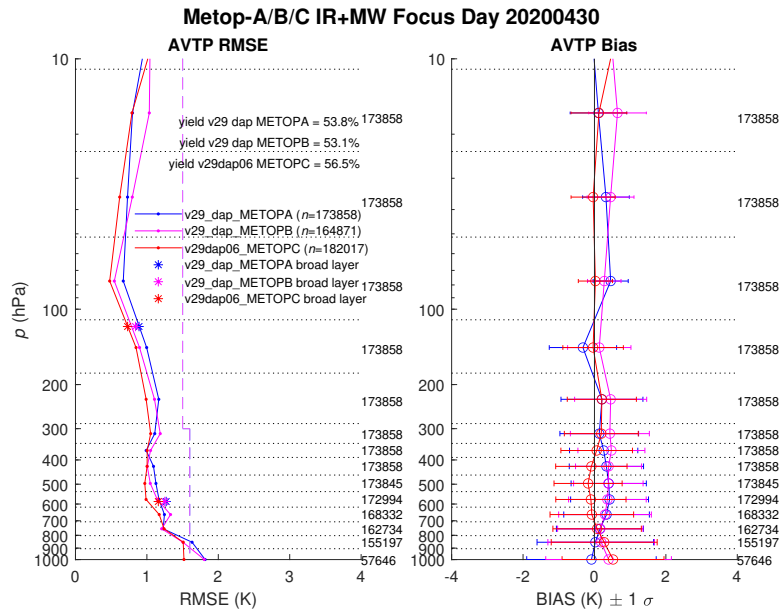


Figure 2.20: As Figure 2.17 except for Metop-A/B/C versus global ECMWF model collocations.

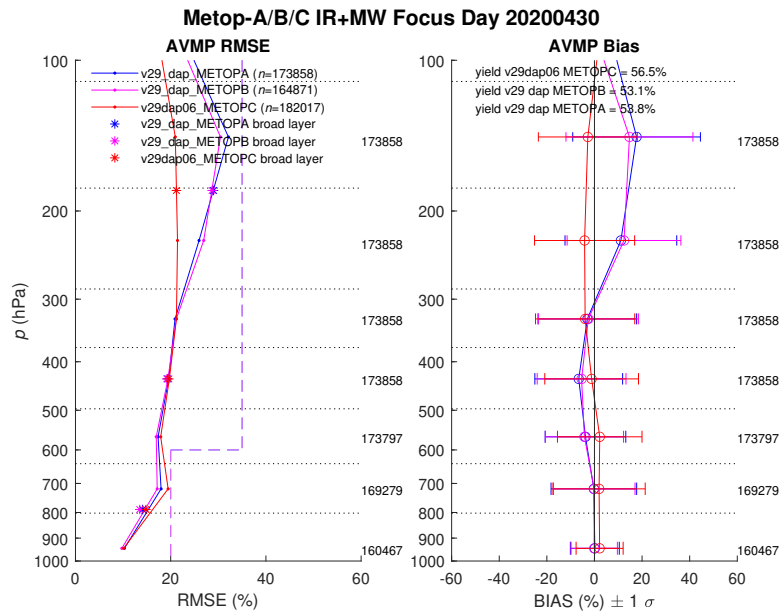


Figure 2.21: As Figure 2.18 except for Metop-A/B/C versus global ECMWF model collocations.

CAMS model analysis fields and Aqua-AIRS CO retrievals shows consistency between SNPP and NOAA-20, along with similar spatial patterns. Figure 2.22 shows a comparison of CO₂ between NUCAPS SNPP CrIS and NASA OCO-2 using 11 focus days spanning 1 year period. NUCAPS SNPP CrIS CO₂ agrees with OCO-2 v9 to within approximately 2.5 ppm or 0.5%. In comparison, however, the NUCAPS SNPP CrIS measurements provide twice daily nearly global coverage owing to its broad swaths and cloud-clearing algorithm.

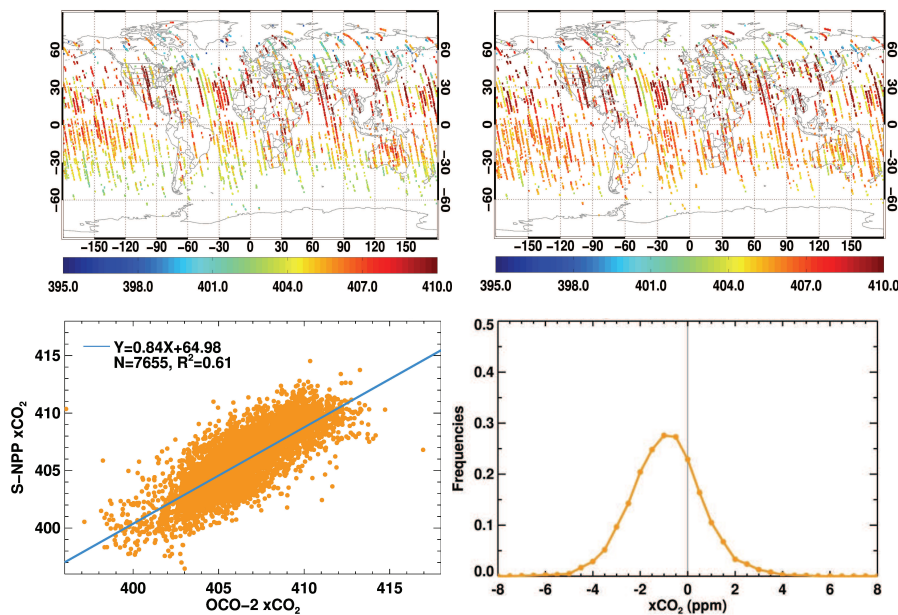


Figure 2.22: NUCAPS retrieved carbon dioxide EDR comparison with OCO-2: (top left) collocated SNPP NUCAPS CO₂ retrievals in averaged column (xCO₂ in ppm), (top right) collocated OCO-2 retrievals, (bottom left) correlations of CO₂ between SNPP NUCAPS and OCO-2, and (bottom right) histogram of the differences (NUCAPS minus OCO-2). Data used are 11 focus days spanning a 1 year period.

Finally, as mentioned above, the SNPP and NOAA-20 carbon trace gas retrievals (i.e., CO, CH₄, and CO₂) have been extensively validated versus *in situ* reference datasets, including TCCON, AirCore and ATom (Nalli et al., 2020). Figure 2.23 shows the collocation sample for the NOAA-20 NUCAPS with ATom-4 profile extractions used for the statistical assessment of the NOAA-20 NUCAPS v3.0 carbon trace gas products (CO, CH₄, and CO₂, QA-accepted cases) shown in Fig. 2.24. Aircraft *in situ* data used as the baseline in the assessment were obtained from NOAA/GML

Picarro measurements. The global measurement uncertainties (RMSE) for total integrated columns (under clear-to-partly cloudy conditions) are approximately 20%, 1.5% and 0.75%, respectively (Fig. 2.24, top); when NUCAPS AKs are applied (Fig. 2.24, bottom), these are reduced to approximately 9.2%, 1.5% and 0.3% (Nalli et al., 2020).

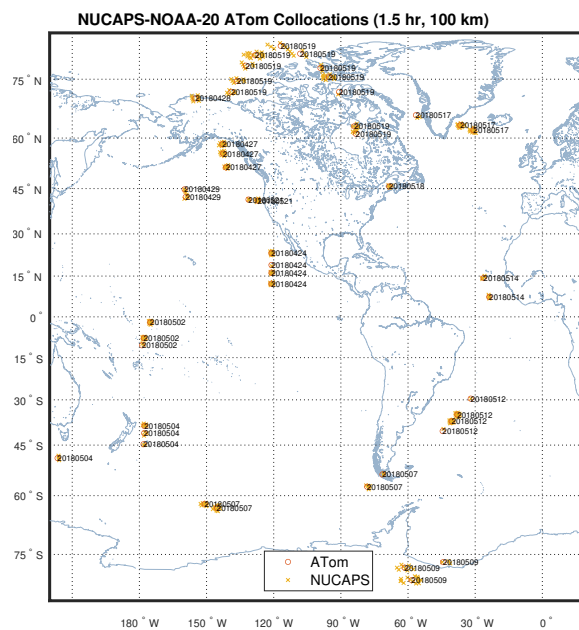


Figure 2.23: ATom collocation samples for NOAA-20 NUCAPS v3.0 carbon trace gas profile validation (Nalli et al., 2020). NUCAPS FOR (gold \times) are shown collocated with extracted ATom profiles (red circles) within space-time collocation windows of $\Delta r \leq 100$ km radius and Δt within ± 1.5 h for the ATom-4 campaign.

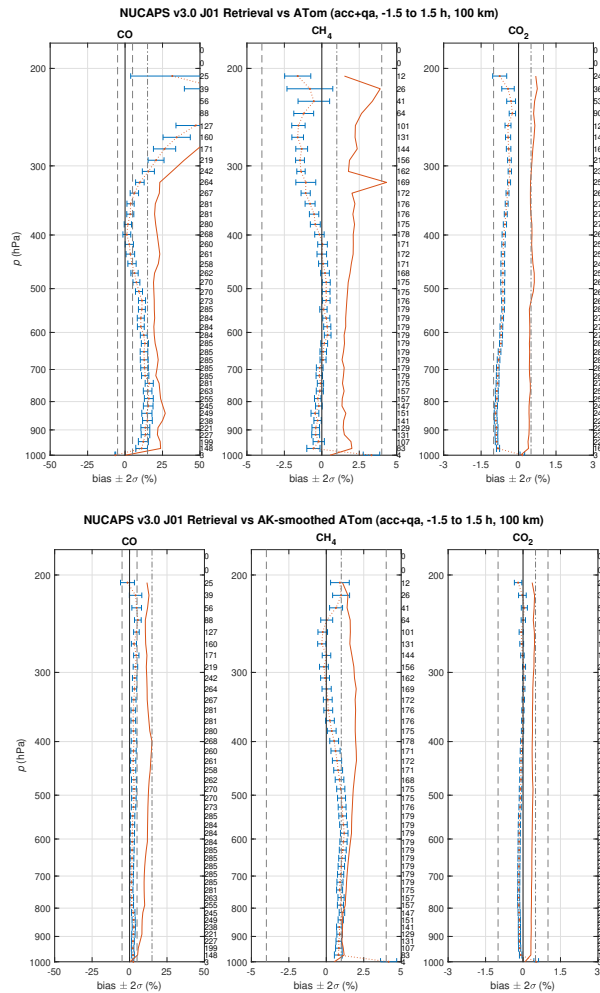


Figure 2.24: NOAA-20 NUCAPS carbon trace gas profile retrieval statistics (Nalli et al., 2020): (top) results without AKs, and (bottom) results with NUCAPS AKs applied. Shown are bias (dotted red line) and precision (1σ variability; solid red line) versus ATom-4 *in situ* aircraft data (NOAA/GML measurements): (left) carbon monoxide, (center) methane, and (right) carbon dioxide. Layer sample sizes are indicated on the right margins.

3. REFERENCES

- Aumann, H. H., et al., 2003: AIRS/AMSU/HSB on the Aqua Mission: Design, science objectives, data products, and processing systems. *IEEE Trans. Geosci. Remote Sensing*, **41** (2), 253–264.
- Barnet, C., 2009: NPOESS Community Collaborative Calibration/Validation Plan for the NPOESS Preparatory Project CrIS/ATMS EDRs. Tech. Rep. I30004, Ver. 1 Rev. B, Integrated Program Office (IPO), Silver Spring, Maryland.
- Barnet, C., J. Blaisdell, and J. Susskind, 2000: An analytical transformation for use in computation of interferometric spectra for remote sensing applications spectra. *IEEE Trans. Geosci. Remote Sens.*, **38**, 169–183.
- Bodeker, G. E., et al., 2016: Reference upper-air observations for climate: From concept to reality. *Bull. Am. Meteorol. Soc.*, **97** (1), 123–125.
- Chahine, M. T., 1974: Remote sounding of cloudy atmospheres. I. The single cloud layer. *J. Atmos. Sci.*, **31**, 233–243.
- Chahine, M. T., 1977: Remote sounding of cloudy atmospheres. II. Multiple cloud formations. *J. Atmos. Sci.*, **34**, 744–757.
- Chandrasekhar, S., 1950: *Radiative Transfer*. Dover, New York, 393 pp. pp.
- Divakarla, M., et al., 2008: Evaluation of Atmospheric Infrared Sounder ozone profiles and total ozone retrievals with matched ozonesonde measurements, ECMWF ozone data, and Ozone Monitoring Instrument retrievals. *J. Geophys. Res.*, **113**, D15308, doi:10.1029/2007JD009317.
- Divakarla, M., et al., 2014: The CrIMSS EDR Algorithm: Characterization, optimization and validation. *J. Geophys. Res. Atmos.*, doi:10.1002/2013JD020438.
- Divakarla, M. G., C. D. Barnet, M. D. Goldberg, L. M. McMillin, E. Maddy, W. Wolf, L. Zhou, and X. Liu, 2006: Validation of Atmospheric Infrared Sounder temperature and water vapor retrievals with matched radiosonde measurements and forecasts. *J. Geophys. Res.*, **111**, D09S15, doi:10.1029/2005JD006116.
- Gambacorta, A., et al., 2014: An experiment using high spectral resolution CrIS measurements for atmospheric trace gases: Carbon monoxide retrieval

- impact study. *IEEE Geosci. Remote Sensing Lett.*, **11 (9)**, 1639–1643, doi: 10.1109/LGRS.2014.2303641.
- Goldberg, M. D., H. Kilcoyne, H. Cikanek, and A. Mehta, 2013: Joint Polar Satellite System: The United States next generation civilian polar-orbiting environmental satellite system. *J. Geophys. Res. Atmos.*, **118**, 13,463–13,475, doi: 10.1002/2013JD020389.
- Goldberg, M. D., Y. Qu, L. M. McMillin, W. Wolf, L. Zhou, and M. Divakarla, 2003: AIRS near-real-time products and algorithms in support of operational numerical weather prediction. *IEEE Trans. Geosci. Remote Sensing*, **41**, 379–389.
- Han, Y., Y. Chen, X. Xiong, and X. Jin, 2015: S-NPP CrIS full spectral resolution SDR processing and data quality assessment. American Meteorological Society, Phoenix, AZ, Annual Meeting, <https://ams.confex.com/ams/95Annual/webprogram/Paper261524.html>.
- Han, Y., et al., 2013: Suomi NPP CrIS measurements, sensor data record algorithm, calibration and validation activities, and record data quality. *J. Geophys. Res. Atmos.*, **118**, 12,734–12,748, doi:10.1002/2013JD020344.
- Hannon, S. E., L. L. Strow, and W. W. McMillan, 1996: Atmospheric infrared fast transmittance models: a comparison of two approaches. *Optical Spectroscopic Techniques and Instrumentation for Atmospheric and Space Research II*, P. B. Hays and J. Wang, Eds., SPIE, International Society for Optics and Photonics, Vol. 2830, 94–105, doi:10.1117/12.256106.
- Hyland, R. W. and A. Wexler, 1983: Formulations for the thermodynamic properties of the saturated phases of H₂O from 173.15 K to 473.15 K. *ASHRAE Trans.*, **2A**, 500–519.
- Inness, A., et al., 2019: The CAMS reanalysis of atmospheric composition. *Atmos. Chem. Phys.*, **19**, 3515–3556, doi:10.5194/acp-19-3515-2019.
- Jacobson, A. R., et al., 2020: CarbonTracker CT2019. NOAA Earth System Research Laboratory, Global Monitoring Division, doi:10.25925/39M3-6069.
- Karion, A., C. Sweeney, P. Tans, and T. Newberger, 2010: AirCore: An Innovative Atmospheric Sampling System. *J. Atmos. Oceanic Technol.*, **27 (11)**, 1839–1853, doi:10.1175/2010JTECHA1448.1.

- Kornfield, J. and J. Susskind, 1977: On the effect of surface emissivity on temperature retrievals. *Mon. Weather Rev.*, **105**, 1605–1608.
- Masuda, K., 2006: Infrared sea surface emissivity including multiple reflection effect for isotropic gaussian slope distribution model. *Remote Sens. Environ.*, **103**, 488–496.
- Masuda, K., T. Takashima, and Y. Takayama, 1988: Emissivity of pure and sea waters for the model sea surface in the infrared window regions. *Remote Sens. Environ.*, **24**, 313–329.
- Mather, J. H. and J. W. Voyles, 2013: The ARM climate research facility: A review of structure and capabilities. *Bull. Amer. Meteorol. Soc.*, **94** (3), 377–392, doi:10.1175/BAMS-D-11-00218.1.
- McMillin, L. M. and H. E. Fleming, 1976: Atmospheric transmittance of an absorbing gas: A computationally fast and accurate transmittance model for absorbing gases with constant mixing ratios in inhomogeneous atmospheres. *Appl. Optics*, **15**, 358.
- Membrive, O., C. Crevoisier, C. Sweeney, F. Danis, A. Hertzog, A. Engel, H. Bönisch, and L. Picon, 2017: AirCore-HR: a high-resolution column sampling to enhance the vertical description of CH₄ and CO₂. *Atmos. Meas. Tech.*, **10**, 2163–2181.
- Miloshevich, L. M., H. Vömel, D. N. Whiteman, B. M. Lesht, F. J. Schmidlin, and F. Russo, 2006: Absolute accuracy of water vapor measurements from six operational radiosonde types launched during AWEX-G and implications for AIRS validation. *J. Geophys. Res.*, **111**, D09S10, doi:10.1029/2005JD006083.
- Morris, V., et al., 2006: Measuring trans-Atlantic aerosol transport from Africa. *Eos Trans. AGU*, **87** (50), 565–571.
- Nalli, N. R., P. J. Minnett, E. Maddy, W. W. McMillan, and M. D. Goldberg, 2008a: Emissivity and reflection model for calculating unpolarized isotropic water surface leaving radiance in the infrared. 2: Validation using Fourier transform spectrometers. *Appl. Optics*, **47** (25), 4649–4671.
- Nalli, N. R., P. J. Minnett, and P. van Delst, 2008b: Emissivity and reflection model for calculating unpolarized isotropic water surface leaving radiance in the infrared. 1: Theoretical development and calculations. *Appl. Optics*, **47** (21), 3701–3721.
- Nalli, N. R., et al., 2006: Ship-based measurements for infrared sensor validation during Aerosol and Ocean Science Expedition 2004. *J. Geophys. Res.*, **111**, D09S04, doi:10.1029/2005JD006385.

- Nalli, N. R., et al., 2011: Multi-year observations of the tropical Atlantic atmosphere: Multidisciplinary applications of the NOAA Aerosols and Ocean Science Expeditions (AEROSE). *Bull. Am. Meteorol. Soc.*, **92**, 765–789, doi:10.1175/2011BAMS2997.1.
- Nalli, N. R., et al., 2013: Validation of satellite sounder environmental data records: Application to the Cross-track Infrared Microwave Sounder Suite. *J. Geophys. Res. Atmos.*, **118**, 13,628–13,643, doi:10.1002/2013JD020436.
- Nalli, N. R., et al., 2018a: Validation of atmospheric profile retrievals from the SNPP NOAA-Unique Combined Atmospheric Processing System. Part 1: Temperature and moisture. *IEEE Trans. Geosci. Remote Sensing*, **56 (1)**, 180–190, doi:10.1109/TGRS.2017.2744558.
- Nalli, N. R., et al., 2018b: Validation of atmospheric profile retrievals from the SNPP NOAA-Unique Combined Atmospheric Processing System. Part 2: Ozone. *IEEE Trans. Geosci. Remote Sensing*, **56 (1)**, 598–607, doi:10.1109/TGRS.2017.2762600.
- Nalli, N. R., et al., 2020: Validation of carbon trace gas profile retrievals from the NOAA-Unique Combined Atmospheric Processing System for the Cross-Track Infrared Sounder. *Remote Sens.*, **12 (19)**, 3245, doi:10.3390/rs12193245.
- Newman, S. M., et al., 2012: The Joint Airborne IASI Validation Experiment: An evaluation of instrument and algorithms. *J. Quant. Spectrosc. Radiat. Transfer*, **113**, 1372–1390.
- Reale, T., B. Sun, F. H. Tilley, and M. Pettey, 2012: The NOAA Products Validation System. *J. Atmos. Ocean. Tech.*, **29**, 629–645, doi:10.1175/JTECH-D-11-00072.1.
- Rodgers, C. D. and B. J. Connor, 2003: Intercomparison of remote sounding instruments. *J. Geophys. Res.*, **108 (D3)**, 4116, doi:10.1029/2002JD002299.
- Rosenkranz, P. W., 1995: A rapid atmospheric transmittance algorithm for microwave sounding channels. *IEEE Transactions on Geoscience and Remote Sensing*, **33 (5)**, 1135–1140, doi:10.1109/36.469477.
- Rosenkranz, P. W., 2001: Retrieval of temperature and moisture profiles from amsu-a and amsu-b measurements. *IEEE Transactions on Geoscience and Remote Sensing*, **39 (11)**, 2429–2435, doi:10.1109/36.964979.

- Rosenkranz, P. W., 2003: Rapid radiative transfer model for AMSU/HSB channels. *IEEE Transactions on Geoscience and Remote Sensing*, **41** (2), 362–368, doi:10.1109/TGRS.2002.808323.
- Rosenkranz, P. W., 2006: Cloud liquid-water profile retrieval algorithm and validation. *J. Geophys. Res.*, **111**, D09S08, doi:10.1029/2005JD005832.
- Seemann, S. W., E. E. Borbas, R. O. Knuteson, G. R. Stephenson, and H.-L. Huang, 2008: Development of a Global Infrared Land Surface Emissivity Database for Application to Clear Sky Sounding Retrievals from Multispectral Satellite Radiance Measurements. *J. Appl. Meteorol. Climatol.*, **47** (1), 108–123, doi:10.1175/2007JAMC1590.1.
- Smith, W. L. and H. M. Woolf, 1976: The use of eigenvectors of statistical covariance matrices for interpreting satellite sounding radiometer observations. *J. Atmos. Sci.*, **33**, 1127–1140.
- Strow, L., H. Motteler, R. Benson, S. Hannon, and S. D. Souza-Machado, 1998: Fast-computation of monochromatic infrared atmospheric transmittances using compressed look-up tables. *J. Quant. Spectrosc. Radiat. Transfer*, **59**, 303–317.
- Strow, L. L., S. E. Hannon, S. D. Souza-Machado, H. E. Motteler, and D. Tobin, 2003: An overview of the AIRS radiative transfer model. *IEEE Trans. Geosci. Remote Sensing*, **41** (2), 303–313.
- Stull, R. B., 2000: *Meteorology for Scientists and Engineers*. 2d ed., Brooks/Cole, Cengage Learning, Belmont, California.
- Sun, B., A. Reale, D. J. Seidel, and D. C. Hunt, 2010: Comparing radiosonde and cosmic atmospheric profile data to quantify differences among radiosonde types and the effects of imperfect collocation on comparison statistics. *J. Geophys. Res.*, **115**, D23 104, doi:10.1029/2010JD014457.
- Sun, B., A. Reale, F. Tilley, M. Petty, N. R. Nalli, and C. D. Barnet, 2017: Assessment of NUCAPS S-NPP CrIS/ATMS sounding products using reference and conventional radiosonde observations. *IEEE J. Sel. Topics Appl. Earth Observ.*, **10** (6), 2499–2509, doi:10.1109/JSTARS.2017.2670504.
- Susskind, J., C. D. Barnet, and J. Blaisdell, 1998: Determination of atmospheric and surface parameters from simulated AIRS/AMSU sounding data: Retrieval methodology and cloud clearing methodology. *Adv. Space Res.*, **21**, 369–384.

- Susskind, J., C. D. Barnet, and J. M. Blaisdell, 2003: Retrieval of atmospheric and surface parameters from AIRS/AMSU/HSB data in the presence of clouds. *IEEE Trans. Geosci. Remote Sensing*, **41** (2), 390–409.
- Taylor, J. P., et al., 2008: EAQUATE: An international experiment for hyperspectral atmospheric sounding validation. *Bull. Amer. Meteorol. Soc.*, **89** (2), 203–218, doi:10.1175/BAMS-89-2-203.
- Thompson, A. M., J. C. Witte, S. J. Oltmans, and F. J. Schmidlin, 2004: SHADOZ — A tropical ozonesonde-radiosonde network for the atmospheric community. *Bull. Amer. Meteorol. Soc.*, **85** (10), 1549–1564, doi:10.1175/BAMS-85-10-1549.
- Tobin, D. C., et al., 2006: Atmospheric Radiation Measurement site atmospheric state best estimates for Atmospheric Infrared Sounder temperature and water vapor retrieval validation. *J. Geophys. Res.*, **111**, D09S14, doi:10.1029/2005JD006103.
- Wallace, J. M. and P. V. Hobbs, 1977: *Atmospheric Science: An Introductory Survey*. Academic Press, San Diego, California.
- Weng, F., X. Zou, X. Wang, S. Yang, and M. D. Goldberg, 2012: Introduction to Suomi national polar-orbiting partnership advanced technology microwave sounder for numerical weather prediction and tropical cyclone applications. *J. Geophys. Res.*, **117**, D19112, doi:10.1029/2012JD018144.
- Wexler, A., 1976: Vapor pressure formulation for water in range 0 to 100°C: A revision. *Res. Natl. Bur. Stand. U.S., Sect. A*, **80**, 775–785.
- Wofsy, S., et al., 2018: Atom: Merged atmospheric chemistry, trace gases, and aerosols. ORNL Distributed Active Archive Center, URL https://daac.ornl.gov/cgi-bin/dsviewer.pl?ds_id=1581, doi:10.3334/ornl daac/1581, URL https://daac.ornl.gov/cgi-bin/dsviewer.pl?ds_id=1581.
- Wofsy, S. C., the HIPPO Science Team, Cooperating Modellers, and Satellite Teams, 2011: HIAPER Pole-to-Pole Observations (HIPPO): fine-grained, global-scale measurements of climatically important atmospheric gases and aerosols. *Phil. Trans. R. Soc. A*, **369**, 2073–2086, doi:10.1098/rsta.2010.0313.
- Wunch, D., et al., 2011: The Total Carbon Column Observing Network. *Phil. Trans. R. Soc. A*, **369**, 2087–2112, doi:10.1098/rsta.2010.0240.
- Zhou, L., M. Divakarla, and X. Liu, 2016: An overview of the Joint Polar Satellite System (JPSS) science data product calibration and validation. *Remote Sens.*, **8** (139), doi:10.3390/rs8020139.

Zhou, L., et al., 2008: Regression of surface spectral emissivity from hyperspectral instruments. *IEEE Trans. Geosci. Remote Sensing*, **46 (2)**, 328–333.